Stony Brook University

Probing Flow-Induced Crystallization Precursor Structure in Polyolefin Melts by Means of Synchrotron X-Rays

A Dissertation Presented

by

Jong Kahk Keum

to

The Graduate School

In Partial fulfillment of the

Requirements

for the Degree of

Doctor of Philosophy

in

Chemistry

Stony Brook University

December 2007

Stony Brook University

The Graduate School

Jong Kahk Keum

We, the dissertation committee for the above candidate
for the Doctor of Philosophy degree, hereby recommend
acceptance of this dissertation.

Dr. Benjamin S. Hsiao, Advisor
Department of Chemistry

Dr. Benjamin Chu, Chairperson
Department of Chemistry

Dr. Roy Lacey, Third member
Department of Chemistry

Dr. Dennis G. Peiffer, Outside member
ExxonMobile Research and Engineering company

This dissertation is accepted by the Graduate School

Lawrence Martin
Dean of the Graduate School

Abstract of the Dissertation

Probing Flow-Induced Crystallization Precursor Structure in Polyolefin Melts by Means of Synchrotron X-Rays

by

Jong Kahk Keum

Doctor of Philosophy

In Chemistry

Stony Brook University

2007

The formation of flow-induced crystallization precursor structure, i.e. shish-kebab entities, in deformed polyolefin melts was studied by means of synchrotron small-angle X-ray scattering (SAXS) and wide-angle X-ray diffraction (WAXD). The study was performed under two different conditions to elucidate the role of high molecular weight chain as well as the effects of strain rate and strain in the formation of flow-induced crystallization precursor structure. First, to clarify the role of high molecular weight chains, binary polyolefin blends containing high and low molecular weight chains with varying composition were prepared by solution and melt mixing. The results showed that the formation and the stability of flow-induced crystallization precursor structure are greatly enhanced by a small amount of high molecular weight chains above the overlap concentration, implying that high molecular weight chains play an essential role in

forming flow-induced crystallization precursor structure. Second, to elucidate the strain and strain rate effects, a unique cross-slot flow cell which can apply consistent extensional flow was designed and constructed. The results demonstrated that the flow-induced crystallization precursor structure formation is strongly governed by the applied strain as well as the strain rate. As strain and rate are increased, the formation of flow-induced crystallization precursor structure is significantly facilitated. A critical strain, ε_c exists in the formation of flow-induced crystallization precursor structure, even when the applied strain rate, $\dot{\varepsilon}$ is higher than the critical strain rate, $\dot{\varepsilon}_c$. Around ε_c, a sharp transition from amorphous to crystalline state was observed, verifying that the crystalline shish precursor structure is formed first and it induces the growth of folded-chain lamellae, i.e. kebabs.

Table of Contents

List of Figures

List of Tables

Preface

In my thesis, I am mainly interested in understanding the nature of the earliest events of polymer crystallization in flow, where the deformation of high molecular weight chains would produce a stable oriented network, consisting of stretched segments and coiled segments between entanglement points as in typical network materials containing (physical or chemical) crosslinking points. The process may not need to undergo the whole range of stretch-coil transition. The stretched segments can undergo extended-chain crystallization and form shish, where the coiled segment can subsequently undergo folded-chain crystallization and form kebabs. The interplay between the flow field and the chain dynamics of the high molecular weight species thus shall dictate the topology of the flow-induced shish-kebab scaffold.

In order to elaborate this view in greater detail, in chapter 1, my main objective is thus to elucidate the molecular nature of flow-induced crystallization precursor structures in highly entangled polymer melts. To carry out the study properly, the choice of suitable samples and the design of appropriate experimental conditions were carefully made. For sample selection, two linear polyethylene (PE) samples with very different average molecular weights: high density polyethylene, HDPE and ultra high molecular weight polyethylene, UHMWPE were chosen. The former was used as a matrix and the latter (in small fractions) was used as precursor forming species.

In chapter 2, I introduce a unique cross-slot flow device which was recently designed and proven to apply highly consistent extensional flow to polymer melt at the stagnation point. The strain and strain rate effects on the formation of flow-induced precursor structure were investigated by means of synchrotron X-rays. Specifically, the

existence of critical strain on the formation of flow-induced precursor is discussed and suggested.

In chapter 3, I have chosen two PE blown films, processed at the same conditions, for *in-situ* small-angle X-ray scattering and wide-angle X-ray diffraction studies. The PE films were restrained during melting in order to preserve the initial precursor structures formed at high temperatures. The chosen blown films included linear low density polyethylene (LLDPE) and a blend of high density polyethylene (HDPE) with LLDPE. The HDPE sample contained a bimodal distribution of molecular weights: high molecular weight (HMW) and low molecular weight (LMW) components. The HDPE/LLDPE blend composition was selected in such a way that the concentration of the HMW-HDPE species was just above its overlap concentration. Results between LLDPE and HDPE/LLDPE blends were compared to elucidate the role of HMW species on the formation the crystallization precursor structures during the blowing process.

In chapter 4, I aimed to obtain some new insights into the nucleation (secondary nucleation) and growth behavior of twisted kebabs in sheared HDPE melts. Specifically, I have carried out 2D rheo-WAXD and rheo-SAXS measurements after cessation of a step shear. The results is analyzed by a simple shish-kebab model, consisting of central shish and sectorial twisted kebabs, in which each kebab forms sector-like folded surface as it grows outwards and gradually twists. In this simple model, when the degree of lamellar twisting is very small, the changes of (110) and (200) reflection patterns are significantly affected by the outer parts of each twisting kebab. This is because the volume of individual kebab would increase as it grow outwards, where the diffraction intensity (I) is proportional to the total crystal volume (V), $I \propto V$.[19,20] In addition, a simplified Avrami

equation was applied to examine the nucleation and growth mechanism of the twisted kebabs from the shish scaffold.

In chapter 5, a unique polymer blend system containing higher molecular weight isotactic polypropylene (HMW-iPP) and lower molecular weight linear low-density polyethylene (LMW-LLDPE) was prepared. Two experimental temperatures (130 ^{o}C and 140 ^{o}C) above cloud points (in quiescent state) were chosen by assuming UCST behavior; the temperatures were sufficiently low to enable the crystallization of iPP (can be viewed as the solute) in flow but high enough to prevent the crystallization of LLDPE (can be viewed as the solvent). The flow-induced crystallization behavior of HMW-iPP in this blend system was investigated by synchrotron *rheo*-WAXD (wide-angle X-ray diffraction) and *rheo*-SAXS (small-angle X-ray scattering) techniques. Specifically, by varying the composition of the blends, the effect of concentration (directly related to the density of chain entanglement) in the early stages of flow-induced crystallization is explored.

Acknowledgements

Foremost, I would like to express my deep gratitude to my thesis advisor Benjamin S. Hsiao for his valuable guidance and constant academic and financial support during my work on this Ph. D. thesis. I have learned a tremendous amount while under his supervision. His assiduity and strictness in scientific research make him a good example for me to follow in my future career.

I would like to specifically thank my committee members, professor Chu, professor Lacey and Dr. Dennis G. Peiffer, for their in-depth and invaluable suggestions and comments to my thesis. Many thanks are also due to my labmates Feng Zuo, Yimin Mao, Hongwen Zhou, Pranav Nawani and Kyunghwan Yoon and Drs. Hongyu Chen, Rainer Kolb, Ching-Tai Lue, Arnold Lustiger, Thomas Sun, Igors Sics, Rixia Rong, Jie Zhou, Rajesh Somani and Christian Burger. In addition, this research would have not been possible without the financial support of National Science Foundation.

I thank my wife, So Young and my parents for their unending support during the past years. Their continuous encouragement is the source of energy and powerful backing inspiring me to pursue further achievement in m future career. My gratitude is also due to my son, Dongho.

Chapter 1. Dynamic Formation of Flow-Induced Shish-Kebab Structure in Highly Entangled Melts of UHMWPE/HDPE Blends

1.1 Introduction

Flow-induced crystallization of semi-crystalline polymers is an important subject with many practical implications from process design to property control. In particular, the molecular mechanism responsible for the initial formation of the "precursor structure" under flow prior to full scale crystallization in highly entangled polymer melts is of great interests to both academic and industrial communities.[1-14] The current thinking considers that deformation of highly entangled species in the melt directly results in extended-chain crystallization forming shish and subsequent folded-chain crystallization forming kebabs, and thus indirectly influences the final morphology of polymer products.[12] However, the experimental results revealing the kinetics and thermal stability of flow-induced shish-kebab structure are rare, which is the purpose of this study.

Recently, in-situ rheo-X-ray studies confirmed that the high molecular weight species play an essential role in forming the initial crystallization precursor structure (shish-kebabs) in the entangled melt under a given flow condition.[10-17] The molecular basis of flow-induced shish-kebab formation in entangled polymer melt has been related to the concept of coil-stretch transition for polymer chains, which was first proposed by de Gennes a decades ago based on the chain dynamics in dilute solutions.[18] Later, Chu *et al*. experimentally verified that the coil-stretch transition of a single DNA chain in dilute solution is indeed the first-order transition, where the conformation change occurs abruptly above a critical strain rate, $\dot{\varepsilon}_c$.[19] For flow-induced crystallization in entangled

polymer melts, Keller also adopted the concept of coil-stretch transition. He proposed the existence of a critical orientation molecular weight, M^*, for linear polymer chains, which can be scaled with critical strain $\dot{\varepsilon}_c \sim (M^*)^{-\beta}$.[20] Thus, only the polymer chains with molecular weights higher than M^* can remain stretched after a given flow, while shorter chains relax back to the coiled state. However, the coil-stretch transition at the whole chain level in entangled melt is still a controversial viewpoint. This is because it is very unlikely that long entangled chain can disentangle itself and undergo the stretch-coil transition under typical experimental conditions, as in our recent rheo-X-ray studies.[12]

Different from the concept of Keller et al.[20], we hypothesize that deformation of highly entangled chains in a supercooled state would produce a stable oriented network, consisting of stretched segments and coiled segments between entanglement points as in typical network materials containing (physical or chemical) crosslinking points. The process may not need to undergo the stretch-coil transition. The stretched segments can undergo extended-chain crystallization and form shish, where the coiled segment can subsequently undergo folded-chain crystallization and form kebabs.[12] The interplay between the flow field and the chain dynamics of the high molecular weight species in particular, thus shall dictate the topology of the flow-induced shish-kebab scaffold. The concept of *M** for entangled melt is still valid and useful, but the clear definition of *M** and the appropriate methodology to determine its value still requires further investigation.

In our previous studies[21], a bimodal blend, containing a small fraction of crystallizing high molecular species and the matrix of non-crystallizing lower molecular weight species, was used as the model system to explore the formation of precursor structure (shish-kebabs) induced by flow before full scale crystallization. It has been well

demonstrated that phase separation in bimodal polymer blends containing identical chemical composition (i.e., the interaction parameter χ is near zero) but different chain length or chain branching (i.e., different relaxation time spectrum and viscosities) can be induced by flow.[22,23] In fact, the miscibility between the two species depends on the strength of the flow field. Under strong flow (e.g. fiber spinning and injection molding), large phase separated domains (in microns), such as microfibrillar superstructure or even larger skin-core morphology, can be produced. Under weak flow (as in this study), nanoscopic phase separated domains (in tens of nanometers) can be obtained. The former may be dominated by the behavior of large scale liquid-liquid phase separation (LLPS)[24], while the latter may be dominated by the process of crystallization from oriented chains. Recently, Olmsted *et al*. have rationalized the occurrence of nanoscopic liquid-liquid phase separation in polymer melt prior to crystallization through the pathway of spinodal decomposition, even in the absence of flow.[24] However, we do not feel that the step of spinodal decomposition is necessary to induce the shish-kebab structure by flow.

A great deal of efforts has been made to understand the nucleation and growth behavior of polymers under flow in the last several decades. The general behavior of flow-induced crystallization can be understood by conventional theories[20] and the kinetics process can only be approximately described by phenomenological expressions[25], however, the exact molecular mechanism responsible for the nucleation and growth processes at the very initial stage under flow is still unclear. Thus, in this study, our main objective is to elucidate the molecular nature of flow-induced crystallization precursor structures in entangled polymer melts. In order to carry out the study properly, the choice of suitable samples and the design of appropriate experimental conditions were carefully made. For sample selection, two linear polyethylene (PE) samples with very different

average molecular weights: high density polyethylene, HDPE, ($\overline{M}_w$ = 112,000 g/mol) and ultra high molecular weight polyethylene, UHMWPE ($\overline{M}_w$ = 5~6,000,000 g/mol) were chosen. The former was used as a matrix and the latter (in small fractions) was used as precursor forming species (a similar study using a lower molecular weight PE (Mw = 50,000 g/mol, polydispersity = 2.1) as the matrix has been carried out by us previously[21]). The experimental temperature was selected to be above the melting point of HDPE, where only the crystallization behavior of UHMWPE could be observed. Furthermore, the experimental temperature was first set sufficiently high only to allow the real-time investigation of shish formation, but not kebab formation, using in-situ small-angle X-ray scattering (SAXS) and wide-angle X-ray diffraction (WAXD) techniques with synchrotron radiation.

1.2 Experimental

1.2.1 Materials and sample preparation

The HDPE sample ($\overline{M}_w$ = 112,000 g/mol, polydispersity ~ 9.1) was provided by the Dow Chemical Company; the UHMWPE sample ($\overline{M}_w$ = 5 - 6,000,000 g/mol, polydispersity ~ 9.0) was provided by Basell USA. Both samples were polymerized by Ziegler-Natta catalysts and had broad polydispersity. The chosen concentrations of UHMWPE in the two blends were 2 and 5 wt%, respectively, which were significantly

higher than the estimated overlap concentration of UHMWPE (c^* ~ 0.2 wt%). The overlap concentration was estimated based on the equation, $c^* = 3\overline{M}_w \Big/ 4\pi\left[\left\langle R_g^2\right\rangle^{1/2}\right]^3 N_a$ with $\left\langle R_g^2\right\rangle^{1/2}$ being the root-mean-square radius of gyration and N_a being the Avogadro's number.[21,26,27] The characteristic ratio of $\left\langle R_g^2\right\rangle^{1/2} / \overline{M}_w{}^{1/2}$ for PE was 0.46 based on SANS measurements.[28]

The polymer blends were prepared by a solution blending procedure to ensure that the two species were intimately mixed at the molecular level. In order to prevent the sample degradation during mixing, 3 wt% of antioxidants (Irgonox 1076) was added. The detailed mixing procedure has been described elsewhere.[21] A control sample of neat HDPE without the addition of UHMWPE was also prepared using the same procedure. Polymer films with about 0.5 mm thickness were prepared by compression molding at 172 ^oC for 5 min. Samples in the form of a ring (inner diameter = 10 mm, outer diameter = 20 mm) were cut from the melt pressed films for rheo-X-ray measurements.

1.2.2 Instrumentation

A Linkam CSS-450 optical shear stage, modified for in-situ rheo-X-ray experiments was used to apply controlled step shear to the blend samples. The details of this modified shear apparatus have been described elsewhere.[14] In short, the sample was placed in the gap between two X-ray windows (i.e., a Kapton window and a diamond window) and was completely enclosed in the measuring cell. The chosen step shear

conditions were: shear rate $\dot{\gamma} = 100\, s^{-1}$ and duration time $t_s = 5\, s$, where a constant strain (ε) of 500 shear unit was applied to the samples.

In-situ rheo-SAXS (small-angle X-ray scattering) and rheo-WAXD (wide-angle X-ray diffraction) measurements were carried out at the X27C beamline in the National Synchrotron Light Source (NSLS), Brookhaven National Laboratory (BNL). The X-ray wavelength was 1.371 Å. Two dimensional (2D) SAXS and WAXD patterns were collected by using a MAR CCD X-ray detector (MAR-USA), which had a resolution of 1024×1024 pixels (pixel size = 158.44 μm). For SAXS measurements, the sample-to-detector distance was 1832 mm and the scattering angle was calibrated by silver behenate (AgBe). For WAXD measurements, the sample-to-detector distance was 112.4 mm and the diffraction angle was calibrated by aluminum oxide (Al_2O_3). All X-ray images (SAXS and WAXD) were corrected for background scattering, air scattering, sample absorption and synchrotron X-ray beam fluctuations.

1.2.3 Experimental procedures

In order to ensure that the melts were free of any memory effects associated with prior thermal and mechanical histories, all samples were first heated to 172 ^{o}C, which was substantially higher than the equilibrium melting temperature for PE ($T_m^o \approx 145.5\ ^{o}$C), for 5 min. The melts were then rapidly cooled to the chosen crystallization temperature (i.e., 142 ^{o}C) at a -30 ^{o}C/min rate for in-situ SAXS and WAXD measurements. The data acquisition time was 15 s and the data storage time was 5 s for each SAXS and WAXD image collection. After 45 min of isothermal measurement, the once-sheared melt was

subsequently cooled to 134 ^{o}C and held there for 30 min to study further crystallization. The resulting once-sheared and crystallized sample was then gradually heated from 134 ^{o}C to above the melting point at a rate of 1 ^{o}C/min under confined planner restraint in the shear stage to examine the thermal stability of the sheared-induced shish-kebab structure.

1.3 Results and Discussion

1.3.1 Flow-induced shish formation (without kebabs) at T_c = 142 ^{o}C

Figure 1.1 illustrates selected 2D SAXS patterns for each PE blend (2 and 5 wt%) collected at varying times before and after step shear ($\dot{\gamma} = 100\, s^{-1}$ and shear duration t_s = 5 s) at 142 ^{o}C; Before shear, all three samples exhibited only diffused scattering features, typical of PE melts without ordered structure and preferred orientation. Immediately after shear, however, strong equatorial streaks appeared in both blends, as indicated by arrows in Figures 1.1(b) and 1.1 (c). The appearance of the equatorial streak is consistent with the formation of shish (we speculate that it may be related to the formation multiple shish instead of single shish[10]) having strong electron density contrast between the shish and the surrounding molten matrix.

Figure 1.2 shows selected 2D WAXD patterns of three samples (neat HDPE and two blends) collected before and after shear under the same shearing conditions as those in rheo-SAXS measurements. It was seen that highly oriented equatorial (110) reflection peaks appeared in the blend samples immediately after shear (Figures 1.2(b) and 1.2(c)),

implying that the formation of shish consisted of highly oriented crystals probably with extended-chain conformation. In contrast, the neat HDPE melt did not show any sign of shish formation by both SAXS and WAXD after shear (Figures 1.1(a) and 1.2(a), respectively). We note that SAXS is insensitive to the scatterer with low concentration or with low electron density contrast, thus the absence of equatorial streak in SAXS does not necessary mean the absence of shish. However, the results from subsequent crystallization at lower temperatures (i.e., 137 and 131 ^{o}C), which will be discussed later, confirmed that the shish were not formed in the sheared HDPE melt at 142 ^{o}C since WAXD only exhibited amorphous scattering feature and SAXS indicated completely unoriented lamellar scattering. In other words, the experimental temperature (142 ^{o}C) was sufficiently high to prevent the long chain species in HDPE to sustain the stretched and oriented state under shear.

The appearance of equatorial streak in SAXS and a pair of equatorial (110) reflections in WAXD from the blend samples can be directly attributed to the crystallization of sheared UHMWPE component. Since the concentrations of UHMWPE in both blends were significantly higher than the overlap concentration, c^*, all UHMWPE chains could remain stretched and oriented after shear (although the degrees of extension and orientation were a function of position along the gradient direction, i.e., the sample thickness). This is because the relaxation time, τ, of the polymer chain is scaled with its molecular weight, M, where $\tau \sim M^{3.4}$, where the average relaxation time of UHMWPE chains is an order of magnitude higher than that of HDPE.

It is interesting to note that, even though both blends exhibited the formation of shish, the signature of kebab formation, such as the emergence of meridional scattering

maxima in SAXS, was not seen. This indicates that the chosen experimental temperature only allowed the formation of shish (with a higher melting point) but hindered the formation of kebabs (with a lower melting point) in UHMWPE. In our previous studies, the kebab formation took place at the same time scale, almost immediately after the appearance of shish.[10,11,14,21] The short separation time between the formation of shish and kebabs implied that the nucleation barrier of kebabs at the shish/melt interface was relatively low at lower experimental temperatures. Muthukumar et al. proposed that the nucleation of kebab from the presence of shish involves the adsorption of coiled-chain segments through a diffusion process.[9] It is thus reasonable to argue that when the temperature is high (e.g. close to the equilibrium melting temperature), the mobility of the chain segments may be too high to be adsorbed and stay anchored on the shish. The absence of kebab formation at the chosen experimental temperature (142 ^{o}C) thus can be attributed to the sufficiently high temperature, where coiled-chain segments cannot overcome the secondary nucleation barrier to form folded-chain lamellar crystal.

Although no kebab was formed at 142 ^{o}C after shear, the shish was found to first relax and then grow subsequently in both blends during isothermal conditions after shear. To illustrate this unique behavior, the scattered intensity of shish, I_{Shish}, extracted from the 2D SAXS pattern using the expression, $I_{Shish} = 4\pi \int_{0.0087}^{0.31} \int_{0^o}^{20^o} I(s,\phi) ds d\phi$, ($s$ is the scattering vector, where $s = 2\sin\theta/\lambda$ with θ being the scattering angle and λ being the X-ray wave length, and ϕ is the azimuthal angle) as a function of crystallization time is shown in Figure 1.3. The observed scattered intensity changes in different blends exhibited a similar trend, which could be divided into two stages: the initial decrease at t < ~400 s and the later increase at t > ~400 s; in which a minimum value was seen. The

5/95 wt% blend exhibited notably higher scattered intensity than the 2/98 wt% blend during the entire crystallization stages at 142 ^{o}C after shear. Since the scattered intensity, I_{Shish} (s,ϕ), is proportional to the volume of shish, v, as well as the density contrast between the shish and surrounding matrix, $\Delta\rho$, it can be thought that higher volume fraction of shish or more closely packed shish was formed in the 5/95 wt% blend than that in the 2/98wt% blend. This behavior is certainly consistent with the notation that only the UHMWPE component has crystallized in the blends under the experimental conditions, where the 5/95 wt% blend would result in higher scattered intensity than that of the 2/98 wt% blend. It is interesting to note that immediately after shear, the scattered intensity of the shish decreased first (t < 400 s) in both blends, which suggests that the volume fraction of the shish or the density contrast between the shish and the surrounding matrix in the blend began to decrease (although the latter may be less likely). It is conceivable that the initial shish entity does not contain purely crystalline structure, where the process of crystallization can reduce the internal force and relax some stretched chains, leading to the reduction of the total scattering volume. This can be further explained as follows. The formation of the initial shish is directly related to the deformation of a network of highly entangled chains, where the entanglement points may be embedded in the shish. Upon crystallization of some oriented and extended chain segments, the internal stress on the network will be reduced, leading to the relaxation of stretched chains in the vicinity of extended-chain crystalline shish. Recently, Olmsted *et. al*. have proposed another possibility. That is the interplay between strain and nematic-like orientational interactions of stretched density and orientation fluctuations along the flow axis.[22] In both blends, the scattered intensity of the shish was found to increase at t > 400 s. This can be explained by the growth of extended shish, using the concept of auto-

catalytic process by Peterman et al.[29,30] This will be discussed later. We believe that the final shish structure developed at t > 2500 s contained mainly extended-chain crystals, which would be consistent with the WAXD results.

In order to investigate the time-evolution of the shish structure, the changes of the average shish length, $\langle L_{shish} \rangle$, and the misorientation of shish, B_ϕ, were followed. These parameters were obtained by using the Ruland streak method to analyze the equatorial streak feature in SAXS.[31-33] Ruland demonstrated that the size and orientation distributions of longitudinal voids in polymer and carbon fibers in real space could be estimated from the equatorial streak of SAXS in reciprocal space (as long that the orientation and the longitudinal length of scatterer are finite). Since the method is principally based on the separation of experimentally measured azimuthal breadth from contributions of scatterer length and misorientation, the method can also be applied to separate the average length of shish and its average misorientation. If one assumes that all azimuthal distributions can be modeled by Lorentz functions, the observed azimuthal width, B_{obs}, can be related to the length of shish, $\langle L_{shish} \rangle$, and the azimuthal width, B_ϕ, due to misorientation of shish by the following equation.

$$B_{obs} = \frac{1}{\langle L_{shish} \rangle \cdot s_{12}} + B_\phi \quad \text{(Cauchy-Cauchy)} \qquad (1)$$

If all azimuthal distributions have Gaussian expressions, then the relationship becomes

$$B_{obs}^2 = \left(\frac{1}{\langle L_{shish} \rangle \cdot s_{12}} \right)^2 + B_\phi^2 \quad \text{(Gaussian-Gaussian)} \qquad (2)$$

where B_{obs} represents the integral width of the azimuthal profile from the equatorial streak at s_{12} (the scattering vector $s_{12} = \sqrt{(s_1^2 + s_2^2)} = 2\sin\theta/\lambda$). Based on Equation (1) or

Equation (2), $\langle L_{shish} \rangle$ can be obtained from the slope, and the misorientation width, B_ϕ can be obtained from the intercept of the plots (B_{obs} *vs.* s_{12}^{-1} or B_{obs}^2 *vs.* s_{12}^{-2}). In this study, we found that all azimuthal distributions were better fit with Lorentz functions, thus the plot based on Equation (1) (as shown in Figure 1.4) was used to determine $\langle L_{shish} \rangle$ and B_ϕ.

In addition, the change of the shish cross-section radius, R_C, was examined by analyzing the equatorial streak profile using the Guinier law for rod-like scatterer.[34] According to this law, the scattered intensity of long rod-like scatterer with length, H and the rod radius, R_C, (where $H >> R_C$) can be expressed as

$$I(s) = I_H(s) \cdot I_C(s) \cong H \cdot \frac{1}{2s} \cdot (\Delta\rho)^2 \cdot A^2 \cdot \exp\left(-2\pi^2 R_C^2 s^2\right) \qquad (3)$$

where the scattered intensities, $I_H(s)$ and $I_C(s)$ are related to the length and the cross-section area of rod-like scatterer, respectively. They are given as follows,

$$I_H(s) \cong H \cdot \frac{1}{2s} \qquad (4)$$

$$I_C(s) \cong (\Delta\rho)^2 A^2 \cdot \exp(-2\pi^2 R_C^2 s^2) \qquad (5)$$

where A represents the cross-section area of the rod-like scatterer. Then R_C can be obtained by fitting the linear portion of the $\ln I(s)$ *vs.* s^2 plot at the low s region of the curve (i.e., the minimum of s is equal to 0.0056), where the intensity $I(s)$ was integrated at ϕ = 0-180°. It should be noted that the Guinier approximation is applicable for monodisperse systems when $qR_C < 1$.

The time-evolution of two structure parameters of shish ($\langle L_{shish} \rangle$ and B_ϕ), obtained by the Ruland's streak analysis using Equation (1) for both blends is shown in Figures 1.5(a) and 1.5(b). The corresponding change of the shish diameter (R_C), obtained

by the Guinier analysis, is shown in Figure 1.6. In Figure 1.5, the value of $\langle L_{shish} \rangle$ in the 2/98 wt% blend was found to decrease at t > ~400 s, while the shish orientation increased (i.e., B_ϕ decreased). The decrease in $\langle L_{shish} \rangle$ and the increase in shish orientation can be explained by the partial relaxation of the stretched UHMWPE chain network after shear, where some defective and less oriented shish crystals may melt due to entropic recovery of the stretched chains.. It was interesting to see that in the 2/98 wt% blend, $\langle L_{shish} \rangle$ began to increase at t > 400 s, accompanying by a decrease in the shish orientation. The increases in the shish length can be attributed to the growth of shish, while the decreases in shish orientation suggests that the growth process took place in stretched chain segments that were partially relaxed (thus resulting in decreasing orientation). Figure 1.6 indicates that the shish diameter (R_C) remained almost about constant with time (a very slight decrease was seen). Keller *et al*.[29] and Petermann *et al*.[30] reported that the shish can undergo longitudinal growth in deformed polymer solution, where the growth process is accomplished by pre-oriented (mesomorphic) chains. The driving force for the longitudinal growth of shish can be attributed to the free energy difference between the formation of shish and the relaxation of stretched "mesomorphic" melts. They argued that if the growth rate of the shish is relatively slow with respect to the relaxation time of the stretched chains, the local orientation of newly formed shish would be reduced. Our results in the 2/98 wt% UHMWPE/HDPE blend are certainly consistent with the mechanism proposed by Keller *et al*.[29] and Petermann *et al*.[30]

The behavior of the 5/95 wt% blend was slightly different from that of the 2/98% blend. Although the value of $\langle L_{shish} \rangle$ decreased and the shish orientation increased

(i.e., B_ϕ decreased) in the initial stage, these values also exhibited the same trend at the late stage (except at the intermediate stage where both $\langle L_{shish} \rangle$ and B_ϕ decreased). In general, the starting values of $\langle L_{shish} \rangle$ and B_ϕ were higher in the 5/95 wt% blend than those of the 2/98 wt% blend, indicating the latter formed a network of shorter but more oriented shish. This is consistent with our earlier concept[21] that the flow-induced shish-kebab precursor structure comes mainly from the entangled chains of high molecular weights (e.g. UHMWPE). In the lower concentration blend (2/98 wt% UHMWPE/HDPE), the UHMWPE chains are less entangled, forming a lose network with a fewer number of "crosslinking" (entanglement) points. In the higher concentration blend (5/95 wt% UHMWPE/HDPE), the UHMWPE chains are more entangled, resulting in a dense network with more "physical crosslinking" (entanglement) points. Consequently, under the same shear conditions (i.e., $\dot{\gamma} = 100\, s^{-1}$, t_s = 5 s and the strain unit $\gamma_s = 500$), the loosely entangled network could be oriented more (due to the smaller modulus) but formed shorter shish length (due to lower concentration); whereas the dense entangled network could be oriented less (due to the higher modulus) but led to longer shish length (due to higher concentration). It is interesting to see that although both blends exhibited the growth process of shish in the intermediate stage, the growth behavior in the higher concentration blend (5/95 wt% UHMWPE/HDPE) was much weaker and lasted for a shorter period of time than that in the lower concentration blend (2/98 wt% UHMWPE/HDPE). This behavior is certainly consistent with the concept of flow-induced network structure containing shish-kebabs from the highly entangled UHMWPE species. It is also interesting to note that in Figure 1.5(a), the shish length

became nearly identical (i.e., $\langle L_{shish} \rangle \approx 950$ nm) at the late stage of the shish-kebab formation ($t \approx 2500$ s). Perhaps, this is because the final shish length is thermodynamically dependent (rather than dynamically dependent), which should be the same at the same crystallization temperature.

During the shish-kebab formation, the R_C values for both blends were found to decrease very slightly (Figure 1.6). The negative slope indicates that the later formed shish probably had a thinner average diameter, which is consistent with the relaxation of stretched chains decreasing the amount of stretched chains that can participate in the shish growth. It is interesting to see that the 5/95 wt% blend generally exhibited a larger R_C value than the 2/98 wt% blend. This also agrees with the notion that as the concentration of the UHMWPE component increases, more UHMWPE chains can be involved in the shish formation leading to a larger R_C value. However, since the difference in R_C between the two blends is small, this indicates that the concentration of UHMWPE is not a strong factor affecting R_C. Instead, the concentration of UHMWPE seems to be a dominant factor affecting the number (concentration) of shish.

1.3.2 Subsequent kebab formation at $T_c = 134\ ^oC$

After being held at 142 ^oC for 45 min, the once-sheared melts were rapidly cooled to 134 ^oC (at a -30^oC/min rate) to investigate the subsequent crystallization (mainly from the kebab growth). Selected 2D SAXS patterns obtained from the samples immediately after reaching 134 ^oC are shown in Figure 1.7. Again, the sheared HDPE melt only exhibited the diffused scattering feature, confirming that the matrix was in the

molten state at 134 ^{o}C without ordered structure and orientation. In both blends, however, SAXS patterns clearly showed the emergence of two meridional scattering maxima due to the kebab formation. This is because the kebabs grow perpendicularly to the shish axis through the folded-chain crystallization process. The layered kebab structure can be considered as the initial template for the formation of lemallar stacks. During the crystallization at 134 ^{o}C, the shish lengths and the shish orientations for each blend were almost constant as seen in Figures 1.8(a) and 1.8(b). Furthermore, these values were identical to those observed at the final stages of crystallization at 142 ^{o}C (Figures 1.5(a) and 5(b)). This suggests that the crystallization at 134 ^{o}C was mainly due to the kebab growth, where the shish structure became nearly stablized.

To follow the evolution of the kebab growth as well as the further change of shish at 134 ^{o}C, scattered intensities from shish and kebabs were separated from the SAXS patterns for both blends (Figures 1.7(b) and 1.7(c)), and the results are illustarted in Figure 1.9(a) and 1.9(b) respectively. The scattered intensities from shish and kebabs were integrated using the following expressions $I_{Shish} = 4\pi \int_{0.0087}^{0.31} \int_{0^o}^{20^o} I(s,\phi) ds d\phi$ and $I_{Kebab} = 4\pi \int_{0.0087}^{0.31} \int_{20^o}^{90^o} I(s,\phi) ds d\phi$. It was seen that the intensities of shish and kebabs increased rapidly at the initial stage in both blends, while such increases slowed down at later times. Since the average shish length in each blend remained almost constant at 134 ^{o}C (Figure 1.8(a)), the initial increase of the scattered intensity by shish is probably due to the increase in density contrast, $\Delta\rho$, between the shish and the surrounding matrix during subsequent crystallization at lower temperature.

The emergence of meridianal scatteing was due to the kebab growth. In Figure 1.9, the 5/95 wt% blend showed stronger total scattered intensity than the 2/98 wt% blend

during entire crystallization stages (note that the unit scale in 5/95 wt% is much higher than that in 2/98 wt%). Since the 5/95 wt% blend possesed a higher concentration of shish (thus a higher number of nucleation site) than the 2/98 wt% blend, the formal should result in a higher volume fraction of coiled chains for forming kebabs. The number of kebab is associated with the nucleation density on the shish, the growth of kebab is associated with the diffusion of the coiled segments onto the shish. It is conceivable that the growth rate of kebabs (diffusion controlled) is not the same as the growth rate of spherulites in transcrystallization, which is combination of nucleation and growth.

Figure 1.10 shows the changes of long period (L_{sp}) in the kebab assembly for each blend determined from the 2D *rheo*-SAXS patterns in Figure 1.7. This long period represents the sum of the kebab thickness, L_c and the amorphous thickness between the kebabs, L_a; $L_{sp} = L_c + L_a$. It is seen that the kebab long period increased rapidly in the initial stages and slowed down at later times. In the past, the increase of kebab long period has been attributed to the surface melting of kebab crystals and the subsequent recrystallization for form more stable and thicker crystals.[35-37] This can also be the case here. The stability of kekab crystals (folded-chain lamellae) is related to the ratio of bulk free energy (σ) and surface free energy (μ), σ/μ. When the crystal thickens, the σ/μ ratio increases and the crystal stability is enhanced. One often observes such a phoenomenon at crystallization temperature near the melting point, T_m, where large chain mobility permits small crystals to melt and large crystal to thicken to a more stable state. Peterlin demonstrated that the rate of crystal thickening increases with crystallization temperature, T_c, by the following equations;[36]

$$L_{sp}(t) = W \log t + p \qquad (6)$$

where, W is the rate of crystal thickening and p is a constant. The inset in Figure 1.10 shows the plot of $L_{sp}(t)$ *versus* log t, where the rates of crystal thickening for two blends are almost identical. This is reasonable since the rate of thickening is mainly dependent on crystallization temperature, not chain entanglement or flow condition. This also implies that the growth of kebabs in two different blends takes place mainly in the coiled segments of UHMWPE, which has the same diffusion rate thus resulting in the same thickening rate.

It is interesting to note that the kebab long period in the 2/98 wt% blend was less (Figure 1.10) than that in the 5/95 wt% blend at the same crystallization temperature. This has the following implication. Earlier, we observed that the 5/95 wt% blend possesed a higher concentration of shish (thus a higher number of nucleation site) than the 2/98 wt% blend, the total number of nucleated kebabs thus would also be higher in the 5/95 wt% blend. Since both L_{Shish} and L_{sp} values are known, the nucleation density of kebabs per shish, I, can be calculated by the ratio of L_{Shish}/L_{sp} (the result was listed in Table 1.1). It is seen that the nucleation density of kebab per shish was higher in the 2/98 wt% blend than in the 5/95 wt% blend. In other words, the nucleation density per shish decreased as the concentration of shish increased. This phoenomenon has also been observed in our previous studies, but it was not reported. The behavior is associated with the respective concentrations of nucleating shish and surrounding crystallizable coiled chains. A simple scenario one can conclude is that the 2/98 wt% blend contained more crystallizable coiled chains surrounding the shish, whereas the 5/95 wt% blend possessed more shish with less crystallizable coiled chains surrounding the shish. This is possible as

the 5/95 wt% blend may form a dense shish network, where more UHMWPE chains are under strained conditions. As the amount of crystallizable coiled chains surrounding the shish is higher in the 2/98 wt% blend than the 5/95 wt% blend, the former would result in a higher nucleation density per unit shish as seen experimentally.

Selected *rheo*-2D WAXD patterns collected during crystallization in the sheared melts (neat HDPE and UHMWPE/HDPE blends) at 134 ^{o}C are shown in Figures 1.11(a), 1.11(b) and 1.11(c), respectively. These *rheo*-2D WAXD patterns were obtained under the same condition as *rheo*-2D SAXS patterns in Figures 1.7(a), 1.7(b) and 1.7(c). It was seen that WAXD patterns of the once-sheared HDPE sample exhibited no sign of crystallization at 134 ^{o}C. In contrast, WAXD patterns of both sheared blends exhibited 2-bar oriented (110) reflections on the equator at the initial times (e.g. 20 s) and the superposition of weak but discernible 2-arc (110) reflections around the equator with increasing time (e.g. 400 s). The 2-bar equatorial (110) reflections can be attributed to the extended-chain UHMWPE crystals (shish) formed at 142 ^{o}C, while the board 2-arc equatorial (110) reflections can be attributed to the folded-chain UHMWPE crystals (kebabs) formed at 134 ^{o}C. It was interesting to see that the 2-arc (110) reflections gradually transforms into 4-arc off-axis (110) reflections at the later time. The off-axis (110) reflections are associated with the formation of twisted kebabs. This can be explained as follows. The transformation of (110) reflections from equatorial 2-arc to off-axis 4-arc features is due to the rotation of reciprocal lattice vector, r_{110}^{*}, from the step of initiation to twisting during kebab growth. In the transformation, both *a*- and *c*-axes rotate along the *b*-axis, resulting in the turning of r_{110}^{*} along the azimuthal angle, which leads to first broadening and eventually off-axis splitting of (110) reflections.[20]

Changes of the (110) reflection intensities from shish and kebabs for each blend are illustrated in Figure 1.12 (results were obtained from Figures 1.11(b) and 1.11(c), where the (110) reflections by shish and kebabs are indicated). The separation of the (110) reflections from shish and kebab was carried out by curve-fitting of the integrated azimuthal profiles using Gaussian functions. However, prior to this process, the following procedures were applied first. To correct the missing intensity due to the use of flat-plate detector, the measured intensity at given scattering vector and azimuthal angle, $I_{110}(s,\phi)$, was multiplied by a correction factor, $s^2\sin(90\text{-}\phi)$.[34,38] Thus, the total integrated intensity of the (110) reflection can be given as: $I_{110,T}(s,\phi) = I_{110,S}(s,\phi) + I_{110,K}(s,\phi)$, where $I_{110,S}(s,\phi)$ represents the integrated intensity from shish and $I_{110,K}(s,\phi)$ represents the integrated intensity from kebabs. In addition, the following relationship also holds: $I_{110,T}(s,\phi) = 4\pi\int_0^\infty s^2 ds\int_0^{\pi/2}\sin(90^o-\phi)d\phi I(s,\phi)$. Since the kebab intensity is proportional to the volume fraction of kebabs or folded chain crystals (V), $I_{110,K}$ $(t) \propto V(t)$, the time-dependence of the kebab intensity may directly reflect the time-evolution of kebab volume, especially at the initial stage of crystallization. As a result, a simplified Avrami equation[39] was used to analyze the kebab intensity to investigate the nucleation and growth of kebabs.

The general Avrami equation (Equation (7)) has been routinely used to study the crystallization kinetics of polymers.[40]

$$v_c = 1-\exp(-Kt^n) \tag{7}$$

Since the volume fraction of crystal attained is less than 1, the general Avrami equation for polymer crystallization can be expressed as follows.[41]

$$\frac{v_c(t)}{v_c(\infty)} = 1-\exp(-Kt^n) \tag{8}$$

where $v_c(t)$ and $v_c(\infty)$ are volume fractions of crystal at time t and at infinite time (∞), K is the rate constant and n is the Avrami exponent. The following relationship also holds for X-ray diffraction data, $v_c(t)/v_c(\infty) \propto V \propto I_c(t)/I_c(\infty) \propto I_c(t)$, where $I_c(t)$ and $I_c(\infty)$ are diffraction intensities of crystal at time t and infinite time (∞). Since the expression $\exp(-Kt^n) \approx 1-Kt^n+\cdots$, one can simplify the Avrami expression as follows,[39-41]

$$I_c(t) \sim kt^n \tag{9}$$

or

$$\log I_c(t) \sim \log k + n \log t \tag{10}$$

Thus, from the changes in the (110) intensity at the initial stages of crystallization, the Avrami exponents, n, and the constant, k (which is related to the rate constant, K) can be obtained from the simplified Avrami plot as shown in Figure 1.13. The Avrami exponent n and the constant k obtained from such analysis are listed in Table 1.2. It is seen that the estimated Avrami exponents at the initial stage of kebab formation for each blend are about the same ($n \approx 1$), which indicates the kebabs following the 2D growth geometry under athermal (spontaneous) nucleation and diffusion-controlled crystallization conditions.[41,42] Since the constant k is related to the crystallization rate, the results imply that the kinetic of kebab growth was much faster in 5/95 wt% blend than in 2/98 wt% blend under the same crystallization conditions. If the nucleation process and the growth geometry of kebab are pre-determined, the growth rate of kebab is governed by the diffusion rate of chain segments to the lateral face of shish, whereas the amount of kebabs formed at a given time is associated with the density of nucleation. Since the average diffusion length of crystallizing chain segments to the shish surface is a function of the shish concentration, the kebab growth rate also depends on the shish concentration. Thus,

as the average diffusion length of crystallizing chain segments is shorter in 5/95 wt% blend than in 2/98 wt% blend, the kebab growth rate in 5/95 wt% blend is higher. This is consistent with the experimental observations.

1.3.3 Probing the stability of shish-kebab structure in once-sheared melts by confined heating

The stability of shish (formed at 142 ^{o}C) and kebabs (formed at 134 ^{o}C) in once-sheared melts was examined by confined heating using the following procedures. The flow-induced crystallized samples were heated at 1 ^{o}C/min under the planar constraint conditions in the Linkam shear device. The changes of scattered intensities by shish and kebabs in each blend upon melting are illustrated in Figure 1.14. Both blends exhibited total melting of kebabs at about the same temperature (T_m≈140 ^{o}C), which implies that the isothermal crystallization of two sheared blends with different UHMWPE concentrations at 134 ^{o}C formed kebabs of an identical thickness distribution. In other words, although the kebab development can be mediated and prompted by shearing of different blends, the kebab growth in both systems follows the thermodynamics of crystallization. In our previous study, we reported that the equilibrium melting temperature of polyethylene (PE) folded-chain crystals (kebabs) obtained from constrained melting of sheared sample was T_m^o ≈ 142.6 ^{o}C.[43] Even though this value is lower than the theoretical value of equilibrium melting temperature for PE, T_m^o ≈145.5 ^{o}C, the estimated value in this study is in good agreement with the experimental data determined by Wunderlich[5], T_m^o ≈141.5 ^{o}C (in their study, the lamellae were formed

under an equilibrium condition in the absence of flow, and the melting was proceeded without constraint). The above observations clearly indicated that the crystallization and melting of kebabs are governed by thermodynamics as unstrained or non-sheared melts.

In Figure 1.14, the melting of shish for the two blends exhibited two stages: the initial melting at $T \leq 140$ ^{o}C, where the temperature range was identical to that of kebabs observed earlier; and the later melting at $T \geq 140$ ^{o}C. The two-stage melting behavior in shish can be understood by the following experimental observations. Figure 1.15 illustrates changes of shish length and shish orientation, which were about constant at $T \geq 140$ ^{o}C. The initial decrease of scattered intensity in Figure 1.14 are probably associated with the decrease of packing density in extended-chain crystals and thus leads to the decrease in density difference (scattering contrast), $\Delta\rho$, between the shish and surrounding molten matrix. It is interesting to note that the melting points of shish for both blends were higher than the theoretical equilibrium melting temperature (145.5 ^{o}C). This may be explained as follows. Different from kebabs, the growth and melting of shish in both blends are dominated by non-equilibrium factors, imposed by stretched chains and entanglement network. Since the dimension of sample was confined under planar constrained condition during crystallization and melting, the stretched chain could not freely relax upon melting. As a result, the nominal melting point of shish increased to a level higher than the equilibrium melting temperature, $T_m^o = 145.5^{o}$C. This has also been observed in two UHMWPE systems: (1) extended-chain crystals of drawn UHMWPE fibers, which shows an increased melting temperature higher than the equilibrium melting temperature, (2) the phase transition from orthorhombic to hexagonal phase in oriented

UHMWPE, where the transition temperature is also higher than the equilibrium melting temperature.[44,45]

Even though the external constraint applied to the sheared melts was constant and the observed structure parameters, such as the shish length, is about the same in both blends, the nominal shish melting temperature in 5/95 wt% blend was higher than that in 2/98 wt% blend (i.e., 153 ^{o}C *vs.* 148 ^{o}C in Figure 1.15). This may be explained as follows. The melting of shish is accompanied by the topological relaxation of stretched UHMWPE chains in the entanglement network (the total number of entanglement is higher in 5/95 wt% blend than 2/98wt% blend due to the concentration effect). We note that the chain entanglement is a dynamic process which forms and disappears. In the supercooled state, when the chain dynamics is slow, one may assume the entangled melt behaves as a physical network. The shear deformation would generate two populations of UHMWPE chain segments with different orientations: (1) stretched chain segments, which are oriented along the flow direction and are confined by the "frozen" entanglement points, and (2) unperturbed chain segments (or coiled segments).[12] As a result, only a fraction of UHMWPE can be oriented by flow and participate in the shish formation, while others remain in the unperturbed state but they are connected to and surround the shish. Since the total number of entanglement in the 5/95 wt% blend is higher than that in the 2/98wt% blend, the former has a higher thermal stability. This is seen in Figure 1.15, where both blends exhibit the increase in shish length and the decrease in shish orientation (the higher B_{ϕ} value, the higher shish misorientation) with the 5/95 wt% blend having higher thermal stability. It is interesting to see that the average shish lengths for both blends were about the same, but the 5/95 wt% blend exhibited a

higher shish misorientation, probably due to the stronger entanglement network that would recoil faster upon stress relaxation.

1.4 Conclusions

In-situ rheo-SAXS and *rheo*-WAXD studies were carried out to investigate flow-induced crystallization of UHMWPE/HDPE blends, where UHMWPE chains (with long relaxation times) play the major role in forming the entanglement network. The combined SAXS and WAXD results confirmed that the shear-induced shish formation at 142 ^{o}C was mainly originated from UHMWPE chains. The final shish lengths in two blends (2/98 wt% and 5/95 wt%) were about the same within the experimental error, even though the UHMWPE compositions were quite different. The identical shish length in these two blends might be due to the identical strain (ε=500) imposed on the supercooled and restrained melts. As the temperature decreased to 134^{o}C, both blends exhibited the formation of kebabs, where growth process was diffusion-controlled rather than nucleation-controlled. Even though the total nucleation number of kebab was higher in the 5/95 wt% blend, the nucleation density of kebab per unit shish was higher in the 2/98 wt% blend. This could be attributed to the different concentrations of shish and crystallizable coiled chains in the sheared melts. The once-sheared (at 142 ^{o}C) and crystallized (at 134 ^{o}C) samples were subject to subsequent heating under planar constraint to investigate the thermal stability of shish-kebab structure. Both blends exhibited an identical melting temperature of kebabs, indicating that the kebab stability is dictated by the thermodynamics of coiled chains. In contrast, the high melting

temperature of shish indicates that the shish stability is dictated mainly by the thermodynamics of stretched chains under the planar constrained conditions.

1.5 Reference

1. Keller A. *Faraday Discussions of the Royal Society of Chemistry*, **1979**, 68, 145.

2. Hill M. J.; Keller, A. *J. Macromol Sci (Phys.)***, 1969**, B3, 1531.

3. Keller, A.; Kolnaar, H. W. *Mater. Sci. Technol*, **1997**, vol 18, 189.

4. Ward, I. M. *Structure and Properties of Oriented Polymers*, Wiley, New York, **1975**.

5. Wunderlich, B. *Macromolecular physics*, vol 2, Academic Press, New York, **1973**.

6. Wilkinson, A. N.; Ryan, A. J. (Eds.), *Polymer Processing and Structure Development*, Kluwer, Dodrecht, **1998**.

7. Pennings, A. J.; Kiel, A. M. *Colloid. Z. Z. Polym*. **1965**, 205. 160.

8. Nadkarni, V. M.; Schultz, J. M. *J. Polym. Sci. Phys. Ed*. 1977, 15, 2151.

9. Dukovski, I.; Muthukumar, M. *J. Chem. Phys*. **2003**, 118, 6648.

10. Hsiao, B. S.; Yang, L.; Somani, R. H.; Carlos, A. A.; Zhu, L. *Phys. Rev. Lett*, **2005**, 94, 117802.

11. Keum, J. K.; Burger, C.; Hsiao, B. S.; Somani, R. H.; Yang, L.; Chu, B.; Kolb, R.; Chen, H.; Lue, C. *Prog. Colloid Polym. Sci.*, **2005**, 130, 114.

12. Zuo, F., Keum, J. K.; Yang, L.; Somani, R. H.; Hsiao, B. S. Macromolecules, **2006**, 39, 2209.

13. Seki, M.; Thurman, D. W.; Oberhauser, J. P.; Kornfield, J. A. *Macromolecules*, **2002**, 35, 2583.

14. Somani, R. H.; Hsiao, B. S.; Nogales, A.; Srinivas, S.; Tsou, A. H.; Sics, I.; Balta Calleja, F. J.; Ezquerra, T. A. *Macromolecules*, **2000**, 33, 9385.

15. Jerschow, P.; Janeschitz-Kriegl, H. *Int. Polym. Process*. **1997**, 12, 72.

16. Vleeshouwers, S.; Meijer, H. *Rheol. Acta*, **1996**, 35, 391.

17. Duplay, C.; Monasse, B.; Haudin, J. M.; Costa, J. L. *J. Mater. Sci.,* **2000**, 35, 6093.

18. de Gennes, P. G.; *J. Chem. Phys.*, **1974**, 60, 5030.

19. Schroeder, C. M.; Babcock, H. P.; Shaqfeh, E. S. G.; Chu, S. *Science*, **2003**, 301, 1515.

20. Kolnaar, J. W. H.; Keller, A. *Prog. Col. Polym. Sci.*, **1993**, 92, 81.

21. Yang, L; Somani, R. H.; Sics, I.; Hsiao, B. S.; Kolb, R.; Fruitwala, H.; Ong, C. *Macromolecules*, **2004**, 37, 4845.

22. Olmsted, P. D.; Milner, S. T. *Macromolecules,* **1994**, 27, 6648.

23. Murase, H.; Kume, T.; Hashimoto, T.; Ohta, Y. *Macromolecules,* **2005**, 38, 8719.

24. Olmsted, P. D.; Poon, W. C. K.; McLeish, T. C. B.; Terril, N. J.; Ryan. A. J. *Phys. Rev. Lett.,* **1998**, 81, 373.

25. Hoffman, J. D.; Lauritzen, J. I. Crystallization of Bulk Polymers with Chain Folding: *Theory of Growth of Lamellar Spherulites*, *J. Res. Natl. Bur. Stand.* ***1961,*** 65A, 297.

26. de Gennes, P. G. *Scaling Concepts in Polymer Physics*; Cornell University Press: Ithaca, NY, **1979**.

27. Takahashi, Y.; Isono, Y.; Noda, I.; Nagasawa, M. *Macromolecules* **1985**, *18*, 1002.

28. Fetters, L. J.; Lohse, D. J.; Garcia-Franco, C. A.; Brant, P.; Richter, D. *Macromolecules* **2002**, 35, 10096.

29. Liberwirth, I.; Loos, J.; Petermann, J.; Keller, A. *J. Polym. Sci. Polym. Phys*. **2000**, 38, 1183.

30. Petermann, J.; Miles, M.; Gleiter, H. *J. Polym. Sci. Polym. Phys*. **1979**, 17, 55.

31. Ruland, W. *J. Polym. Sci. Polym. Sym.*, **1969**, 28, 143.

32. Ruland W.; Perret, R. *J. Appl. Cryst*. **1969**, 2, 209.

33. Ruland W.; Perret, R. *J. Appl. Cryst*. **1970**, 3, 525.

34. Guinier, A.; Fournet, G. *Small-angle scattering of X-rays*, New York: wiley;**1955**.

35. Fisher, E. W.; Schmidt, G. F. *Angew. Chem*. 1962, 74, 551.

36. Peterlin, A. *Macromol. Chem*. **1964**, 74, 107.

37. Hikosaka, M.; Amano, K.; Rastogi, S.; Keller, A. *Macromolecules* **1997**, *30*, 2067.

38. Fraser, R. D.B.; Macrae, T.P.; Miller, A.; Rowlands, R.J. *J . Appl. Cryst*. **1976**, 9, 81

39. Keum, J. K; Burger, C.; Zuo, F.; Hsiao, B.S. *Polymer* **2007**, 48, 4511.

40. Avrami, M. J. *Chem. Phys*. **1939**, 7,1103.

41. Gedde, U. W. *Polymer Physics*, Chapman & Hall; New York, **1995**.

42. Hiemenz, P.C. *Polymer Chemistry: The Basic Concepts* Marcel Dekker, New York, **1984**, 219.

43. Keum, J. K.; Somani, R. H.; Zuo, F.; Burger, C.; Sics, I.; Hsiao, B. S.; Chen, H.; Kolb, R.; Lue, C. *Macromolecules*, **2005**, 38, 5128.

44. Bassett, D. C.; Block, S.; Piermarini, G. J. *J. Appl. Phys*. **1974**, 45, 4146.

45. Tashiro, K.; Sasaki, S.; Kobayashi, M. *Macromolecules*, **1996**, 29, 7460.

Table 1.1 Nucleation density of shish for the UHMEPE/HDPE blend.

	2/98 UHMWPE/HDPE blend	5/95 UHMWPE/HDPE blend
Nucleation density per shish (I)	15.2	12.4

Table 1.2 Avrami exponent, *n*, and the constant, *k* (related to Avrami rate constant, *K*) of the UHMWPE/HDPE blend.

	2/98 UHMWPE/HDPE blend	5/95 UHMWPE/HDPE blend
n	1.1	1.2
k	3.1	19.1

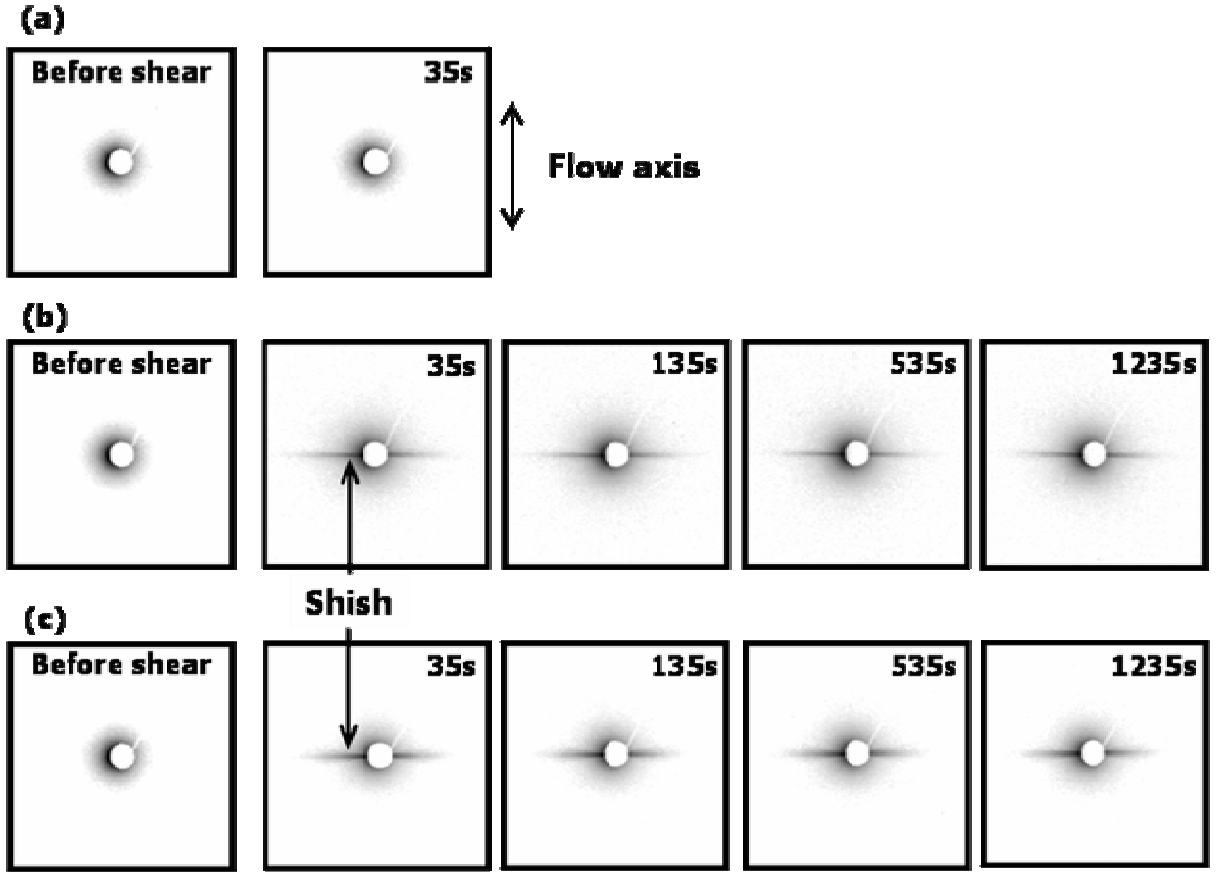

Figure 1.1 (a), (b) and (c)

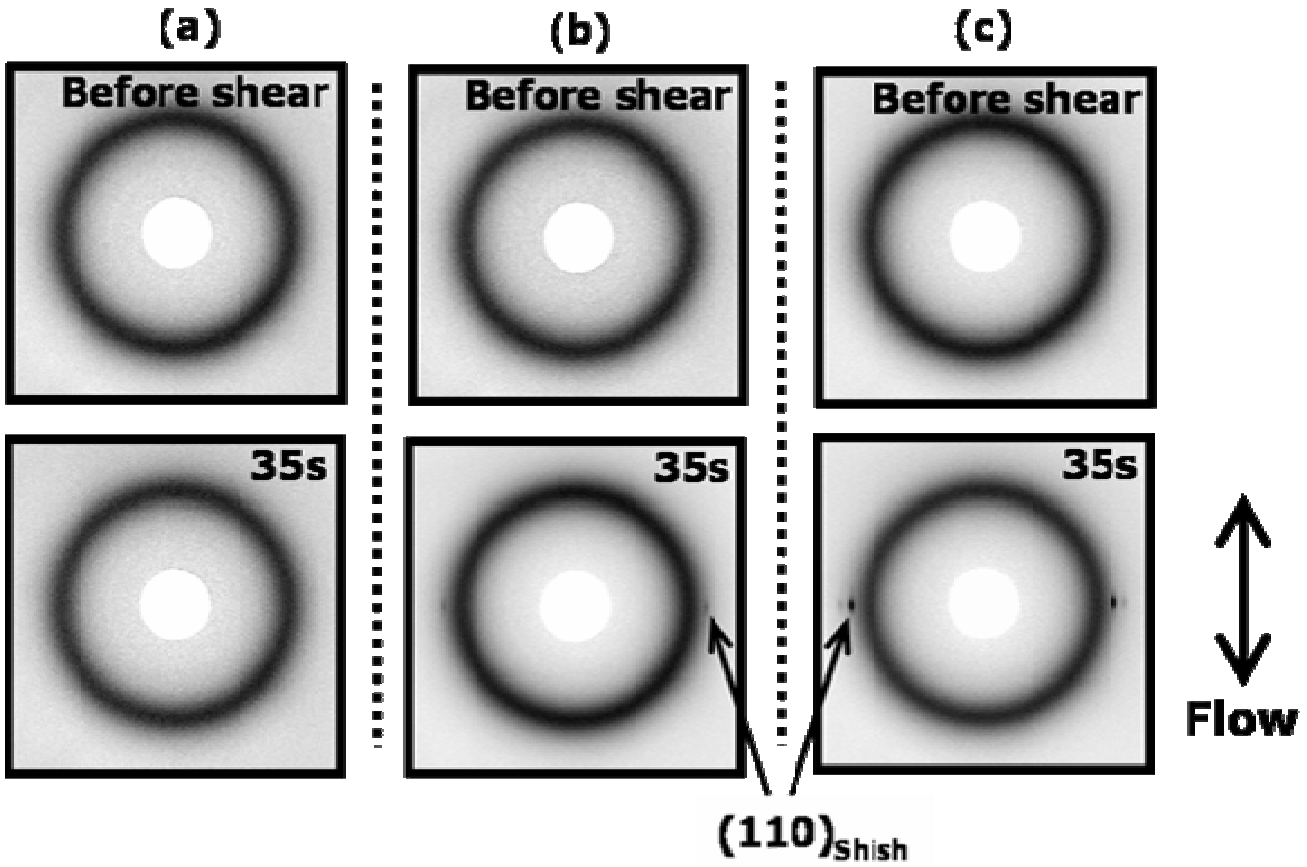

Figure 1.2(a), 1.2(b) and 1.2(c)

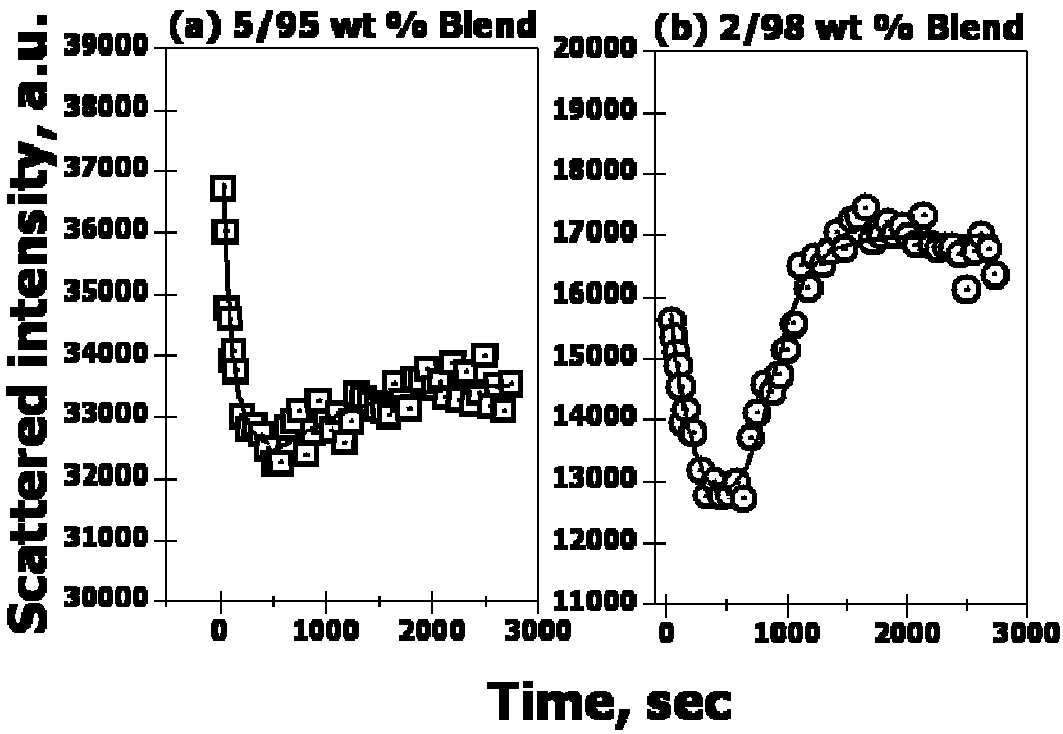

Figure 1.3(a) and 1.3(b)

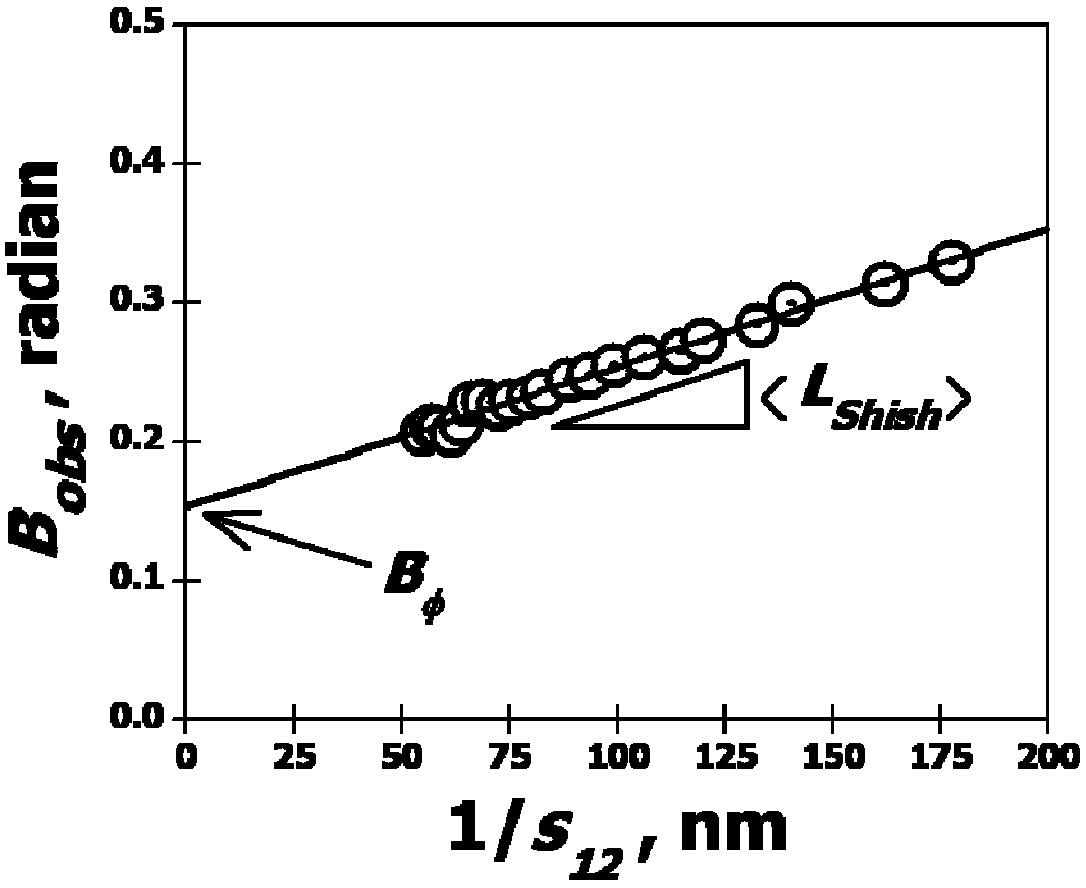
0.5
0.4
0.3
0.2
0.1
0.0
0
25
50
75
100
125
150
175
200
B_{obs}, radian
$1/s_{12}$, nm
$\langle L_{Shish} \rangle$
B_ϕ

Figure 1.4

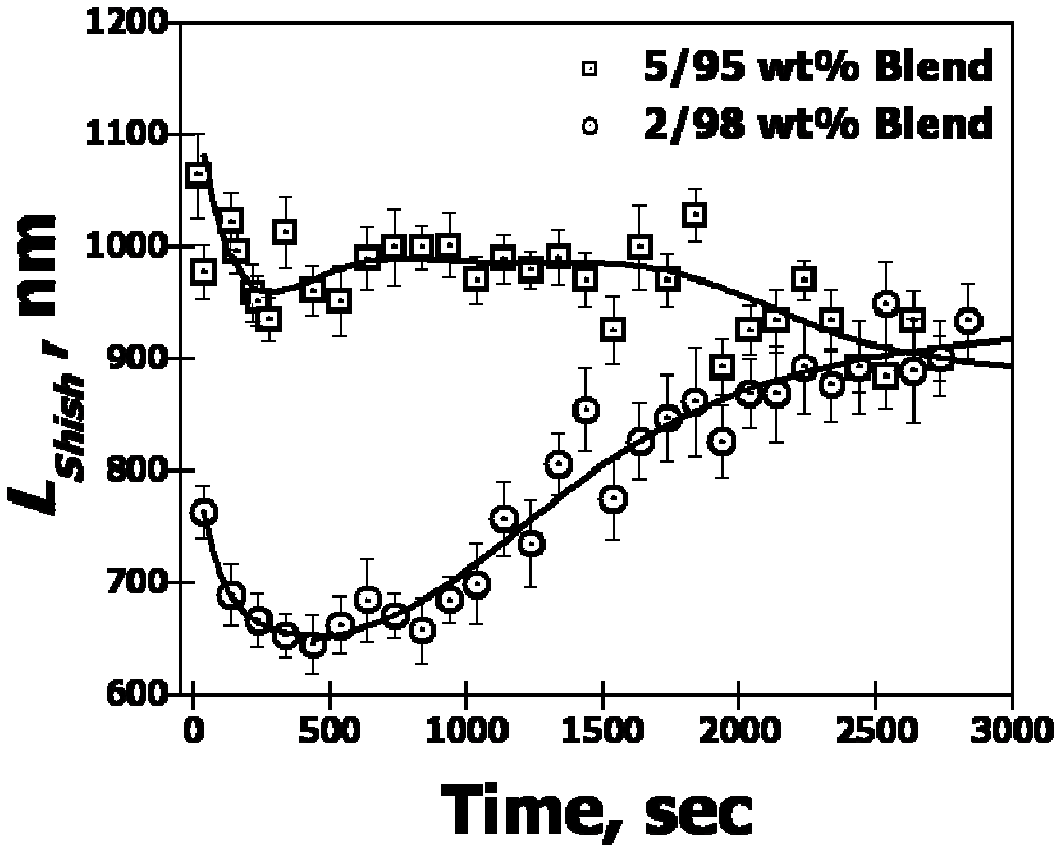
5/95 wt% Blend
2/98 wt% Blend
L_{shish}, nm
Time, sec
1200
1100
1000
900
800
700
600
0
500
1000
1500
2000
2500
3000

Figure 1.5(a)

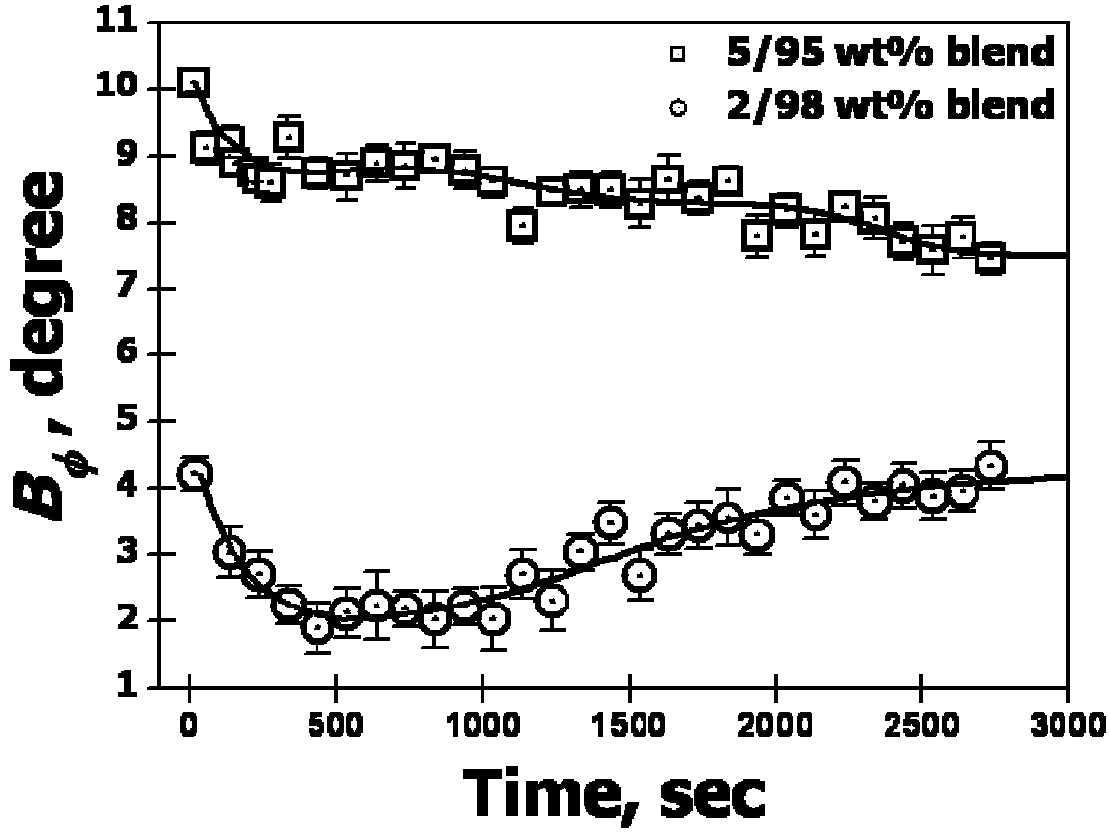
5/95 wt% blend
2/98 wt% blend
B_{ϕ}, degree
Time, sec
11
10
9
8
7
6
5
4
3
2
1
0
500
1000
1500
2000
2500
3000

Figure 1.5(b)

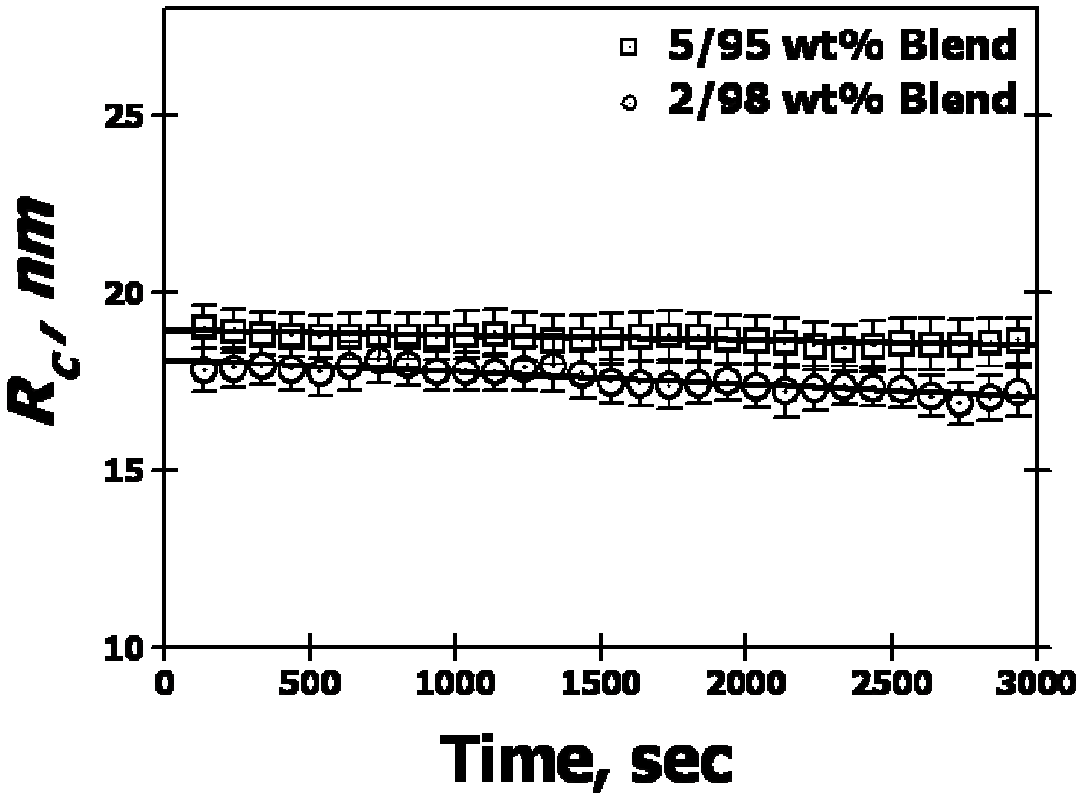
5/95 wt% Blend
2/98 wt% Blend
R_c, nm
25
20
15
10
0
500
1000
1500
2000
2500
3000
Time, sec

Figure 1.6

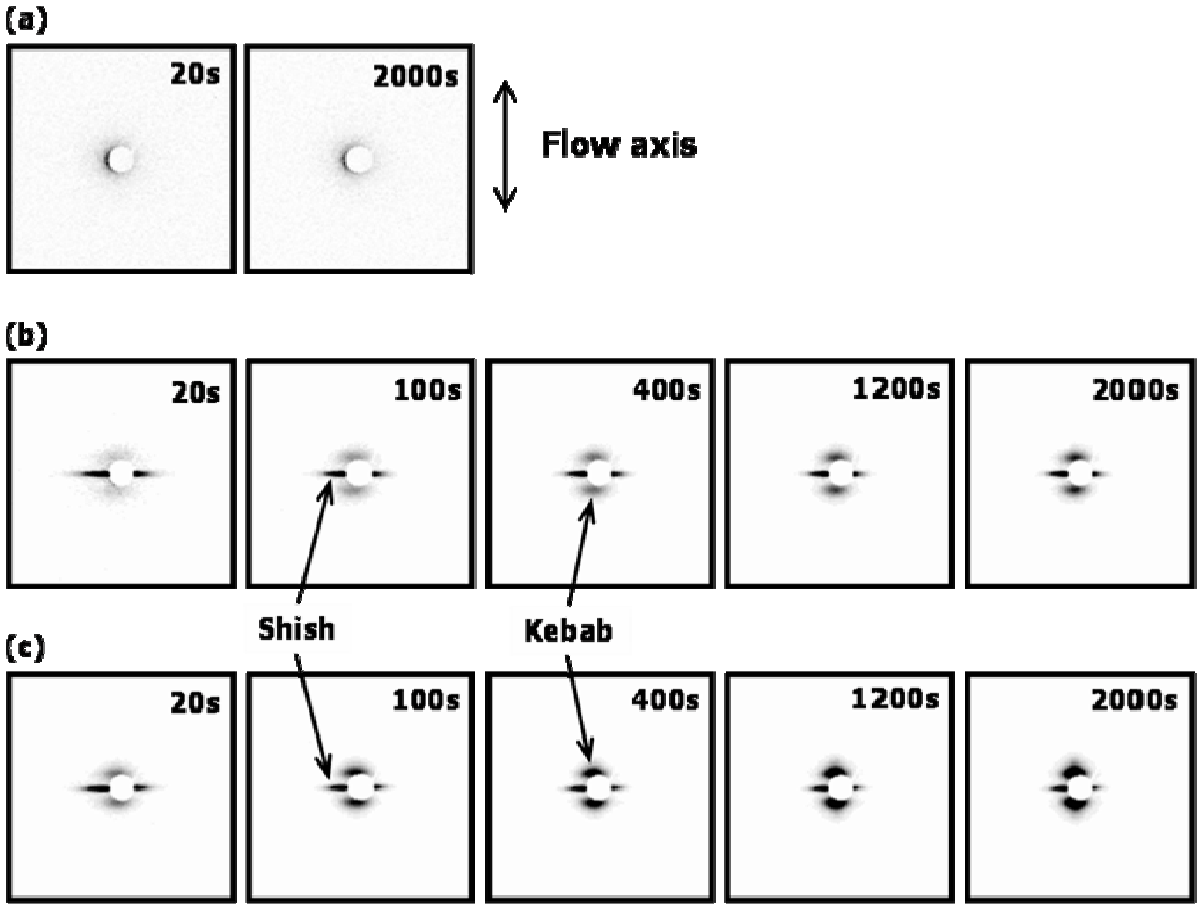

Figure 1.7 (a), 1.7(b) and 1.7(c)

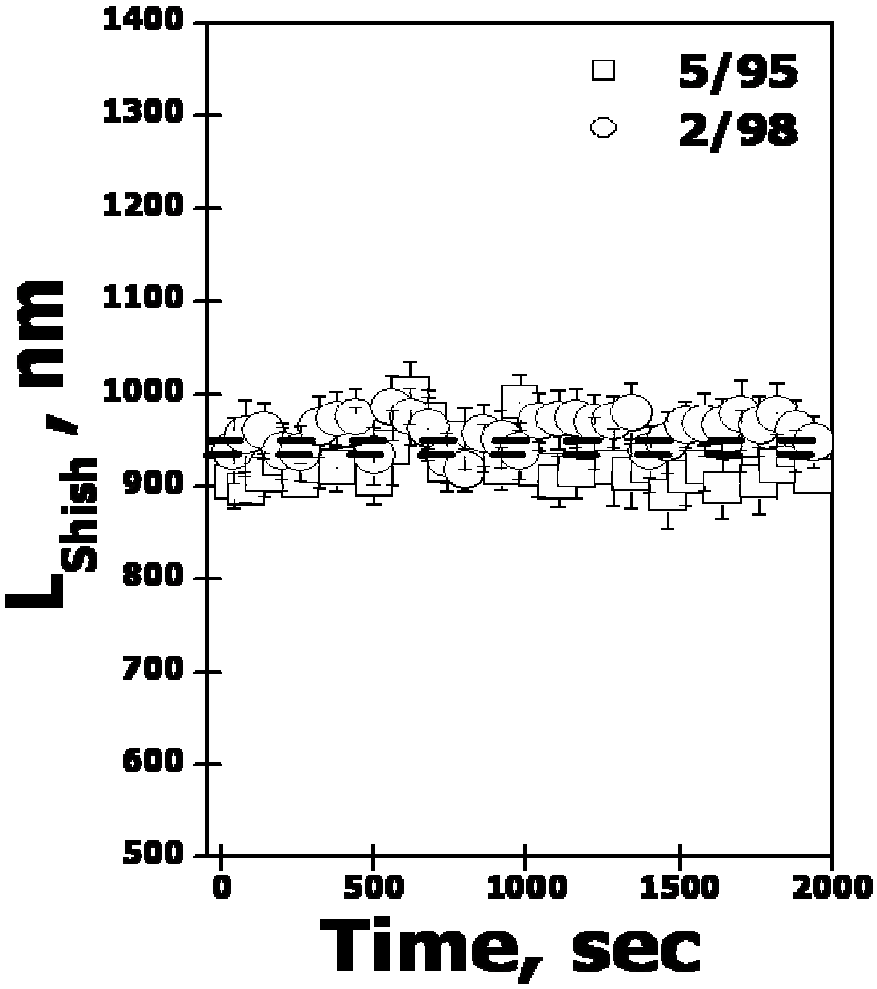
1400
1300
1200
1100
1000
900
800
700
600
500
0
500
1000
1500
2000
5/95
2/98
L Shish / nm
Time, sec

Figure 1.8(a)

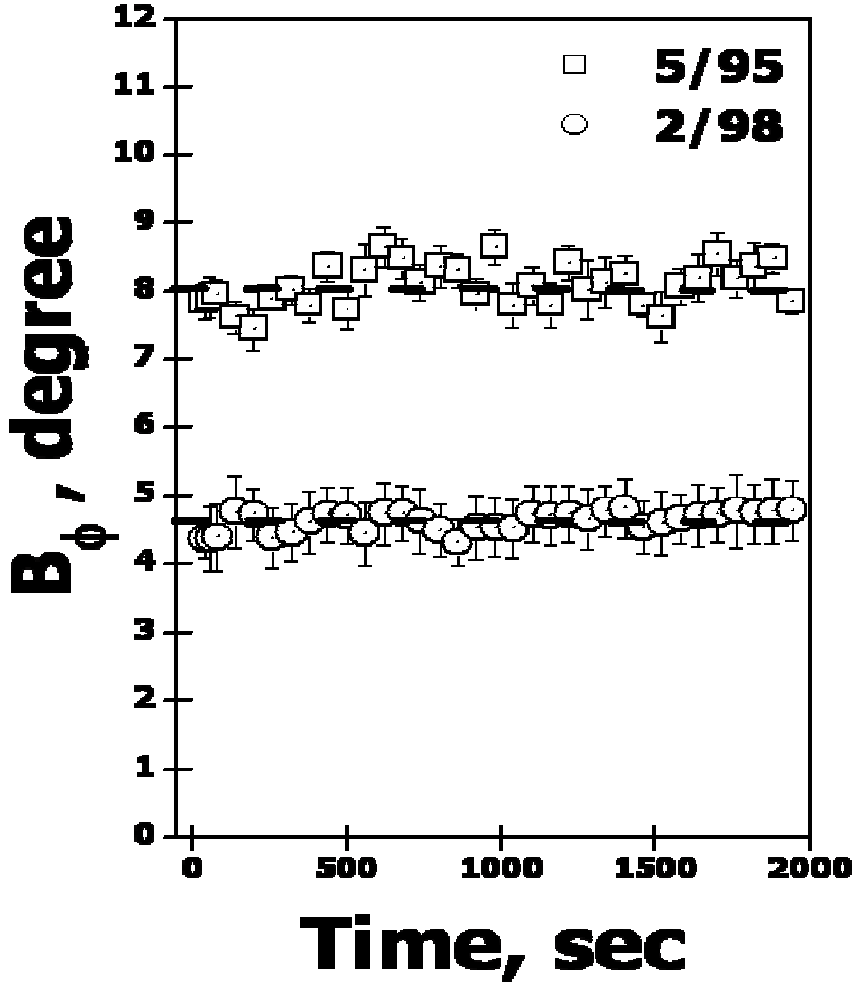
5/95
2/98
B_ϕ, degree
Time, sec
0
1
2
3
4
5
6
7
8
9
10
11
12
0
500
1000
1500
2000

Figure 1.8(b)

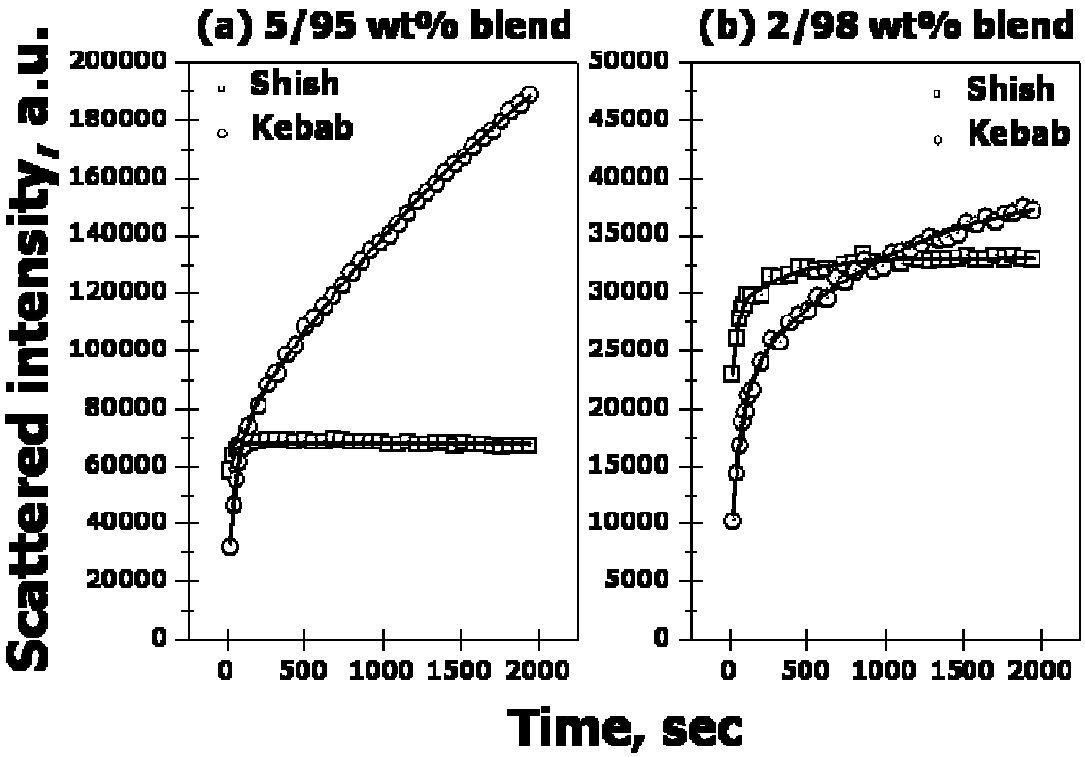
(a) 5/95 wt% blend
(b) 2/98 wt% blend
Shish
Kebab
Shish
Kebab
Scattered intensity, a.u.
Time, sec
200000
180000
160000
140000
120000
100000
80000
60000
40000
20000
0
50000
45000
40000
35000
30000
25000
20000
15000
10000
5000
0
0
500
1000
1500
2000
0
500
1000
1500
2000

Figure 1.9

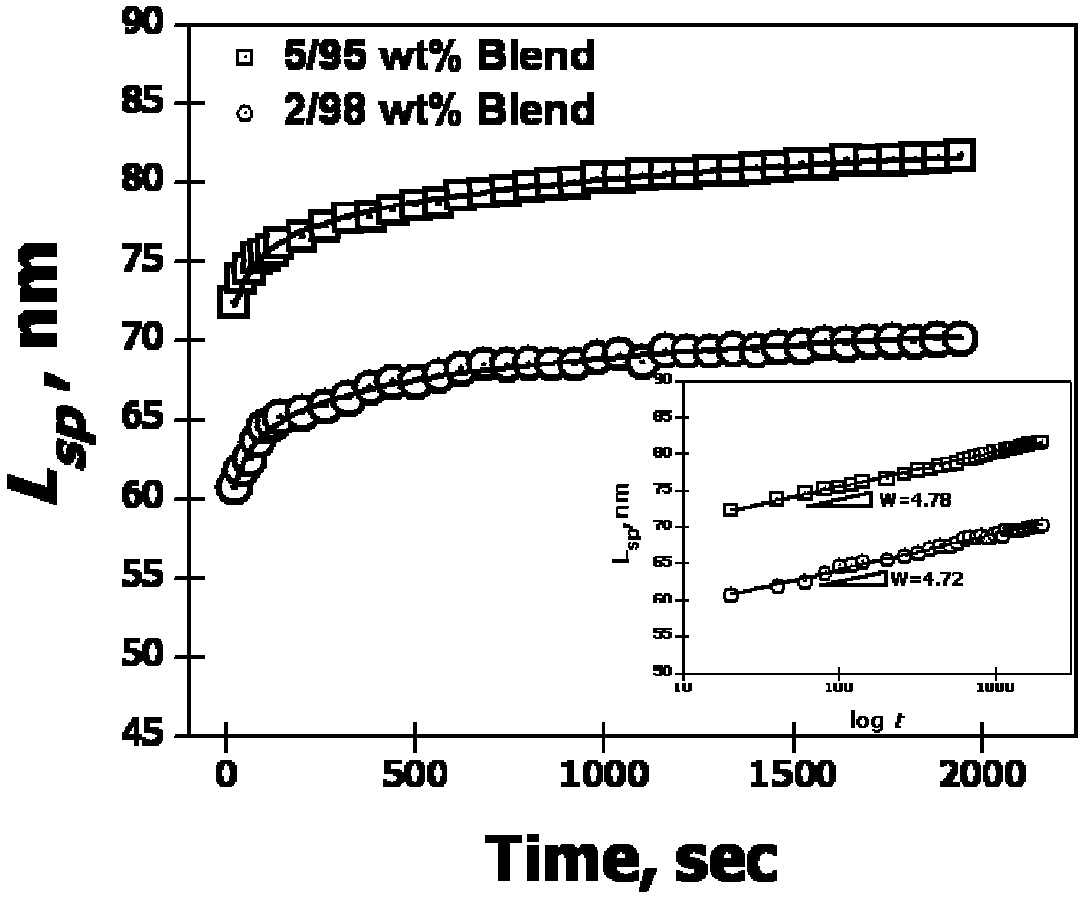

Figure 1.10

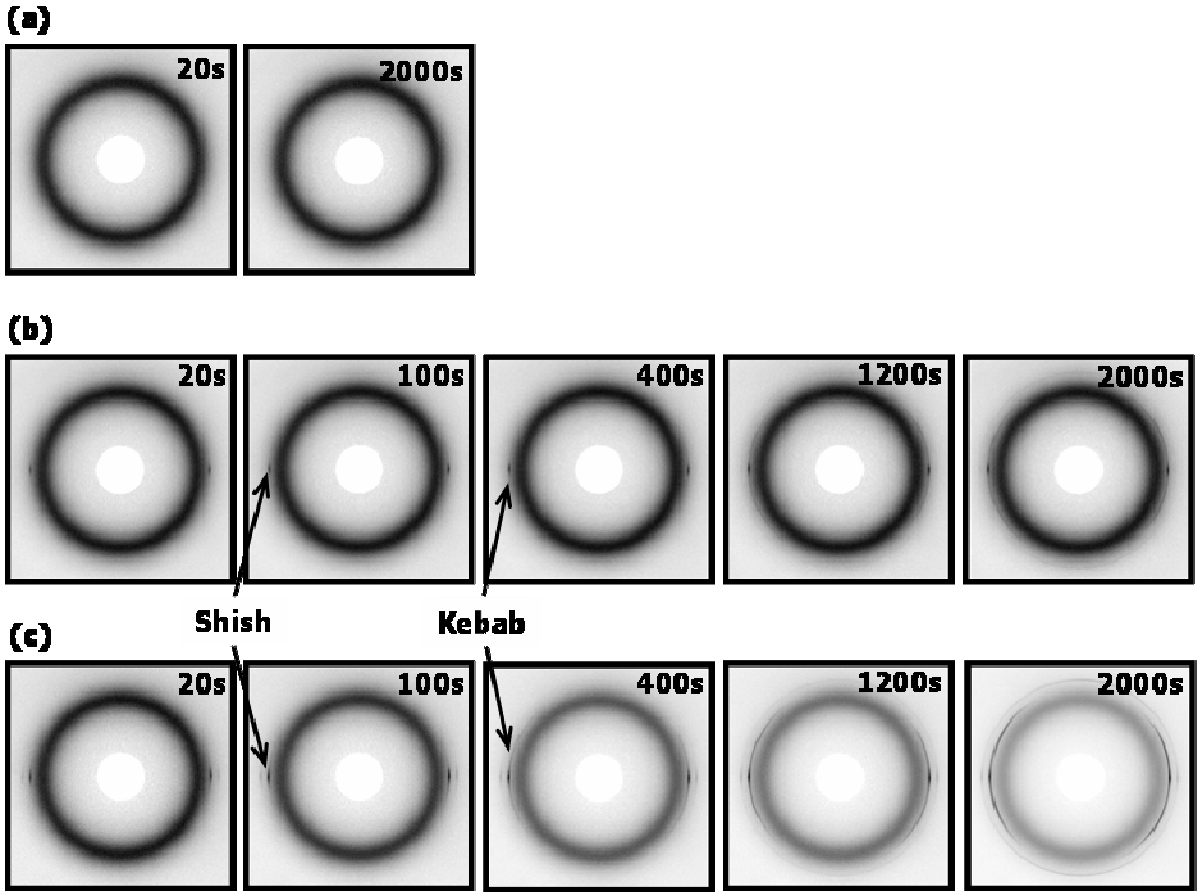

Figure 1.11 (a), 1.11(b) and 1.11(c)

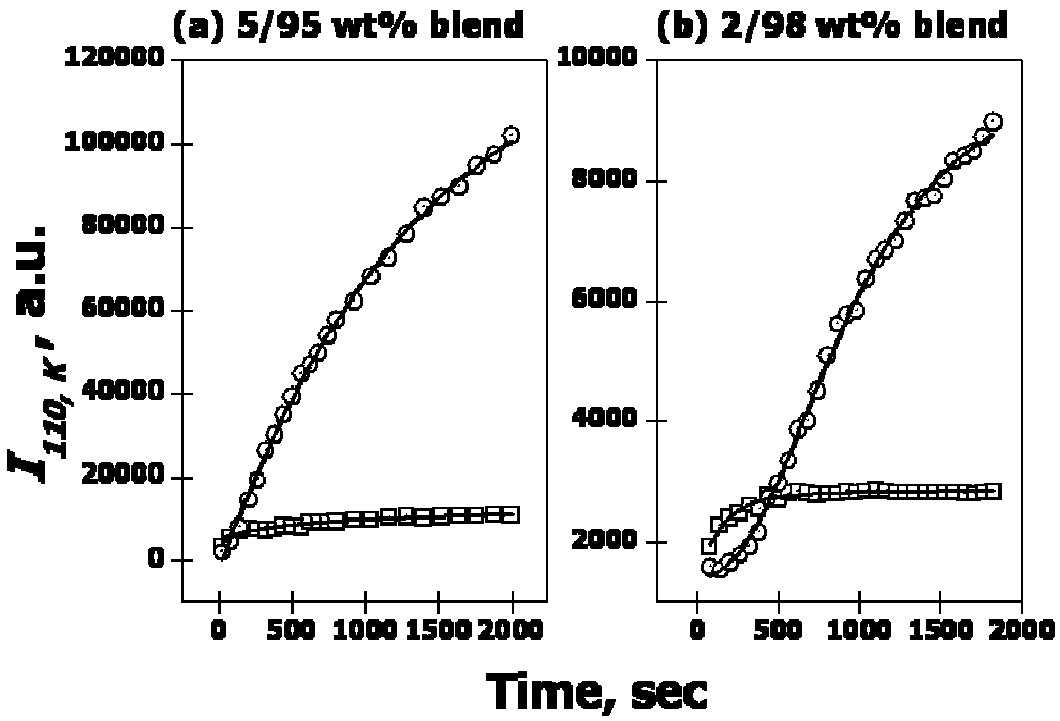

Figure 1.12(a) and 1.12(b)

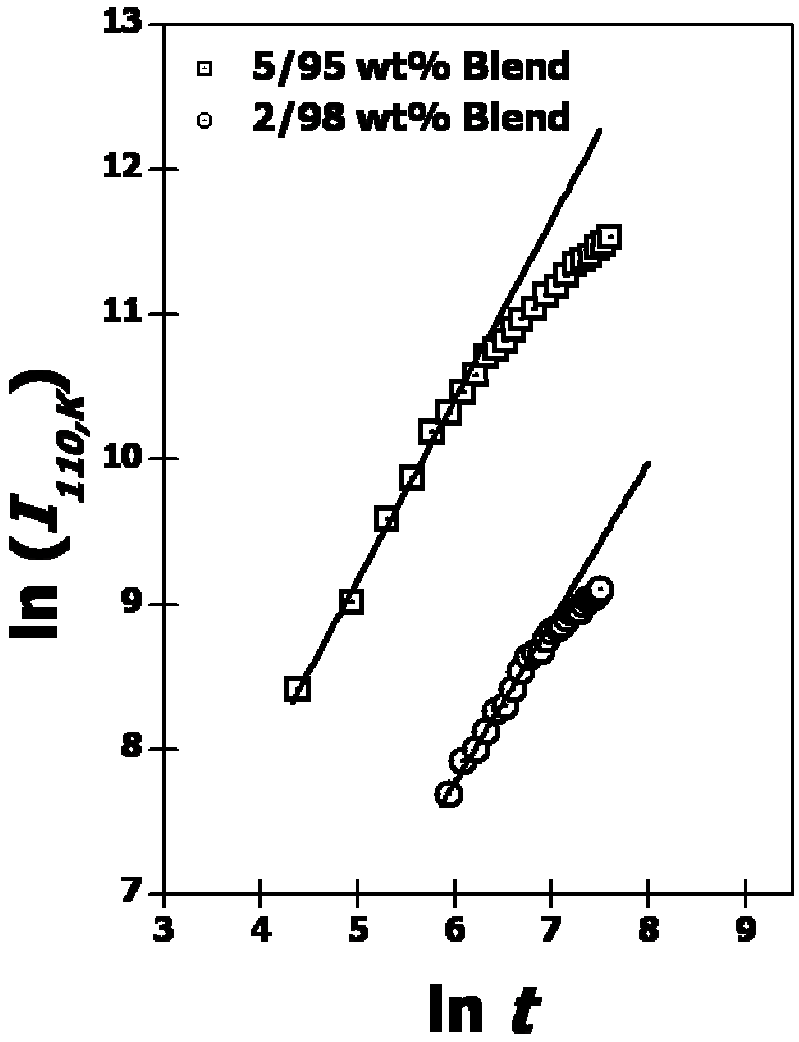

Figure 1.13

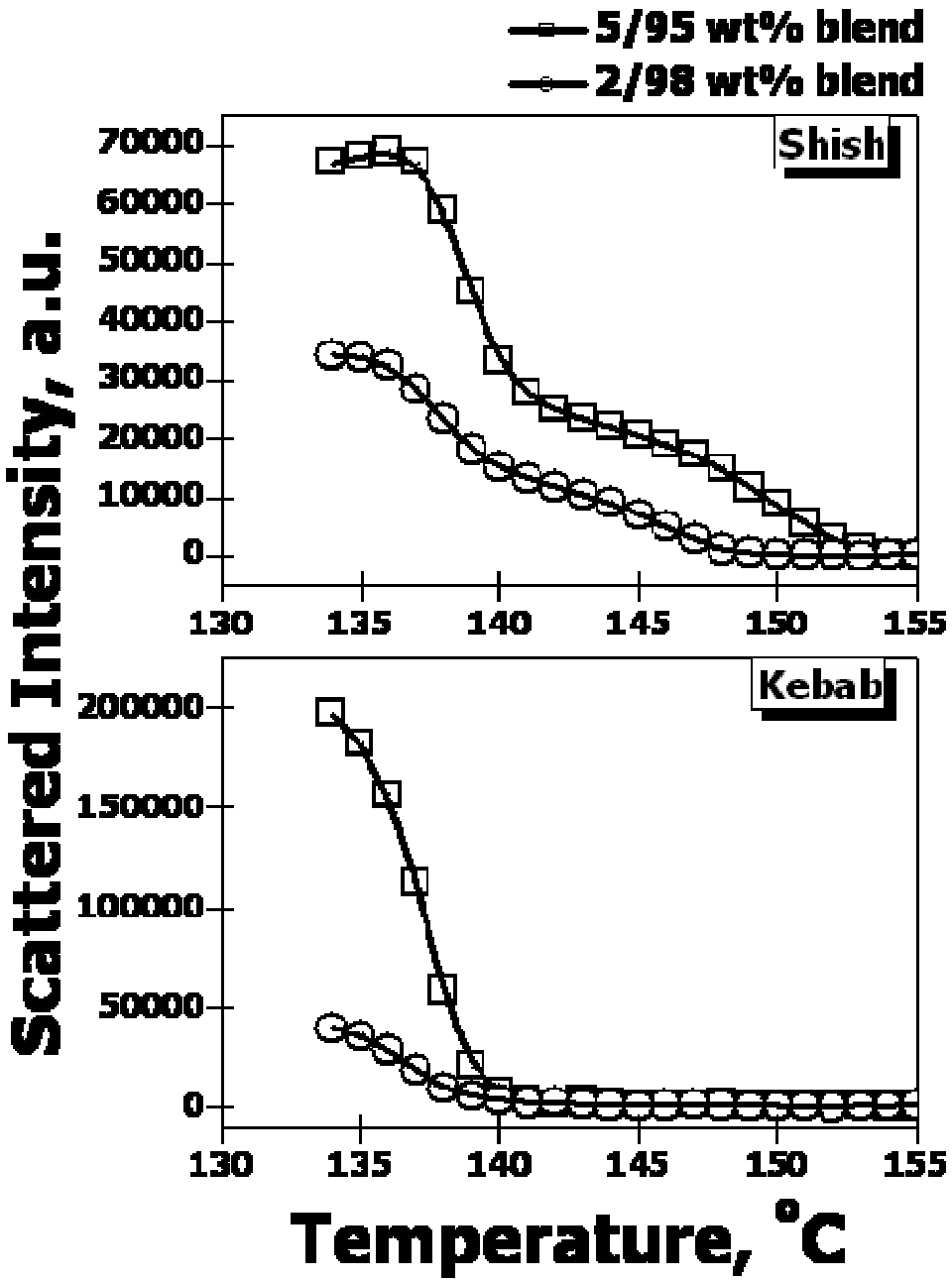
5/95 wt% blend
2/98 wt% blend
Shish
Kebab
Scattered Intensity, a.u.
Temperature, °C
70000
60000
50000
40000
30000
20000
10000
0
200000
150000
100000
50000
130
135
140
145
150
155

Figure 1.14

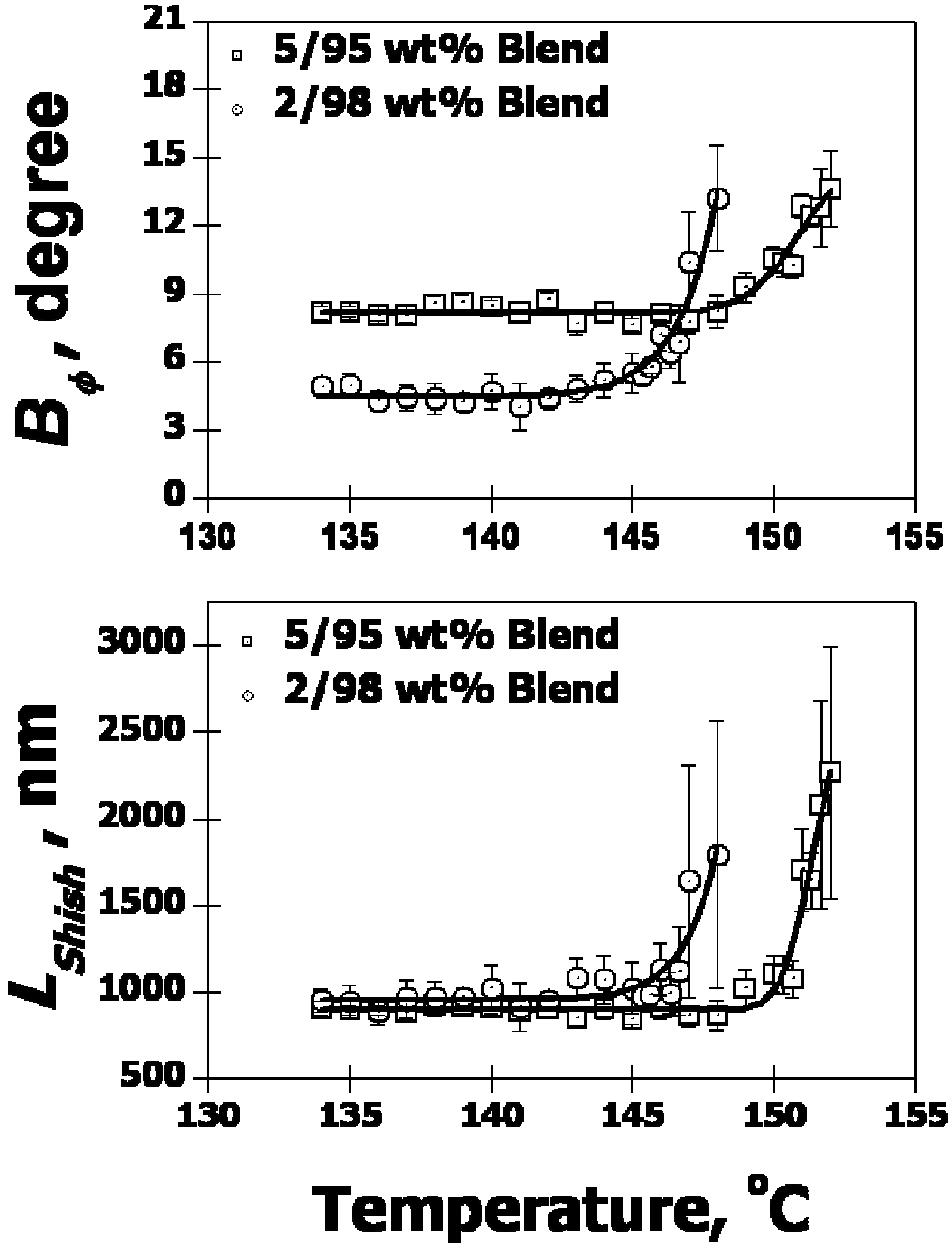
5/95 wt% Blend
2/98 wt% Blend
B_{ϕ}, degree
21
18
15
12
9
6
3
0
130
135
140
145
150
155
5/95 wt% Blend
2/98 wt% Blend
L_{shish}, nm
3000
2500
2000
1500
1000
500
130
135
140
145
150
155
Temperature, °C

Figure 1.15

Chapter 2. A Unique Cross-Slot Flow Device for the Investigation of Extensional Flow-Induced Crystallization in Entangled Polymer Melt Using Synchrotron X-Rays

2.1 Introduction

Flow-induced crystallization of semicrystalline polymer has long been an important subject in both academic and industry.[1-7] In industrial forming processes, since polymer chains are long covalently-bonded and thus are highly anisotropic, they highly tend to align along the axis of mechanical strain field during processing. Varying flow strength can result in different morphologies, which lead to different properties of the final products. Recent studies undoubtedly indicated that the final morphology of polymer product is indeed dominated by the pre-existing state of chain stretching induced by flow and the subsequent formation of flow-induced crystallization precursor structure (i.e. shish).[8-14]

The chain stretching induced by flow, prior to the formation of flow-induced crystallization precursor, has long been coupled to the concept of coil-stretch transition which was first proposed by de Gennes decades ago based on the chain dynamics in dilute polymer solutions.[15] For concentrated polymer solution or polymer melts, Keller also adopted the concept, whereby he proposed the twofold criticality in the coil–stretch transition.[1] That is, for a monodisperse polymer melt, there exists a critical strain rate ($\dot{\varepsilon}_c$) and, for a polydisperse polymer melt under a given strain rate, there exists a critical orientation molecular weight (M) in the molecular weight distribution. The former indicates that, in a monodisperse polymer solution or melt, the polymer chains can be

stretched only when the strain rate level reaches $\dot{\varepsilon}_c$, whereas, the latter means that, in a polydispersed solution or melt at a fixed strain rate, only the chains longer than *M* will be stretched while the rest of shorter chains remains in random-coiled state without experiencing the transition. In the latter case, increasing strain rate increases the amount of chains that becomes stretched by decreasing *M* in the molecular weight distribution. Based on the above findings, it has been hypothesized that the final morphology of oriented polymers, i.e. fibers and blown films, is a consequence of the pre-existing state of stretched chain induced by flow, where the high molecular weight tail in the molecular weight distribution plays a much more important role than the rest of shorter chains. For example, the shish-kebab structure consisting of an extended-chain crystal (shish) and folded-chain lamella (kebabs) is thought to be the direct evidence of the coil-stretch transition of polymer chains in which the stretched chains (higher molecular weight species) forms shish while the coiled chains (lower molecular weight species) crystallize into kebabs. However, the coil-stretch transition at the whole chain length level in highly concentrated polymer solution or entangled polymer melt is still controversial.[8,12] That is because it is very doubtful that long and highly entangled chains disentangles and undergoes the coil-stretch transition under typical experimental flow conditions. Instead, it is believed that the topological deformation of highly entangled species (entanglement network) in the melt directly results in generations of partially stretched and coiled chain segments between entanglement points, where the stretched chain segments form shish (i.e., extended-chain crystal or oriented mesomorphic structure) which finally facilitates the folded-chain crystallization (kebab formation) of nearby coiled chain segments.[7]

It has been suggested that the fractional extension of polymer chain under flow is governed by the nature of the flow, i.e., simple shear, extension-dominant and

extensional flow.[8,16] In fact, the most of practical flows are mixed flow consisted of both rotational and extensional components and the resulting degree of fractional deformation of polymer chain is highly dependent on the relative magnitudes of each component. In a simple shear flow, recognizing as the magnitude of extensional and rotational components are equal, it is believed that polymer chains may not form a stable, highly stretched state. Instead, large fluctuation in chain extension is observed. This is because the stretched state can be destabilized by the tumbling effect of rotational component. In an extension-dominant flow, on the other hand, one can expect more stable and larger fractional deformation of polymer chain than the polymer chains in a simple shear flow. Thus, some insightful curiosities about the stable and high chain stretching, and the subsequent flow-induced nucleation process are still remained. The cross-slot flow cell may generate the extension-dominant flow that can achieve the stable and high chain stretching.

Wide-angle X-ray diffraction (WAXD) and small-angle X-ray scattering (SAXS) using Synchrotron radiation source are powerful tools in investigating the dynamic changes of polymer structure during polymer processing.[17-21] For example, the *in-situ* anisotropic structural changes of polymer under shear[18,19], stretching[20] and spinning[21], can be directly investigated by using intense synchrotron radiation source. Thus, a great deal of studies of polymer forming processes using synchrotron X-ray techniques has been carried out during the past decades and the studies are well documented.[17] Among the studies, the dynamic structural evolution (i.e. shish-kebab formation) of semicrystalline polymer in deformed melts has often been studied by using in-situ WAXD and SAXS. However, the most of the flow-induced crystallization studies of polymer melt have been focused on the crystallization in a shear flow. The extensional

flow-induced crystallization study in polymer melt in extension dominant cross-slot flow, however, is rare.[1,22-24]

Thus, in chapter 2, we have devised a unique cross-slot flow device, generating extensional flow at the central location of outflow channel across the stagnation point for the purpose of synchrotron X-ray studies and have tested the extensional flow-induced crystallization of isotactic poly(propylene) (*i*PP). The cross-slot flow device largely consisted of two main parts, e.g., polymer melt feeding apparatus and cross-slot flow cell. It was found out that the device could apply reproducible extensional flow field to polymer melt at the stagnation point.

2.2 Instrumentation

2.2.1. Sample feeding apparatus

Figure 2.1 shows a polymer melt feeding apparatus mounted with cross-slot flow cell. The apparatus was composed of two square-shaped upper and lower optical platforms (610 × 610 mm), four pillars (610 mm in length × 70 mm in diameter) supporting the optical platforms at the corners, barrel (260 mm in length × 15.3 mm in inner diameter) and motor-driven plunger (250 mm in length × 15.3 mm in diameter). The barrel was located on the upper optical platform of this apparatus, which could store the maximum ~46000 mm^3 of polymer melts (solutions or gels) with a temperature capability from room temperature to 300 °C. The heating of barrel was attained by temperature controller connected with three band heaters and thermocouple. The temperature was feedback-controlled by PID. Since the thermocouple measured the

temperature of the barrel, a digital thermometer with thin thermocouple was used to measure and calibrate the real temperature of sample by dipping the thin thermocouple into the melt. The motor-driven plunger was used to drive the polymer melt from the barrel to a cross-slot flow cell (Figure 2.2). A fine stepping motor was used to achieve better precision control in feeding polymer melts into the cross-slot flow cell. In order to avoid the corrosion of metal surface, i.e. in case using solvent, the barrel was built by B2/B10 metal. With the aid of stepping motor, the top platform could be moved vertically over a distance range of ~ 15 cm with 0.2 mm precision. Also, two pairs of precision optical rails mounted on the lower optical platform led the upper platform to move horizontally along the direction perpendicular to incident X-ray beam over a range of ~ 20 cm. The two adjustable movements, e.g. vertical and horizontal movements, of this apparatus were very useful to align the sample at the X-ray beam position.

2.2.2 Cross-slot flow cell

A schematic diagram of the cross-slot flow geometry is given in Figure 2.3. By driving the polymer melt from barrel into the two inlet channels and forcing it to flow through a pair of opposing outflow channels the extensional flow field was created along the central outflow plane across the stagnation point. The cross-slot flow cell was composed of two pieces of metal blocks, shims, X-ray windows and Kapton films as depicted in Figures 2.4(a) and 2.4(b). Each part was numbered as from 1 to 9 in Figure 2.4(a) for the better representation. The metal block (1) had a dimension of 64 × 44 × 8 mm with cylindrical aperture of 5 mm in diameter × 8 mm in height. The aperture led the incident X-ray beam to hit the sample. The other metal block (7) had the same dimension

with metal block 1 but it possessed conic aperture with 5 mm in inner diameter × 15 mm in outer diameter to avoid the blocking of diffracted or scattered X-ray beam at the edges of metal block (7) and shims (4 and 5). The resultant maximum diffraction angle, 2θ, available for X-ray measurement was ~ 35°. Inflow and outflow channels were built by inserting uniquely designed two pieces of shims (4 and 5) between the two metal blocks. The dimension of channel formed by the assembly of metal blocks and shims was 2 × 2 × 42.5 mm (height, H × depth, D × channel length, CL). All the corners of the channel around the stagnation point were rounded with a radius, R. In order to minimize the three-dimensional flow effect near the stagnation point, the radius of the corners was fixed as 1.1 mm of which radius led to the smaller radius-to-height ratio, R/H, than 0.5.[25] Also, both metal blocks 1 and 7 themselves had outlet openings with the same height and depth with the inflow and outflow channels (2 mm H × 2mm D) and they were directly connected to the outflow channels. The length of the opening (OL) was 8 mm. Thus, the polymer flow passed through the channels could be released out of cross-slot flow cell through these two outlet openings. Thus, the total flow length of polymer flow (L) in the cross-slot flow channel (CL = 42.5 mm) and outlet opening (OL = 8 mm) was 50.5 mm. In order to determine the depth-to-height ratio, D/H, X-ray beam absorption by sample along with the maximum diffraction angle was inevitably considered. The chosen D/H ratio was 1 and this ratio was much smaller than 8. The value is known as the minimum cut-off of two-dimensional planar flow which only exhibits extensional component without rotational component.[23] The metal blocks and shims were made of stainless steel to be free of rust. The inner surfaces of shims (channel wall) were machined to reduce the surface roughness. The X-ray windows were beryllium disc with 15 in diameter× 1.5 mm in thickness, T. Also, this cross-slot flow cell was designed to facilitate quartz and

diamond windows for the studies using optical techniques, i.e. birefringence, light scattering, etc. Two Kapton films were placed between the shims and metal blocks to ensure smooth surface and easy cleaning after run. The heating of cross-slot flow cell was achieved by using PID temperature controller connected with four cartridge heaters and thermocouple. Since the PID control was based on the temperature of the cross-slot flow cell, the digital thermometer was again used to measure and calibrate the real temperature of sample in the cross-slot flow cell by directly dipping a thin thermocouple into the melts in the cross-slot flow cell.

The cross-slot flow cell was mounted on the barrel by using connector (9). Thus, the polymer melt in barrel could be driven into the cross-slot flow cell through the connector. The driven polymer melt was split into two streams at the inlet channels of the cross-slot flow cell (Figure 2.3). Finally, the inflow cross streams resulted in the generation of extensional flow along the central outflow plane across the stagnation point.

The strain rate of cross-slot flow cell, $\dot{\varepsilon}$, at volume flow rate, Q, is given by,[26]

$$\dot{\varepsilon} = \frac{Q}{H^2 D} \tag{1}$$

where, Q is the volume flow rate. The maximum attainable volume flow rate, Q for this setup was 368 mm^3 /s and the resultant strain rate ($\dot{\varepsilon}$) was 46 s^{-1}. As the melt was modeled as a fully developed laminar flow of Newtonian fluid with a viscosity (μ) of 1000 pa·s at $\dot{\varepsilon} = 46\, s^{-1}$, the pressure drops, Δp, for the barrel and connector with circular channel (Equation 2), and for the square channel of cross-slot flow cell (Equation 3) could be estimated, respectively, as,[27]

$$\Delta p = \frac{2Q\mu L}{Ar^2} \tag{2}$$

$$\Delta p = \frac{Q\mu L}{AH^2\left[\frac{1}{3} - \frac{64}{\pi^5}\tanh\frac{\pi}{2}\right]} \quad (3)$$

where, r is the radius of cross-section of the barrel or connector. A is the cross-section area of barrel, connector or cross-slot. Thus, based on the partial pressure drops obtained from Equations 2 and 3, the total pressure drop of barrel, connector and cross-slot flow cell, ΔP_{total}, was estimated as ~ 93 bar.

2.2.3. X27C beamline setup

Extensional flow-induced crystallization test using this cross-slot flow device was performed at the Advanced Polymers Beamline (X27C) at the National Synchrotron Light Source (NSLS), Brookhaven National Laboratory (BNL). To adjust the sample-to-detector distance, the base of the device was mounted on a high-precision translational stage of which direction is parallel to the incident X-ray beam. Thus, including the dual movements of feeding apparatus, e.g. horizontal and vertical movements, the device could be adjustable along the three directions, e.g., horizontal, vertical and transverse direction for the alignment. The X-ray beamline (X27C) consisted of a high precision pinhole system that was suitable for simultaneous SAXS and WAXD studies.[17] The X-ray beam (λ = 0.1366 nm) was collimated through the three-pinhole system with 190 cm in length and with the last pinhole size of 0.37 mm in diameter. Using a custom-designed X-ray beam spot monitoring system, the synchrotron beam could be easily aligned with the central stream line of polymer flow. Since we were interested in the dynamic

evolution of anisotropic structure during crystallization, the data collection was carried out by using charge coupled device (CCD, MAR-USA).

2.2.4 Sample and X-ray measurement

An isotactic poly(propylene), *i*PP, made by the Ziegler-Natta method were chosen for the test of this set-up. The molecular weights (number-averaged molecular weight, M_n, peak molecular weight, M_p, weight-averaged molecular weight, M_w, and *z*-averaged molecular weight, M_z) were 78546, 208909, 328034 and 802248 g/mol, respectively. The molecular weight distribution, MWD, was thus about 4.2. The resolution of CCD was1024×1024 pixels (pixel size = 158.44 μm). The collection and storage time of each image were 15 and 5 s, respectively. The sample-to-detector distances for WAXD (112 mm) were calibrated with Al_2O_3 (aluminum oxide) as standard sample. The corrections for background scattering, air scattering and synchrotron beam fluctuation were carried out by using ion chamber before the sample. The cross-slot device was utilized to perform *in-situ* X-ray measurements. First, enough amounts of solid *i*PP pellets were fed into the barrel. Then, the temperature of the sample was elevated to 210 ^oC and maintained the temperature until all *i*PP sample was totally molten. In order to remove air bubbles which were formed in the barrel, the melts were slowly pressed by moving the motor-driven plunger downwards while the bottom of the barrel was left blocked. The plunger was freely released afterwards while maintaining the temperature at 210 ^oC for the compressed polymer melt to recover. After mounting the cross-slot flow cell, the melt was driven into cross-slot flow cell to fill the empty space of channels while maintaining the temperature at 210 ^oC for 5 more minutes to ensure that

the melt was free of any memory effects associated with clusters, crystal aggregates and molecular conformation. Then, the sample was cooled down to 163 ^{o}C at a cooling rate of -3 ^{o}C/min. As the temperature was reached 163 ^{o}C, the sample was subject to an extensional flow and maintained the temperature at 163 ^{o}C up to two hours to collect WAXD images. The flow and temperature protocol for the experiments is shown in Figure 2.5. The test of the device was performed into twofold; strain rate-dependent and strain-dependent tests. For the investigation of strain rate-dependent behavior, the chosen strain rates, $\dot{\varepsilon}$, were 0, 4.6, 11.6, 23.2 and 34.7 s^{-1} at the fixed duration time, t_s = 15s. Also, for the study of the strain dependency in flow-induced crystallization, strain rates, $\dot{\varepsilon}$ = 23.2 s^{-1} was chosen and fixed while varying the duration time, t_s = 0, 5, 10, 15, 17, 20 and 23 s.

2.3 Results and discussions

2.3.1 Strain rate dependency in extensional flow-induced crystallization

Figures 2.6(a), 2.6(b) and 2.6(c) show selected 2D WAXD patterns of *i*PP collected after applying extensional flow; strain rate, $\dot{\varepsilon}$ =11.6, 23.2 and 34.7 s^{-1} for 15 s, at 163 ^{o}C. We note that all the experiment of this study were performed at 163 ^{o}C while varying the strain rate, $\dot{\varepsilon}$ or strain, ε. We also note that 2D WAXD patterns obtained from quiescent melt at 163 ^{o}C only exhibited amorphous halo during the experimental time duration (~ 2 hours) representing that the sample was in a totally molten state without any ordered structure formation associated with orientation and crystallization. As the extensional flows were applied, however, the patterns began to reveal highly

oriented crystalline reflections and the reflections intensified as crystallization time increased. It is noted that the deformed melts begin to show the typical of oriented equatorial and off-axis reflections of α-crystal, i.e. (110), (040), (130), (111) and (131) reflections.[28] These oriented reflection patterns at around the equator and off-axis, e.g. equatorial (hk0) and off-axis (hkl) reflections, clearly indicated that the two opposing inflow streams driven by the plunger created an extensional flow field along the central stream line of the outflow channels and they finally induced the stretching of chains along the flow direction. Since no crystallization indication was detected at the quiescent melt, it is evidenced that the observed crystalline reflections are intimately associated with the chain stretching at the flow conditions which accompany the flow-induced precursor structure formation. As mentioned previously, the pre-existing state of chain stretching induced by flow and the subsequent formation flow-induced precursor structure is closely related to the coil-stretch transition of polymer chains. Based on the twofold criticality of Keller, it can be thought that the molecular weight of the stretched chains were higher than the critical orientation molecular weight, M at the flow condition. In other words, the applied strain rates, $\dot{\varepsilon}$=11.6, 23.2 and 34.7 s^{-1} were at the ranges of at $\dot{\varepsilon} \geq \dot{\varepsilon}_c$ for the stretched chains. We note that the flow-induced precursor structure formation was absent at a relatively low strain rate, $\dot{\varepsilon}$ = 4.6 s^{-1}. This implied that the applied strain field was not enough to induce the chain stretching and the formation of flow-induced precursor structure. Or the concentration of any ordered structure was so dilute that it could not be detected by WAXD.

In order to investigate the flow-induced crystallization precursor structure depending on the magnitude of strain rate, the crystallinity changes were obtained from the 2D WAXD patterns as partly shown in Figure 2.6. To obtain the crystallinity, the 2D

WAXD patterns were first Fraser-corrected[29] and circularly averaged. Then, the resultant circular-averaged WAXD profiles were curve-fitted by using 7 Voight functions; 2 functions for amorphous halo and 5 functions for crystalline reflections, as exemplified in Figure 2.7. The 2θ range selected for the curve-fitting was 6~26 °. The total crystallinity (weight-averaged crystallinity or crystallinity index), *Xc*, is given as,

$$Xc = \frac{Ac}{Aa + Ac} \times 100 \tag{4}$$

where, *Ac* and *Aa* are the total reflection area of crystalline peaks and amorphous halo, respectively. The total crystallinity changes obtained from the above curve-fitting procedure were depicted in Figure 2.8. It is seen that the total crystallinity increases as strain rate increases. This indicates that more chains were involved in flow-induced crystallization as the magnitude of strain rate increases. Since no crystallization was evolved in the quiescent melt, the oriented crystalline structure evolution after the cessation of extensional flow can indicate the formation of flow-induced crystallization precursor structure which will finally dominate the final crystallinity; the concentration of flow-induced precursor structure will be proportional to the total final crystallinity. Based on the final crystallinities obtained at t = ~2500 s after the application of flow, the dependence of strain rate on crystallinity was depicted in Figure 2.9. It is noted that the crystallinity change begins to show steep increase at $4.6 < \dot{\varepsilon} \leq 11.6$ s^{-1} (see dotted vertical line in the diagram). This corresponds to Keller's assumption of coil–stretch transition in polydispersed polymer melt.[1] At a given strain rate, only the chains longer than *M* will be stretched while the rest of shorter chains remains in random-coiled state without experiencing the transition, where increasing strain rate increases the amount chains that can be stretched while down-shifting the critical orientation molecular weight,

M in the molecular weight distribution. The increased amount of stretched chain segments will obviously increase the total crystallinity. It is also true that the applied strain rate, $\dot{\varepsilon}$ was higher than the critical strain rate, $\dot{\varepsilon}_c$ for chains with $M_w \geq M$.

2.3.2 Strain dependency in extensional flow-induced crystallization

Selected 2D WAXD patterns of *i*PP sample collected after applying the different strains (different flow duration time), ε =394.4, 463 and 534 but the fixed strain rate, $\dot{\varepsilon}$ = 23.2 s^{-1} are seen in Figures 2.10(a), 2.10(b) and 2.10(c), respectively. The previously presented WAXD patterns in Figure 2.6 (b) were subject to ε = 348 at $\dot{\varepsilon}$ = 23.2 s^{-1} and so it can be compared with the WAXD patterns in Figures 2.10(a)-2.10(c). The total strain of melt along the central outflow stream line can be estimated by integrating the strain rate over time as,[23]

$$\varepsilon = \int_{t_i}^{t_f} \dot{\varepsilon} \cdot t \cdot dt \tag{5}$$

where, t_i and t_f are the initial and final time for the application of strain field. We note that the quiescent melt and the melt sunject to a relatively low strain, ε = 232 at $\dot{\varepsilon}$ = 23.2 s^{-1} only represented amorphous halo implying that the melts were in totally molten states without any ordered strauture formation. As can be seen in Figures 2.10(a), 2.10(b) and 2.10(c), however, the melts obviously began to reveal highly oriented reflection patterns of α-crystals and the reflections were intensified as the strain increased as the melts were subject to the higher strains. This represented that the applied strain field apparently induced the formation of flow-induced precursor structure of which chain axis is parallel

to the direction of extensional flow and will finally facilitate the folded-chain crystal (kebab) growth on top of it.

To investigate the evolution of oriented crystal depending on the applied strain at the fixed strain rate in greater detail, the changes of total crystallinity was obtained partly from the 2D WAXD patterns presented in Figures 2.6(b) and 2.10(a)-2.10(c), and the results were shown in Figure 2.11(a). Also, the dependency of the total crystallinity on the applied strain was depicted in Figure 2.11(b), based on the final crystallinities obtained at t = ~2500 s. The total crystallinityies were obtained from the same procedure as mentioned above in Figure 2.7, Equation (4) and the related text. In Figures 2.11(a) and 2.11(b), it is noted that the total crystallinity increases as the strain increases at the strain rate and the increase is finally saturated. We recall that the applied strain rate, $\dot{\varepsilon}$ = 23.2 s^{-1} was in the range of $\dot{\varepsilon} \geq \dot{\varepsilon}_c$ as seen from Figure 2.9, where it was seen that the flow condition induced the flow-induced precursor structure formation and the formation was highly strain rate-dependent. Thus, it would lead to the oriented precursor structure formation at $\varepsilon <\sim 300$, even though the magnitude of strain was relatively low. However, it is noted that no crystallization is observed when $\varepsilon <\sim 300$ as can be seen in Figure 2.11(b). Based on this result, it can be thought that the precursor structure formation is also highly strain-dependent even at $\dot{\varepsilon} \geq \dot{\varepsilon}_c$. An induction time seems to be needed so that random coiled-chains discoils and they have an enough orientation to form precursor structure in the presence of flow.

One of the most interesting features that can be seen in Figure 2.11(b) is that the change exhibits sigmoidal curve, where the formation of flow-induced precursor structure is achieved only when the strain reaches a certain critical point. Also, it is noted that the transition is very sharp at a very narrow strain region (note the shaded rectangle in the

diagram). This indicates that, at a fixed strain rate higher than critical strain rate, there exists a critical strain, ε_c for the chains to form flow-induced precursor structure. In monodisperse polymer melts, it is considered that the critical strain, ε_c is highly molecular weight-dependent. Increasing molecular weight decreases critical strain as schematized in Figure 2.12. Also, the transition is thought to be very sharp. In this case, the local fluctuation of entanglement density and thus the orientation fluctuation may result in the finite transition width of critical strain, ε_c. In polydispersed melt, on the other hand, since the chain species with $M_w \geq M$ in the region of high molecular weight tail of the molecular weight distribution experience coil-stretch transition at a given strain rate, the molecular weight of chains which experience the coil-stretch transition is also polydisperse. Thus, the width of critical strain, ε_c is considered to be much broader as compared to the monodisperse polymer melts. Also, increasing strain rate in the range of $\dot{\varepsilon} \geq \dot{\varepsilon}_c$, will increase the transition with in $\dot{\varepsilon}_c$ due to the broadened molecular weight distribution of chains that can be stretched and form oriented precursor structure. It is also reasonable to consider that the increases in Figure 2.12 will continue and be saturated if all the probable chains with $M_w \geq M$ at the strain rate, $\dot{\varepsilon}$ form flow-induced precursor structure.

After the cessation of flow, as in our study, the stretched chains in molten matrix are assumed to be highly dynamic, where some chains will form oriented precursor structure while others will relax back into random-coiled state. Indeed, the formation of oriented precursor structure or relaxation is assumed to be dominated by the two competing counter parts, e.g. the forces generated by Van der Waals interactions, i.e. interactions by stretched chains and/or interactions at entanglement points, and the entropy of stretched chains segments. In our previous study, it was evidently shown that

even the preformed precursor structure (shish) relaxed drastically accompanying the decreases in the length and the total crystallinity immediately after shear cessation.[30] This evidenced that the formation of flow-induced precursor structure after the cessation of flow is dominated by the two competing counter parts, Van der Waals interactions and entropic force. If the chain interactions are dominant by creating an effective frictional grip to prevent entropic recovery, the stretched chain segments will form flow-induced precursor structure, otherwise they will relax. It is thought that the concentration of stretched chain segments, its orientation and entanglement density between stretched chains are the determining in the magnitude of frictional grip between stretched chain segments. It is also reasonable to consider that the fluctuations in the concentration, orientation and entanglement density will perturb the transition width to become broader.

2.4 Cnoclusions

The unique cross-slot flow device, for the purpose of the investigation of extensional flow-induced crystallization of semicrystalline polymers using synchrotron WAXD and SAXS, have devised and tested. The WAXD results clearly demonstrated that the device generated extensional flow at the outflow channel across the stagnation point. It was found that the formation of oriented precursor structure formation is strongly governed by the applied strain rate and strain. As strain rates and strain increased at $\dot{\varepsilon} \geq \dot{\varepsilon}_c$ flow-induced crystallization precursor structure formation was facilitated more and more and the total final crystallitnity increased. Most of all, it was found that there existed a critical strain, ε_c for the formation of oriented precursor structure even at $\dot{\varepsilon} \geq \dot{\varepsilon}_c$. At ε_c, there existed a sharp transition from amorphous to crystalline state. This

indicated that, even though at $\dot{\varepsilon} \geq \dot{\varepsilon}_c$, the stretched chain segments must possess enough degree of orientation to form flow-induced precursor structure. After Keller proposed the two-fold criticalities in coil-stretch transition in entangled polymer melt, a great deal of studies have been performed to clarify the origin of flow-induced crystallization precursor structure and the results were well documented else where.[1,8,9] However, the existence of critical strain, ε_c for the formation of flow-induced crystallization precursor structure has not been addressed by others. Thus, we proposed the existence of critical strain, ε_c for the formation of oriented crystallization precursor structure at the strain rate higher than critical strain rate, $\dot{\varepsilon} \geq \dot{\varepsilon}_c$. It was also argued that the formation of oriented precursor structure is dominated by the two competing counter forces, Van der Waals interactions and entropic force, where if the chain interactions are dominant the stretched chains would form oriented precursor structure, otherwise they would relax.

2.5 References

1. Kolnaar, J. W. H.; Keller, A. *Prog. Col. Polym. Sci.* **1993**; 92; 81.
2. Keller, A.; Machin, M. J. *J. Macromol. Sci., Phys*. **1967**; B1(1); 41.
3. Hill, M. J.; Keller, A. *J. Macromol. Sci., Phys.* **1971**; B5(3); 591.
4. Keller, A.; Muller, A. J.; Odell, J. A. *Prog. Colloid Polym. Sci.* **1985**; 75; 175.
5. Keller, A.; Odell J. A. *Colloid. Polym. Sci.* **1985**; 263; 181.
6. Pennings, J.; van der Mark, J. M. A. A.; Kiel, A. M. Kolloid Z. Z. Polym. **1970**; 237; 336.
7. Loos, J.; Katzenberg, F.; Petermann, J. *J. Mat. Sci.* **1997**; 32; 1551.
8. Somani, R. H.; Yang, L; Zhu, L; Hsiao, B. S. *Polymer* **2005**; 46; 8587.

9. Kumaraswamy, G. J. *Macromol. Sci. Polym. Rev.* **2005**; 45; 375.

10. Hsiao, B. S.; Yang, L.; Somani, R. H.; Avila-Orta, C. A.; Zhu, L. *Phys. Rev. Lett.* **2005**; 94; 117802.

11. Somani, R. H.; Hsiao, B. S.; Nogales, A.; Srinivas, S.; Tsou, A. H.; Sics, I.; Balta-Calleja, F. J.; Ezquerra, T. A. *Macromolecules* **2000**; 33; 9385.

12. Zuo, F.; Keum, J. K.; Yang, L.; Somani, R. H.; Hsiao, B. S. *Macromolecules*, **2006**; 39; 2209.

13. Dukovski, I.; Muthukumar, M. J Chem Phys **2003**; 118; 6648.

14. Kumaraswamy. G.; Kornfield, J. A.; Yeh, F.; Hsiao, B. S. *Macromolecules* **2002**; 35 ;1762.

15. de Gennes, P. G. *J. Chem. Phys.*, **1974**; 60; 5030.

16. Smith, D. E. ; Babcock, H. P.; Chu, S. *Science* **1999**; 283; 1724.

17. Chu, B; Hsiao, B. S. *Chem. Rev.* **2001**; 101; 1727.

18. Yang, L.; Somani, R. H.; Sics, I.; Hsiao, B. S.; Kolb, R.; Fruitwala, H; Ong, C. *Macromolecules* **2004**, 37, 4845.

19. Keum, J. K.; Burger, C.; Hsiao, B. S.; Somani, R. H.; Yang, L.; Chu, B.; Kolb, R.; Chen, H.; Lue, C. -T. *Prog. Colloid Polym. Sci.* **2005**; 130; 114.

20. Toki, S.; Sics, I.; Hsiao, B. S.; Tosaka, M.; Poompradub, S.; Ikeda, Y.; Kohjiya, S. *Macromolecules* **2005**; 38, 7064.

21. Samon, J. M.; Schultz, J. M.; Hsiao, B. S.; Seifert, S.; Stribeck, N.; Gurke, I.; Saw, C.; Collins, G. *Macromolecules* **1999**; 32; 8121.

22. Miles, M. J.; Keller, A. *Polymer* **1980**; 21; 1295.

23. Swartjes, F. H. M., Ph. D. Thesis. **2001**, Eindhoven University of Technology.

24. Meerveld, J; Peters, Gerrit W. M.; Huetter, M. *Rheol. Acta*. **2004**; 44; 119.

25. Swartjes, F. H. M., Master's thesis 1996, Eindhoven University of Technology.

26. Odell, J. A.; Carrington, S. P. *J. Non-newtonian Fluid Mech.* **2006**; 137; 110.

27. Bahrami, M.; Yovanovich, M. M.; Culham, J. R. *J. Fluid Eng.* **2006**; 128; 1036.

28. Somani, R. H.; Yang, L.; Hsiao, B. S.; Agarwal, P.; Fruitwala, H.; Tsou, A. H. *Macromolecules* **2002** ; 35 ; 9096.

29. Fraser, R. D. B.; Macrae, T. P. ; Miller, A.; Rowlands, R. J. *J. Appl. Cryst.* **1976**; 9; 81.

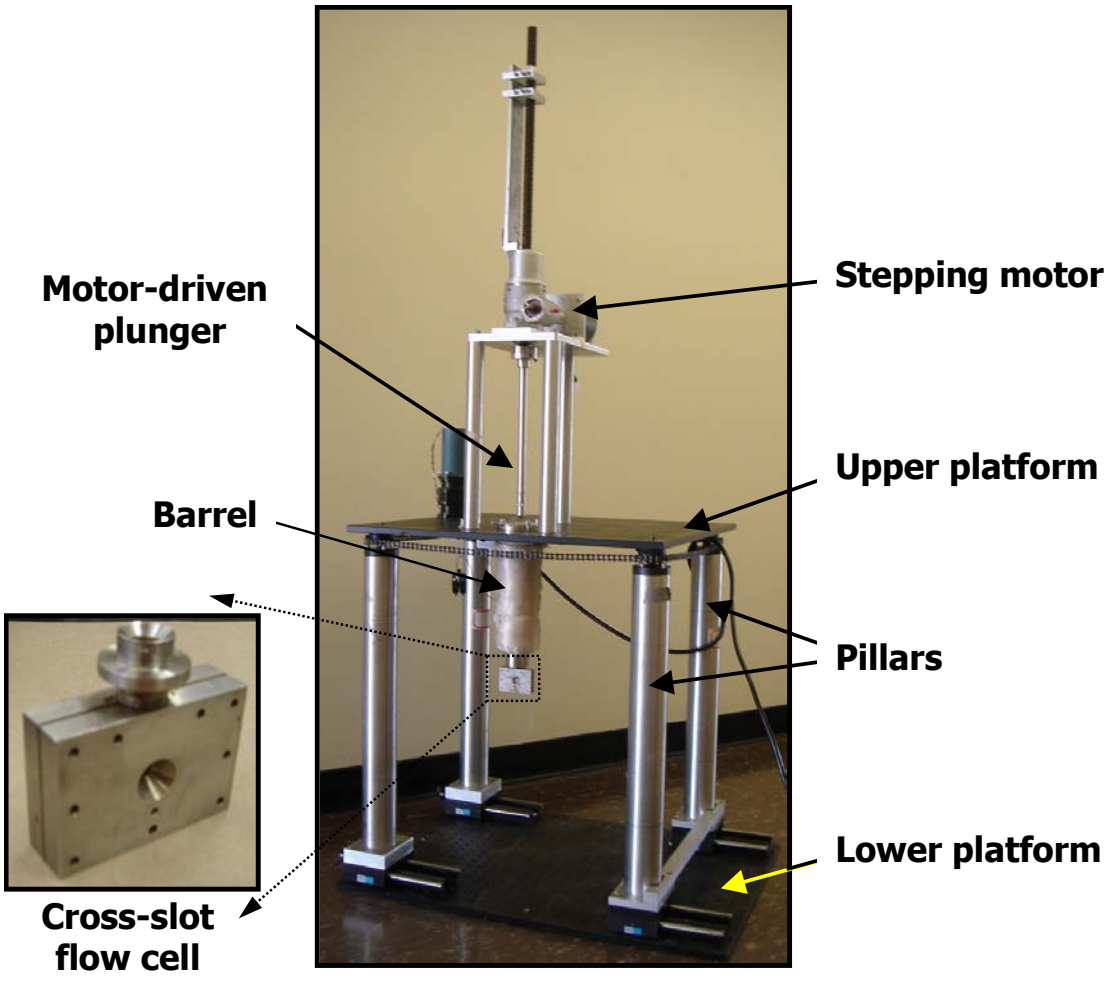
Motor-driven plunger
Stepping motor
Upper platform
Barrel
Pillars
Lower platform
Cross-slot flow cell

Figure 2.1

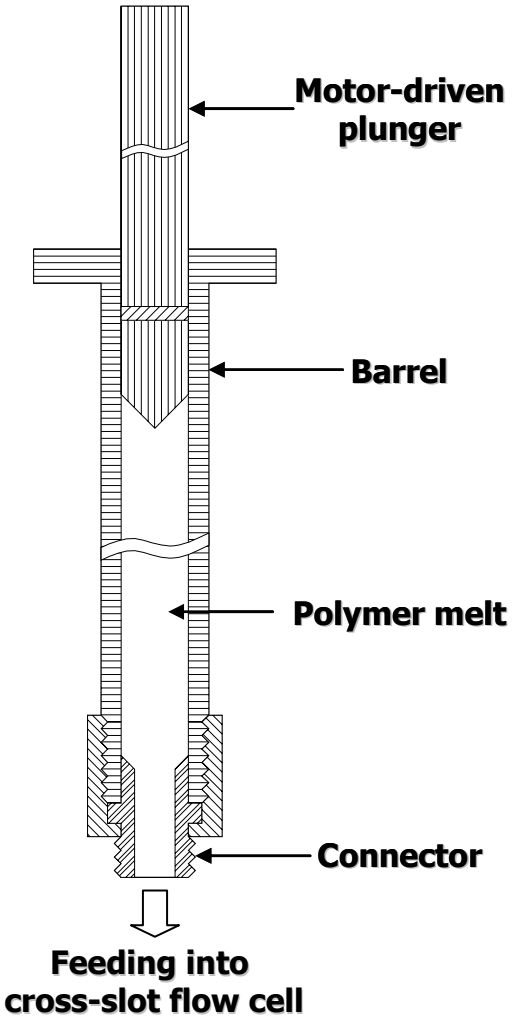
Motor-driven plunger
Barrel
Polymer melt
Connector
Feeding into cross-slot flow cell

Figure 2.2

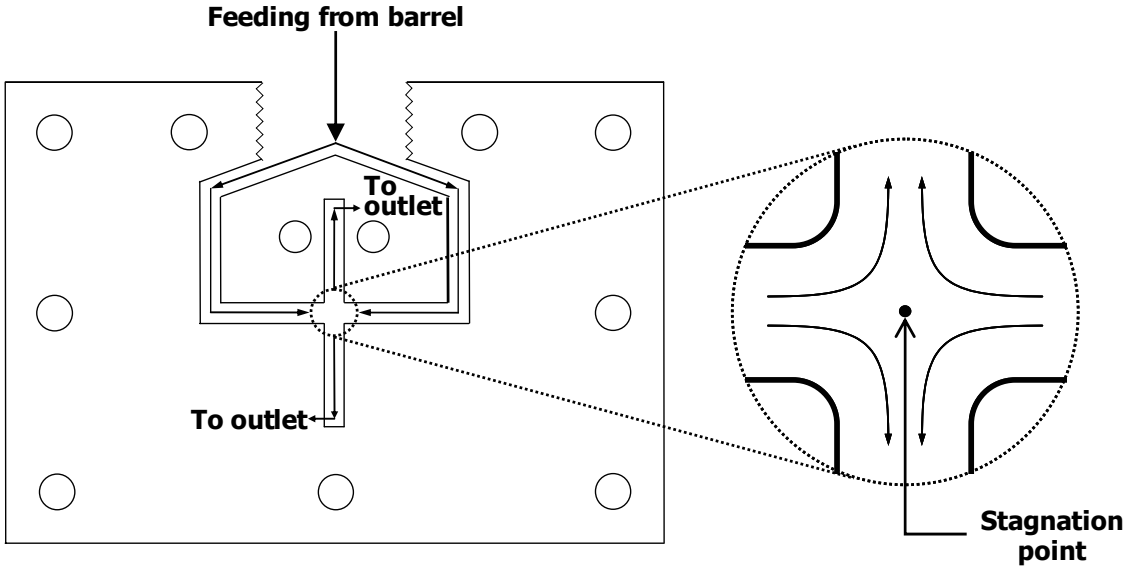

Figure 2.3

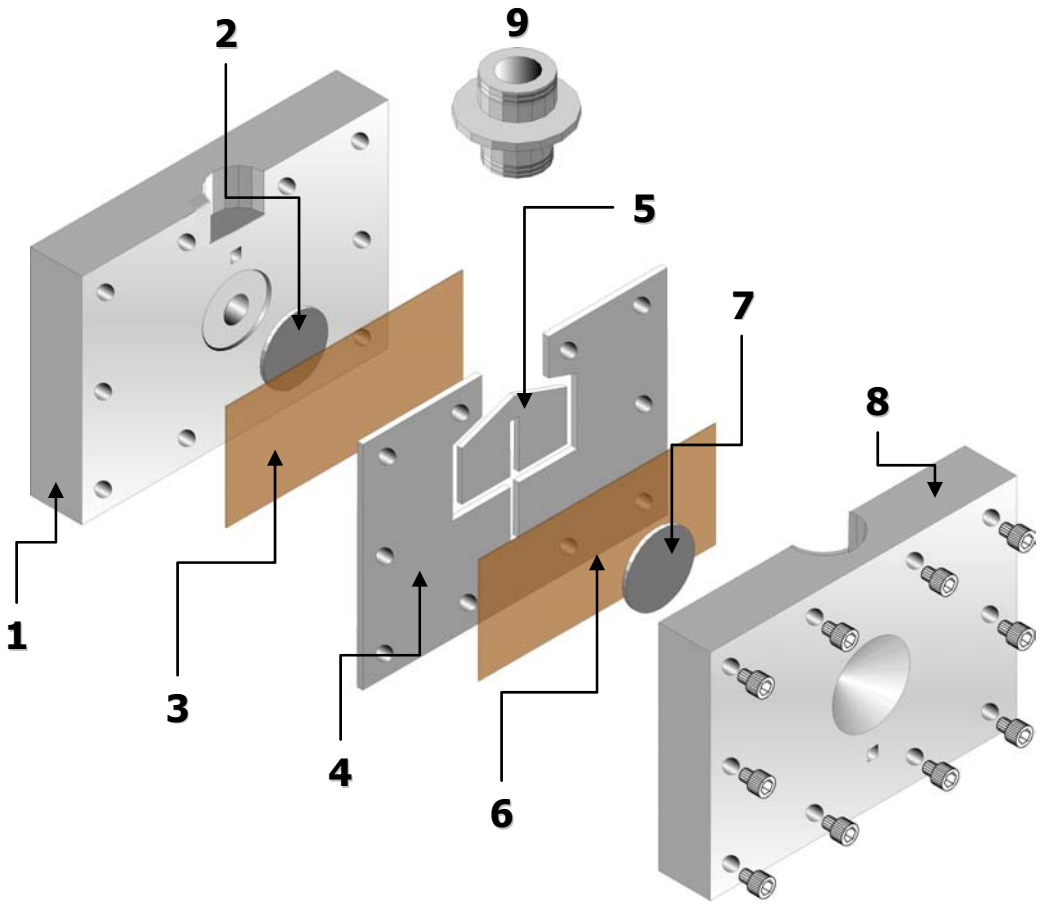

Figure 2.4(a)

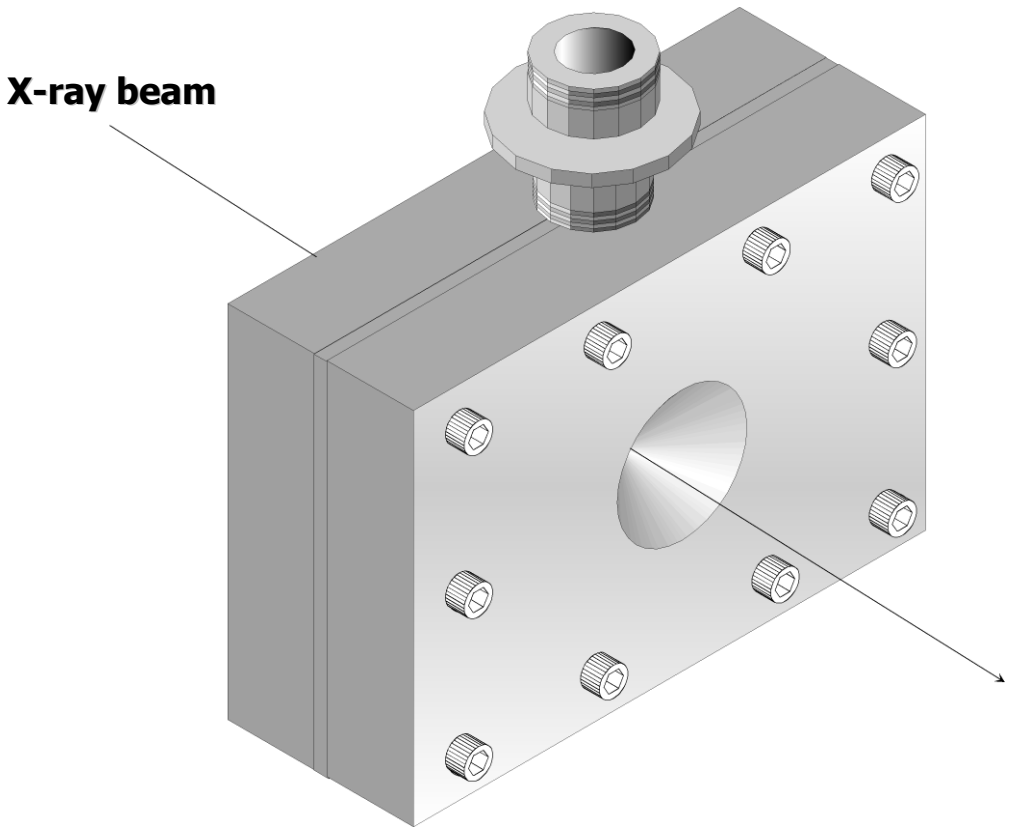

Figure 2.4(b)

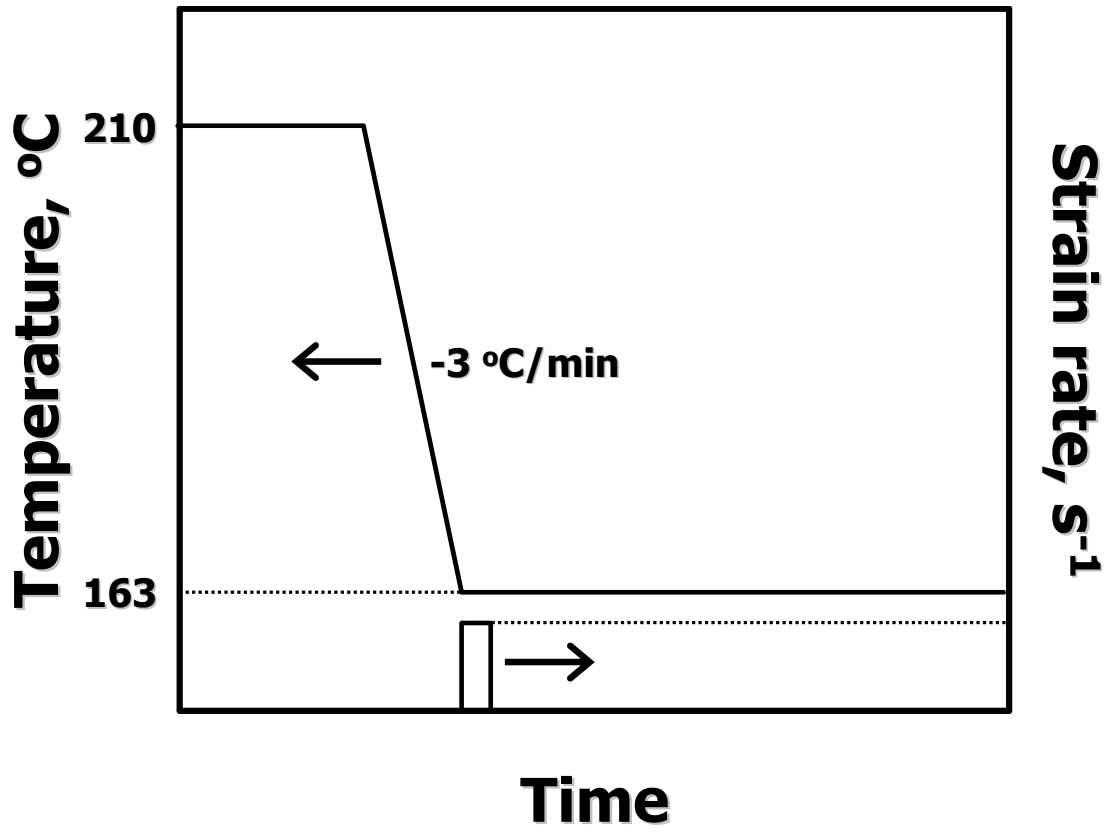

Figure 2.5

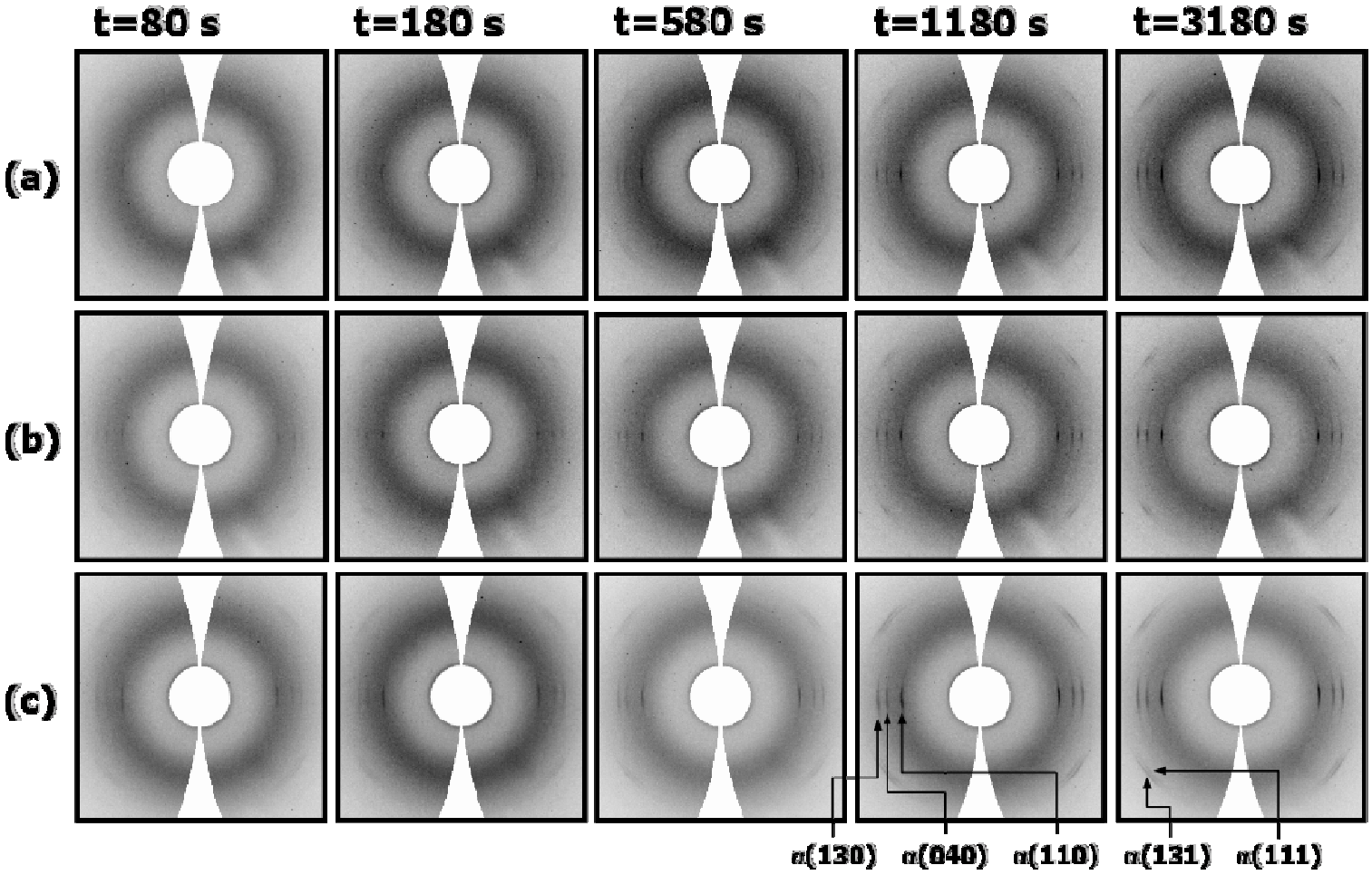

Figure 2.6(a), 2.6(b) and 2.6(c)

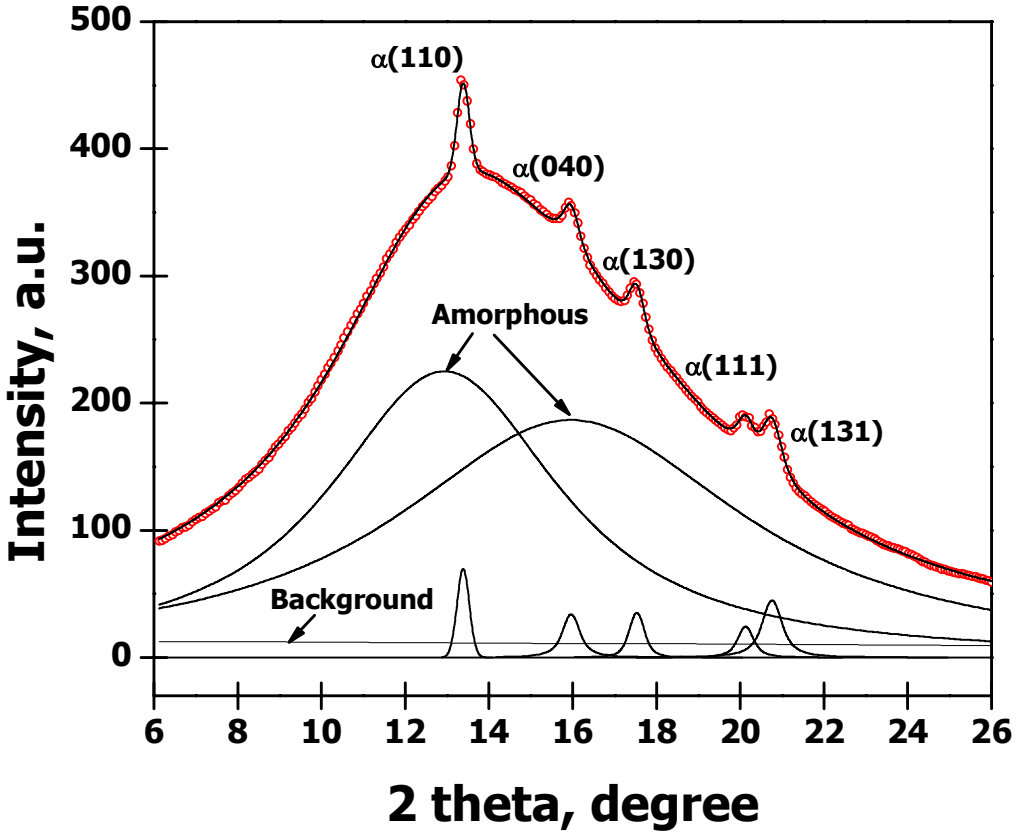
500
400
300
200
100
0
Intensity, a.u.
α(110)
α(040)
α(130)
α(111)
α(131)
Amorphous
Background
6
8
10
12
14
16
18
20
22
24
26
2 theta, degree

Figure 2.7

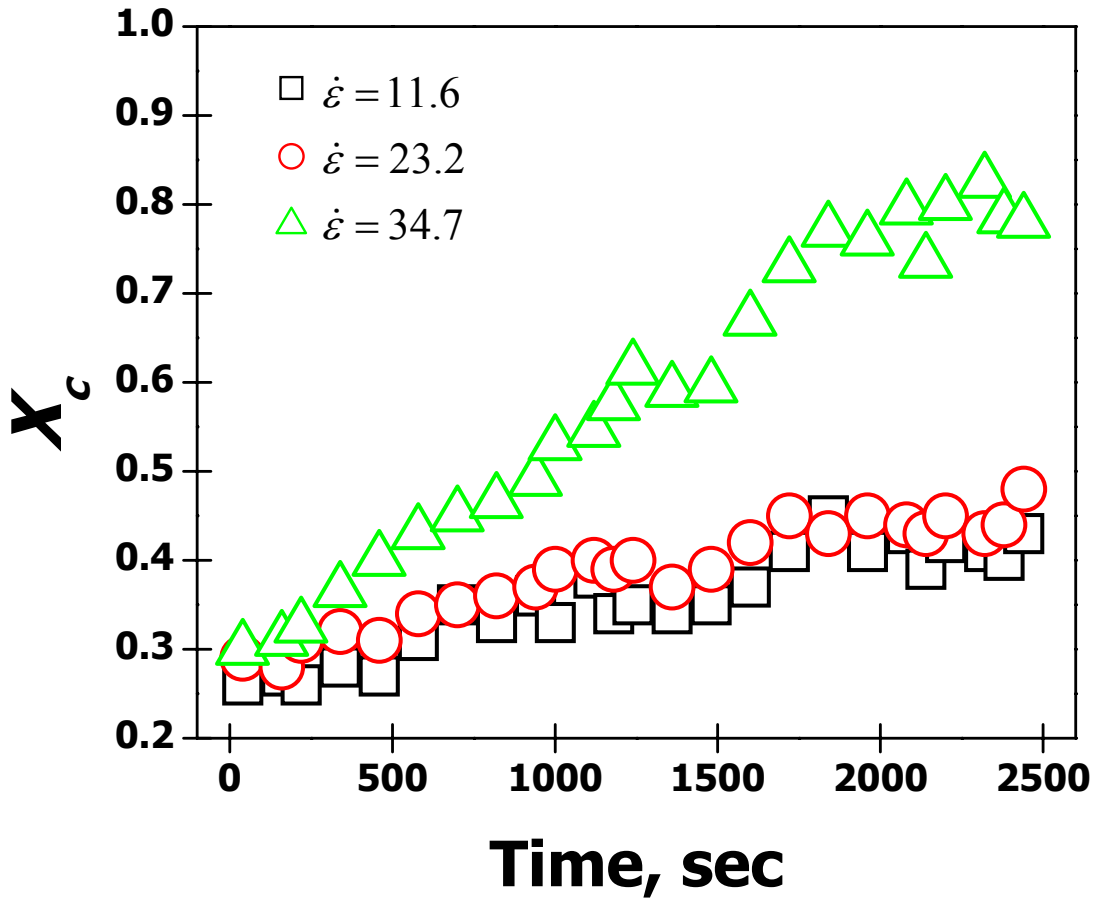
1.0
0.9
0.8
0.7
0.6
0.5
0.4
0.3
0.2
X_c
$\dot{\varepsilon} = 11.6$
$\dot{\varepsilon} = 23.2$
$\dot{\varepsilon} = 34.7$
0
500
1000
1500
2000
2500
Time, sec

Figure 2.8

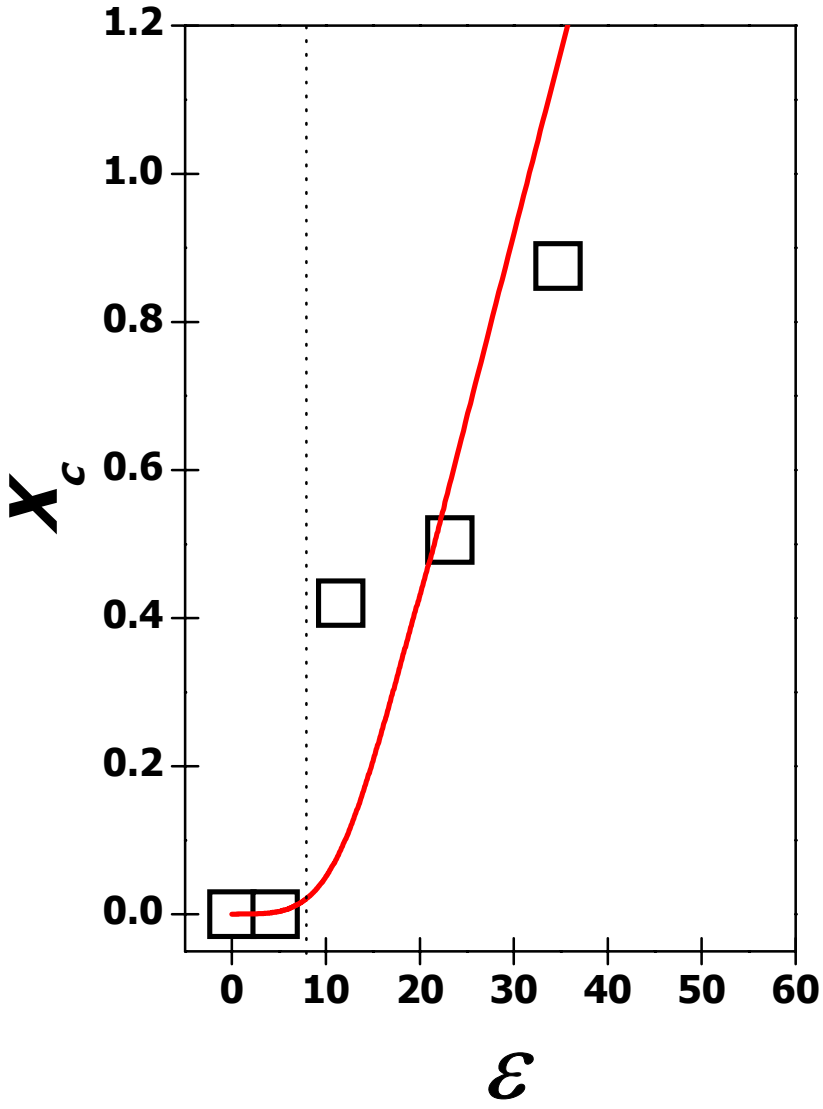

Figure 2.9

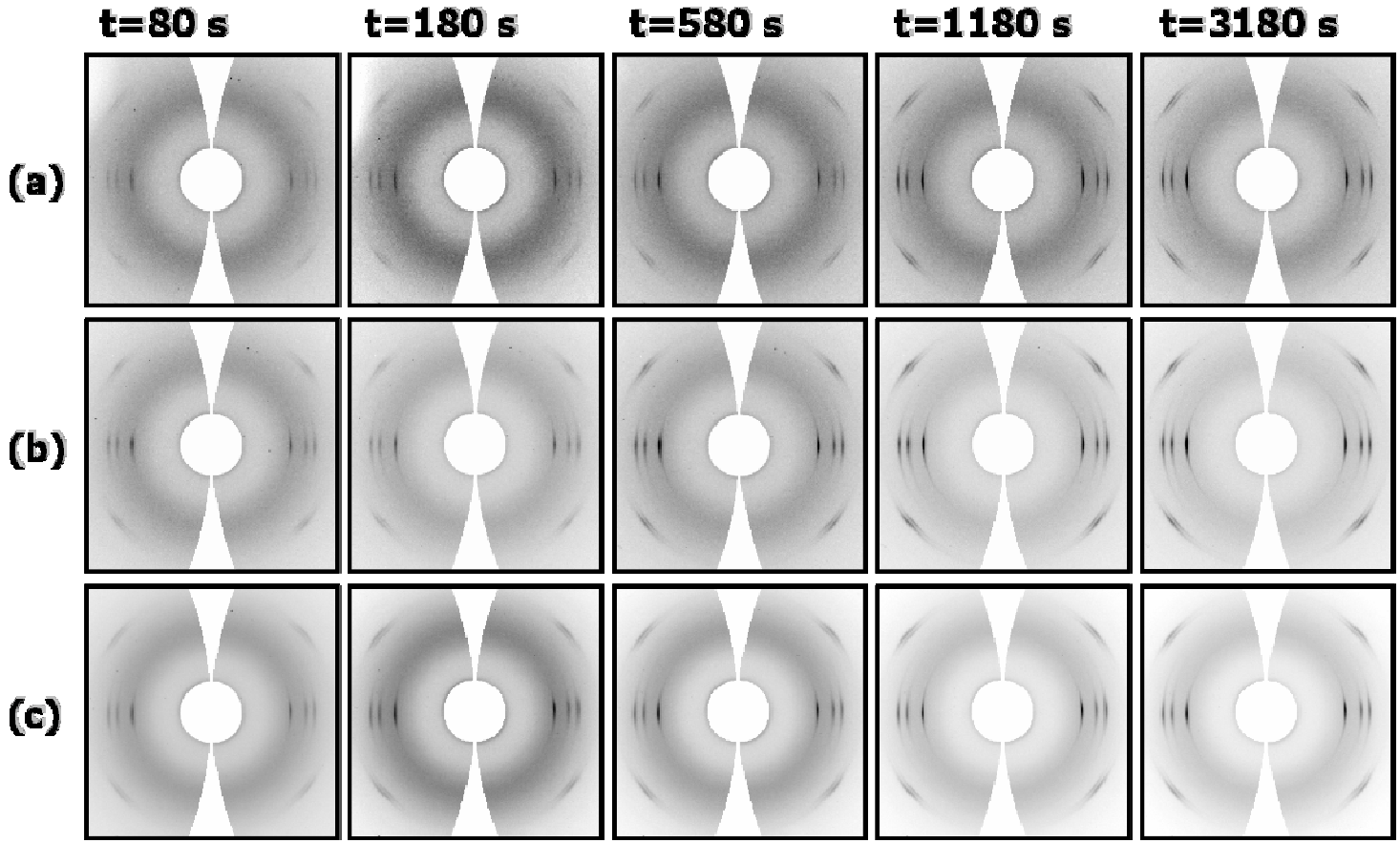

Figure 2.10(a), 2.10(b) and 2.10(c)

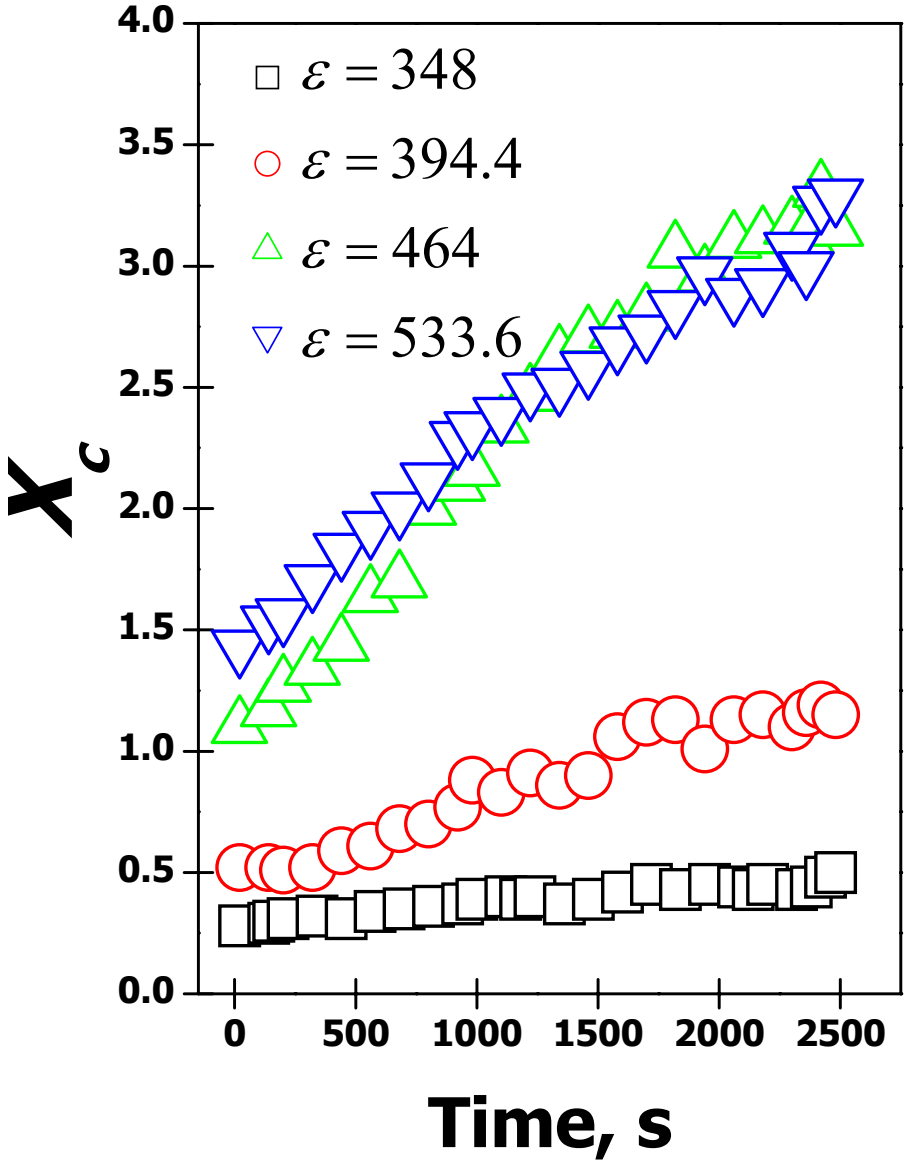
□ ε = 348
○ ε = 394.4
△ ε = 464
▽ ε = 533.6
X c
4.0
3.5
3.0
2.5
2.0
1.5
1.0
0.5
0.0
0
500
1000
1500
2000
2500
Time, s

Figure 2.11(a)

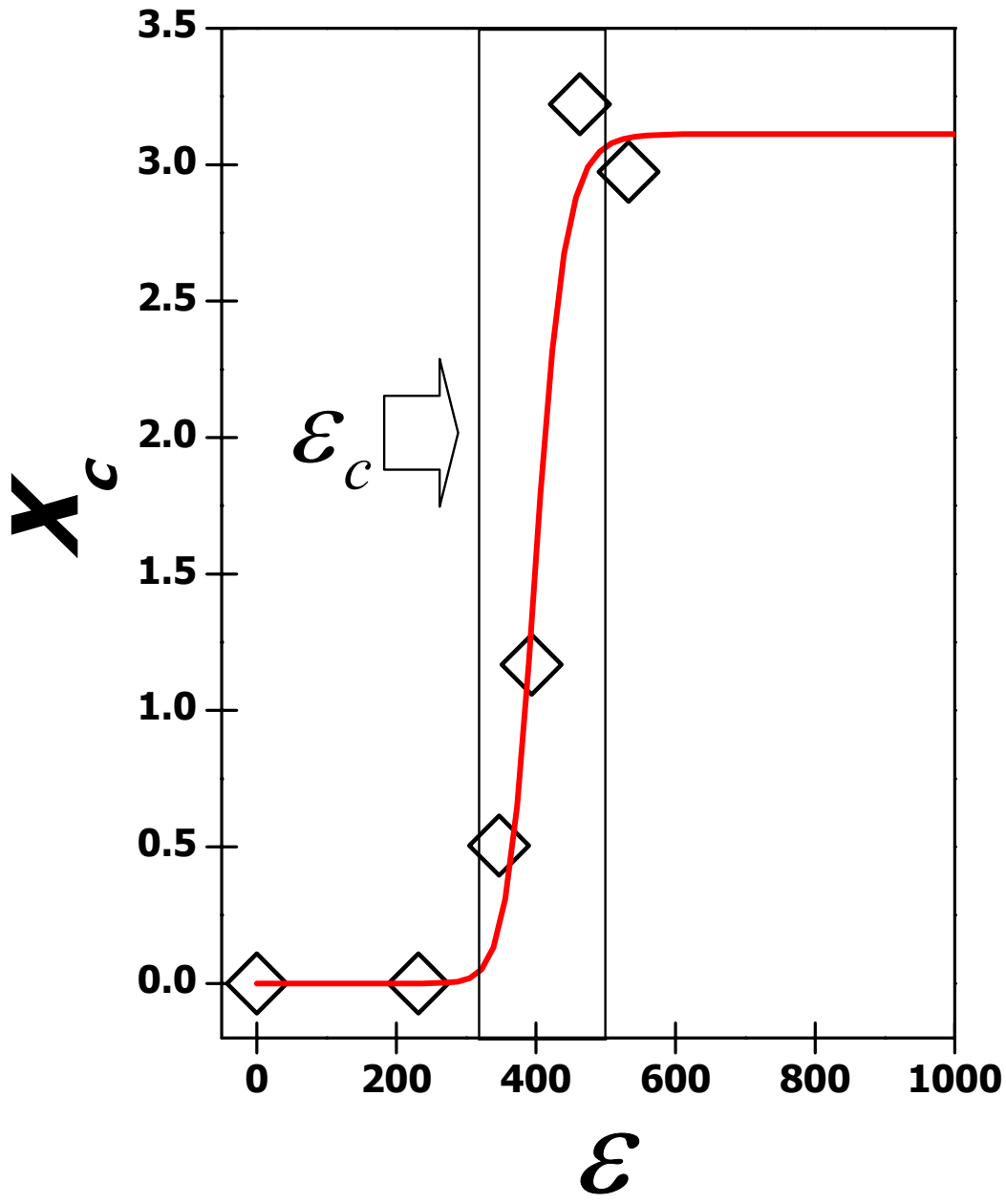
3.5
3.0
2.5
2.0
1.5
1.0
0.5
0.0
χ_c
ε_c
0
200
400
600
800
1000
ε

Figure 2.11(b)

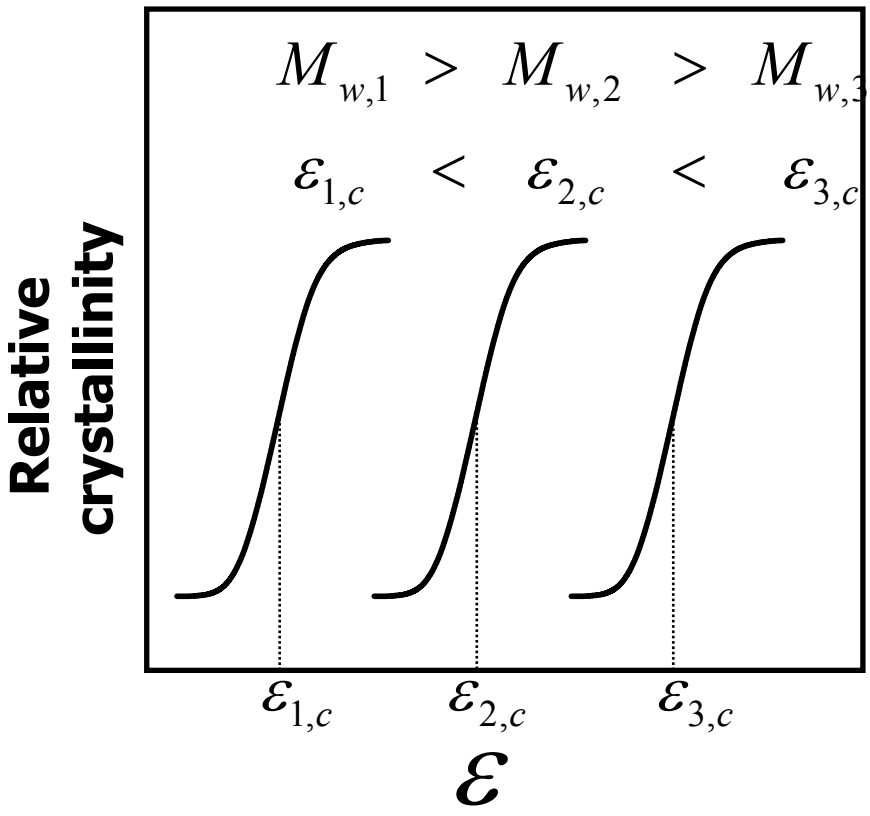
$M_{w,1} > M_{w,2} > M_{w,3}$
$\varepsilon_{1,c} < \varepsilon_{2,c} < \varepsilon_{3,c}$
Relative crystallinity
$\varepsilon_{1,c}$
$\varepsilon_{2,c}$
$\varepsilon_{3,c}$
ε

Figure 2.12

Chapter 3. Probing Flow-Induced Precursor Structures in Blown Polyethylene Films by Synchrotron X-rays during Constrained Melting

3.1 Introduction

Mechanical properties of polymeric materials are dependent on the molecular orientation as well as the overall morphology, which are directly affected by different processing conditions, such as fiber spinning, injection molding, extrusion and film blowing.[1-3] Recent results indicated that external flow field always generates a scaffold of precursor structures (i.e., shish kebabs) at the initial stage of crystallization due to the rheological differences of individual chains.[4,5] This scaffold, which is thermally stable, usually dictates the subsequent morphological development. In this study, we are mainly interested in understanding the nature of the earliest events of polymer crystallization during polymer film blowing process, where a sequential biaxial extensional flow is involved. As *in-situ* experiments are quite difficult to conduct during the film blowing process, a melting study of restrained films (we termed this *restrained melting*) was carried out to extract the information about the flow-induced precursor structures generated at the initial stage of crystallization at high temperatures. This approach appears to work well because the melting temperature of the precursor scaffold is notably higher than the melting temperature of the later formed crystallites.[6]

Keller et al reported that crystalline lamellae (or kebabs) grow epitaxially from the crystallographic *c*-axis of extended chain row-nuclei (or shish) during film blowing.[7] The growth of lamellae often twists gradually around its *b*-axis but stays perpendicularly

to the machine direction (MD) or its *a*- and *c*-axes. The MD orientation of the *a*- and *c*-axes depends on the type of PE and the processing conditions involved. In typical film blowing process, most polymer chains are first oriented along the MD, where the corresponding lamellae would grow along the transverse direction (TD). However, the process involves deformation in two orthogonal directions and normally results in a biaxial molecular orientation along MD and TD.[8,9]

In applications of polymer blown films, such as packaging, polyethylene (PE) is the most widely used system.[10,11] To meet the requirements of good film clarity and high mechanical strength, blends of PE with different molecular weights, distributions and chain architecture have been routinely used as a viable means to tailor the structure and properties. In the last two decades, a great deal of efforts has been made to create new polymer blend systems for commercial applications. However, it is fair to state that the progress made by such an approach has often been hampered by the behavior of phase separation in polymer blends and the lack of understanding of flow-induced crystallization in polymer blends.[12,13] Recently, some studies indicate that the incorporation of a small amount of long chain species can effectively control the behavior of flow-induced crystallization in the matrix and thus the final mechanical properties of the blown films.[14] These results are consistent with the recent findings from *in-situ* rheo-X-ray[4,5,15] and rheo-optical[16,17] studies, which clearly illustrated the critical role of long chains on the production of a precursor scaffold at the early stages of crystallization under flow.

In chapter 3, we have chosen two PE blown films, processed at the same conditions, for *in-situ* small-angle X-ray scattering (SAXS) and wide-angle X-ray diffraction (WAXD) studies. The PE films were restrained during melting in order to

preserve the initial precursor structures formed at high temperatures. The chosen blown films included linear low density polyethylene (LLDPE) and a blend of high density polyethylene (HDPE) with LLDPE. The HDPE sample contained a bimodal distribution of molecular weights: high molecular weight (HMW) and low molecular weight (LMW) components. The HDPE/LLDPE blend composition was selected in such a way that the concentration of the HMW-HDPE species was just above its overlap concentration. The overlap concentration represents the concentration of a polymer in a solution, where the average chains begin to interpenetrate each other and become entangled. Results between LLDPE and HDPE/LLDPE blends were compared to elucidate the role of HMW species on the formation the crystallization precursor structures during the blowing process.

3.2 Experimental

3.2.1 Materials

Both PE blown films (LLDPE and HDPE/LLDPE blend with 5 wt% of HDPE) were experimental materials, processed under the same blowing conditions (extruder diameter: 60 mm, extrusion throughput: 1.8 kg/hr/cm, die diameter: 150 mm, extrusion temperature: 210 ^{o}C, die gap: 1.5 mm, air temperature: 11 ^{o}C, frost line height: 64 cm, film gauge: 25 m). The GPC profiles of HDPE and LLDPE before blending are illustrated in Figure 3.1; the corresponding molecular weight information is summarized in Table 3.1. The LLDPE sample was synthesized by the metallocene method and contained 2.4 mole % of hexene as the comonomer unit, i.e., 12 hexene-branches per

1000 carbon atoms. The weight average molecular weight ($\overline{M}_w$) of LLDPE was 116,000 g/mol and the molecular weight distribution ($\overline{M}_w/\overline{M}_n$) was 2.4. The HDPE sample ($\overline{M}_w$ = 130,000 g/mol) was a homopolymer made by the Ziegler-Natta method and possessed a bimodal molecular weight distribution: LMW-HDPE (80 wt%) and HMW-HDPE (20 wt%). The $\overline{M}_w$ values of the two distributions in HDPE were 99,000 g/mol (LMW-HDPE) and 1,100,000 g/mol (HMW-HDPE), respectively. The two HDPE distributions were estimated by deconvoluting the GPC profile with two Gaussian functions, as shown in Figure 3.1. For the HDPE/LLDPE blend, 5 wt% of HDPE was melt-mixed with LLDPE using an extruder. Thus, in the blend, the concentration of HMW-HDPE chain distribution ($\overline{M}_w$ = 1,100 g/mol) was about 1.0 wt% and this value was higher than the calculated overlap concentration. The corresponding overlap concentration, c^*, of the HMW-HDPE species was calculated by the following expression.[18]

$$c^* = \frac{3\overline{M}_w}{4\pi\left[\left\langle R_g^2\right\rangle^{1/2}\right]^3 N_a} \quad (1)$$

where $\left\langle R_g^2\right\rangle^{1/2}$ represents the root-mean-square radius of gyration and N_a is the Avogadro's number. As the characteristic ratio of $\left\langle R_g^2\right\rangle^{1/2}/\overline{M}_w{}^{1/2}$ for molten HMW-HDPE was 0.46 based on SANS measurements [19], the estimated overlap concentration, c^*, was approximately 4.0×10^{-3} g/cm^3 (i.e., 0.5 wt% in the blend melt). We are particularly interested in the role of HMW-HDPE on the formation of flow-induced crystallization precursor scaffold and subsequent crystallization during the film blowing process because of its long relaxation times.

3.2.2 Experimental procedures

The melting of PE blown films was examined by using *in-situ* synchrotron SAXS and WAXD techniques. Differential scanning calorimetry (DSC) was first used to determine the thermal behavior of blown films without constraint. The heating rate of DSC was 1.1 ^{o}C/min. DSC measurements were carried out by using a Perkin-Elmer DSC 7 instrument. The blown film was heated under constrained conditions in the modified Linkam shear device to perform *in-situ* SAXS/WAXD measurements. The constraint was applied by mechanically sandwiching the film between two parallel plates. This instrument has been used for rheo-X-ray study of polymer melt under shear [15], where the confinement has been proven to be very effective on the sample. The heating rate for X-ray measurements was 0.96 ^{o}C/min. 2D WAXD and SAXS measurement were carried out at the X27C and X3A2 synchrotron beam lines in the National Synchrotron Light Source (NSLS), Brookhaven National Laboratory (BNL), respectively. The wavelengths of the synchrotron radiation were 1.366 Å (X27C) and 1.542 Å (X3A2). 2D SAXS and WAXD patterns were collected using MAR CCD X-ray detector (MARUSA) with the resolution of 1024×1024 pixels (pixel size = 158.44 μm). The data acquisition time was 15 seconds and the data storage time was 5 seconds for each image. The sample to detector distances for SAXS and WAXD were calibrated using AgBe (Silver Behenate) and Al_2O_3 (Aluminum Oxide) as standard samples, respectively. Corrections for background scattering, air scattering, sample absorption (?) and synchrotron beam fluctuation were carried out for all the X-ray images before analysis.

3.3 Results and discussions

3.3.1 DSC thermograms of unrestrained samples

DSC melting thermograms (at a 1.1 ^{o}C/min) for unrestrained blown films of LLDPE and HDPE/LLDPE blend are illustrated in Figure 3.2. The corresponding DSC melting temperatures obtained from Figure 3.2 (blown films) and quiescently crystallized LLDPE and HDPE/LLDPE binary blend (starting samples) are summarized in Table 3.2. In the melting of quiescently crystallized samples, the HDPE/LLDPE blend showed a slightly higher melting temperature than neat LLDPE (Table 3.2). The higher melting temperature of the blend is due to the presence of HDPE. This is because HDPE is a homopolymer having faster crystallization rate and higher crystallization temperature, which lead to the formation of thicker lamellae than LLDPE containing hexane branches (2.4 mole%).

The melting of blown films for both LLDPE and HDPE/LLDPE at the temperature range (90-140^{o}C) exhibited two discrete exotherms, $T_{m,L}$ and $T_{m,H}$, where the subscript L and H denoted the low and high melting temperatures, respectively. The presence of $T_{m,H}$ in LLDPE film can be attributed to the flow-induced crystalline structures, which is absent in the quiescently crystallized sample. The HDPE/LLDPE blend film showed higher values of $T_{\mathrm{m,H}}$ and the end melting temperature than those observed in LLDPE, implying the formation of thicker lamellae due to the presence of HDPE during the blowing process. It was also observed that the addition of HDPE accelerated the crystallization kinetics of the blend as compared to neat LLDPE (data not shown). The value of $T_{m,L}$ for each film was nearly the same as the nominal melting temperatures (T_{m}'s) of quiescently crystallized samples (Table 3.2). This implied that $T_{m,L}$

was related to the melting of lamellae formed under undeformed state (or within the oriented scaffold).

3.3.2 In-situ WAXD during restrained melting

In order to examine the flow-induced crystallization precursor structures in PE blown films, *in-situ* WAXD measurements were carried out on restrained samples at a heating rate similar to that of DSC. Selected 2D WAXD patterns of LLDPE and HDPE/LLDPE blend films at elevated temperatures are shown in Figures 3.3(a) and 3.3(b), respectively. Figure 3.3(c) illustrates the azimuthal profiles taken from the (110) reflection of both films at room temperature. It is seen that 2D WAXD patterns of both films exhibit four-arc (110) reflections at the off-axes and two-arc (200) reflections at the meridian, implying the formation of twisted lamellae. This is because the folded chain lamellae often grow epitaxially from the *c*-axis of the flow-induced row nuclei (shish) and they twist gradually around their crystallographic *b*-axis while staying perpendicularly to the machine direction (MD). The twisted lamellae are responsible for the formation of four-arc (110) reflections at the off-axes and two-arc (200) reflection at the meridian.[7-9]

It is noted that the blend film showed much more distinct (110) and (200) reflections at elevated temperatures (e.g. 116.4 and 126.4 ^{o}C in Figure 3.3(a)) than the LLDPE film. In particular, the oriented crystal reflections remained stable at temperatures above 126.4^{o}C for the blend, whereas the LLDPE film showed only a molten scattering background. This confirms that the thermal stability as well as the orientation of "residual crystallites" in the blend film are significantly higher than those

of LLDPE. Such residual crystallites can be attributed to the first formed crystallization precursor structures during film blowing, which is explained as follows. As the blend contains 1.0 wt% of HMW-HDPE, which is above its overlap concentration, the long HMW-HDPE chains are in the highly entangled state at high temperatures. Upon the application of shear, some fractions of chains can undergo the coil-stretch transition and form extended chain conformation. Crystallization of the extended-chains would take place subsequently and form shish. The shish entity can then induce folded chain crystallization of interconnected as well as disconnected adjacent coiled chain sections and form kebabs.[20] The thermal stability of such shish-kebab structures resulted primarily from the HMW-HDPE component would be much higher than the crystalline structures resulted from LMW-HDPE and LLDPE components. This scenario is consistent with DSC results. We note that as the average molecular weight of LMW-HDPE is lower than LLDPE, the presence of 4 wt% LMW-HDPE may be considered as a diluent in the LLDPE matrix. However, the role of HMW-HDPE on the formation of high temperature stable crystallization precursor structures (i.e. shish kebabs) is unmistakable. In the following, the crystallinity change during melting will be discussed to further illustrate our point.

3.3.3 Crystallinity Change

Frasier corrected 2D WAXD pattern was analyzed to determine the crystallinity index [21,] which is proportional to the true crystallinity and will be termed 'crystallinity' hereafter. The crystallinity index was estimated from Equations (2).

$$X_c = \frac{I_c}{I_t},\ I_t = I_c + I_a \tag{2}$$

where I_c and I_a represent the reflections of the crystal phase (sum of (110) and (200) reflections) and of the amorphous phase, respectively, I_t is the total diffraction intensity due to the sum of amorphous and crystal phases.

In order to obtain the oriented crystals fraction or orientation fraction, X_{or}, the total integrated crystalline reflections, I_c, was deconvoluted into two contributions from oriented and unoriented fractions, using the "Halo" method.[22] The total integrated intensity, I_c, thus has two contributions, (1) I_u, which is due to reflection from the unoriented crystals, and (2) I_{or}, originated by reflections from the oriented crystals. The total crystalline reflections can be represented as follows:

$$X_{or} = \frac{I_{or}}{I_c},\ I_c = I_u + I_{or} \tag{3}$$

where reflection by amorphous phase, I_a, was already subtracted.

The changes of total crystallinity, X_c, and orientation fraction, X_{or}, are depicted in Figures 3.4(a) and 3.4(b) as a function of temperature, respectively. Initially, the crystallinities of both films were comparable, while the orientation fractions of the blend film were significantly higher at the temperatures below 108 ^{o}C. However, when the temperature was elevated above 108 ^{o}C (dotted vertical line in Figure 3.4(a)), the crystallinity of the blend film began to dominate. In addition, the change of orientation fraction in the LLDPE film showed steep increase above 108 ^{o}C, indicating the drastic melting of unoriented crystals, where the blend film only showed a moderate increase in orientation fraction. This can be explained as follows. During the film blowing process, even LLDPE can produce two distinct crystalline structures: a flow-induced precursor scaffold containing thermally stable shish-kebab crystalline structures, and crystallites

formed within the scaffolds upon cooling. The latter would resemble the crystallites formed under quiescent state and thus have low orientation and low thermal stability. Thus, upon heating, the crystallites of low orientation and low thermal stability melt first (at above 108 ^{o}C), leaving behind a more stable crystalline scaffold with high orientation. However, it is clear that the concentration of flow-induced scaffold in LLDPE film is significantly lower that that in HDPE/LLDPE blend. This again confirms the role of HMW-HDPE, which significantly improves the crystallization rate, crystallization temperatures and orientation fraction when compared to those in LLDPE under the same film blowing conditions.

3.3.4 In-situ SAXS during restrained melting

Selected 2D SAXS patterns of LLDPE and the blend film collected during heating are represented in Figures 3.5(a) and 3.5(b), respectively. In addition, the corresponding change of total scattered intensity at selected temperatures near and above the high nominal melting temperatures (i.e. $T_{m,H}$ in DSC) is plotted in Figure 3.5(c). We note that the initial films exhibited both oriented and unoriented scattering features. The orientation of the HDPE/LLDPE blend film was significantly higher than LLDPE at room temperature as well as at elevated temperature. One of the most interesting features found in Figures 3.5(a) and 3.5(b) was that the high temperature SAXS patterns (e.g. above 119 ^{o}C) did not show equatorial streak, which typically represents the presence of shish. Instead, these patterns exhibited “meridional streak”, quite different from the “meridional peak” seen at low temperatures (e.g. below 110 ^{o}C). The meridional peaks are due to the formation of oriented lamellar structure having very large lateral

dimensions, while the meridional streak can be attributed to the formation of shish-kebabs with much smaller lateral kebab diameter (if assumed disk like) and a large polydispersity in their diameter. The latter has recently been demonstrated by us using a shish kebab model to simulate varying scattering patterns as functions of kebab diameter, long period, kebab thickness and their variances[23]. This absence of the equatorial streak does not mean that the shish was absent, it simply means that the dimension of the shish may be too small and/or the concentration too dilutes to be detected by SAXS.

In Figures 3.5(a) and 3.5(b), it is interesting to see that at 126.4 ^{o}C (above $T_{m,H}$ of both samples), the HDPE/LLDPE blend film still exhibits oriented scattering features (i.e. meridional streak), while LLDPE film shows nearly isotropic scattering pattern, typical of molten melt. Based on the plot of total scattered intensity versus temperature (Figure 3.5(c)), the end temperature for each film can be determined: 127.5 ^{o}C (for LLDPE) and 129.4 ^{o}C for (HDPE/LLDPE). These two temperatures are close to the end temperatures (ca. 126 ^{o}C for LLDPE and 128 ^{o}C for HDPE/LLDPE) determined by DSC using unrestrained films (Figure 3.2).

The lamellar long period was found to decrease at higher temperatures (> 119.8 for LLDPE and > 121.7 ^{o}C for HDPE/LLDPE), which was unexpected based on the conventional concept of lamellar melting. This observation can be explained as follows. The decrease in long period is related to the transition from meridional peaks to meridional streak in SAXS (Figure 3.5). The meridional peaks are due to the scattering of the lamellar structure with relatively high misorientation; while the meridional streak can be attributed to the scattering of the oriented shish-kebab scaffold after the melting of dominant lamellae formed at low temperatures. The conventional approach for the analysis of meridional peaks to determine the lamellar thickness involves the use of peak

position from Lorentz-corrected profiles (Figure 3.5(b)). The Lorentz correction (Is^2) is needed to compensate the misorientation of lamellae. However, this correction is no longer suitable for the analysis of the meridional streak, where the degree of misorientation is low in oriented shish kebabs. In the following, we demonstrate that the method devised by Ruland for investigation of scattering streak can be used to analyze the kebab lateral dimension (or diameter if we assume the kebab is disk-like) and orientation distribution as well as their temperature dependences during further melting.

3.3.5 Ruland streak analysis to estimate the kebab diameter and orientation in precursor structure

The Ruland's streak analysis method was first introduced to separate the size and the orientation distributions of longitudinal voids in polymer and carbon fibers from the equatorial streak of the SAXS pattern.[24,25] However, since the method is principally based on the separation of experimental azimuthal breadth from contributions of scatterer length and misorientation, the method can also be applied to meridional streak in separating the average kebab diameter, $\langle D \rangle$, and its misorientation in the shish-kebab structure. If one assumes that all azimuthal distributions can be modeled by Lorentz functions, the observed azimuthal width, $B_{\mathrm{obs}}(s)$ (where $s = 2\sin\theta/\lambda$ with being the scattering angle and being the wavelength) is related to the kebab diameter, $\langle D \rangle$, and the azimuthal width, B_{ϕ}, due to misorientation of kebabs along the shish by the following equation.

$$B_{obs}(s) = \frac{1}{\langle D \rangle \cdot s} + B_{\phi} \tag{4}$$

If all azimuthal distributions can be modeled by Gaussian functions, then the relationship becomes

$$B_{obs}{}^2 = \left(\frac{1}{\langle D \rangle \cdot s} \right)^2 + B_{\phi}{}^2 \tag{5}$$

Since the Lorentzian function gave better fits to our experimental results, Equation (4) was used to analyze the meridional streak. The kebab diameter, $\langle D \rangle$, was determined from the slope of the B_{obs} vs. $1/s$ plot, where the intercept yields the azimuthal integral width, B_{ϕ}. Figure 3.6(a) illustrates the calculated kebab diameter as a function of temperature at the shish kebab stable temperature region ($T > 119.8$ for LLDPE and $T >$ 121.7 ^{o}C for HDPE/LLDPE). The corresponding value of B_{ϕ} is shown in Figure 3.6(b). It is interesting to see that the thermal stability of the kebabs in LLDPE (119.8 – 127.5 ^{o}C) is lower than that in HDPE/LLDPE blend (121.7 – 129.4 ^{o}C). This is reasonable since the kebab moiety in the HDPE/LLDPE blend is mainly due to the HMW-HDPE component, which would result in larger crystal thickness and thus higher melting temperature than the LLDPE kebabs. The formation of the LLDPE kebabs is probably also from the high molecular species.

Two interesting features are observed in Figure 3.6(a). (1) The average diameter of the LLDPE kebabs is lower than that of the HDPE kebab. (2) During heating, the diameter change of the LLDPE kebabs is small (ca. 180 to 80 nm), while the diameter change of the HDPE kebabs is large (ca. 540 to 100 nm). In Figure 3.6(b), the value of B_{ϕ}, due to the misorientation of kebabs is found to increase monotonically with temperature for both LLDPE and HDPE/LLDPE films. This behavior reflects the melting process of the shish-kebab structure, where the aligned kebabs would loose their orientation at high

temperatures. The initial B_ϕ value of the HDPE kebabs is lower than that of the LLDPE kebabs, which indicates that the initial HDPE shish kebabs in the blend has a better orientation.

To confirm the role of the HMW-HDPE component on the formation of a thermally stable crystallization precursor scaffold during flow, the following experiment was also carried out. After the complete melting, which was confirmed by both SAXS and WAXD measurements, both sample were held at 135 ^{o}C for 10 minutes and then subsequently cooled down to room temperature. The 2D SAXS images of LLDPE and HDPE/LLDPE melted films at room temperature are shown in Figures 3.7(a) and 3.7(b), respectively. It is seen that the orientation of the HDPE/LLDPE blend remains high, where the LLDPE sample shows almost no orientation. This indicates that the extended chain conformation of the HMW-HDPE component is not completely relaxed back to the coiled state at 135 ^{o}C, while near all the chains in LLDPE completely coil back. The reversibility of the shish-kebab formation under the restrained condition will be a subject of our future study.

3.3.6 Vonk analysis (for single lamella scattering) to estimate the kebab thickness in precursor structure

According to Vonk,[26] in a dilute lamellar system, where the lamellae are uncorrelated and thus the first-order interference is not discerned, the relationship between the lamellar thickness, l, and the scattered intensity, $I(s)$ can be given by

$$I(s) = \frac{P \sin^2(\pi l s)}{(\pi l s)^2 s^2} \tag{6}$$

where P is a constant. The sine function in equation (6) can be expanded and approximated as

$$I(s) = \frac{P}{s^2} - \frac{1}{3}\pi^2 l^2 P \tag{7}$$

At high temperatures (T > 119.8 for LLDPE and T > 121.7 ^{o}C for HDPE/LLDPE), the scattering interference peak in the meridional streak is very weak and disappears with the further increase in temperature. We expect that the correlation between the kebabs is very low during melting because of the following reasons: (1) the expected average separation distance between the kebabs is large (> 55 nm as in Figure 3.6(a)) in the shish kebab structure, and (2) the misorientation of the kebabs becomes very high with temperature (Figure 3.7(b)). The sliced meridional profile of the vertical scattering streak thus represents the density profile of the kebabs intercepted along the shish axis, which may fit the criterion of single lamella scattering by Vonk. Figure 3.9(a) illustrates the typical plot of $I(s)$ versus $1/s^2$ for a high temperature SAXS profile in LLDPE, where the weight average thickness of the kebab, l, can be estimated by Equation (7). The experimental and fitted SAXS intensity profiles for LLDPE at selected temperatures are plotted in Figure 3.9(b); the calculated kebab thicknesses for both LLDPE and HDPE/LLDPE samples are illustrated in Figure 3.9(c). It is seen that the kebab thickness for both samples exhibit the same linear temperature dependency, even though the chain architecture, composition and branch distribution between LLDPE and HDPE are quite different. HDPE is a linear homopolymer, which usually has fast crystallization rate and forms thick lamellae. In contrast, LLDPE is matallocene-based copolymer containing 12 hexene branches per 1000 carbon atoms. As the side-branches (α-olefins) cannot be

incorporated in the crystalline structure, the relatively short linear sequence in LLDPE often hinders the formation of thick lamellae.

3.3.7 Estimate of equilibrium melting temperature

We can safely assume that the kebab thickness estimated by the above method represent its equilibrium value at the corresponding temperature, since *in-situ* X-ray measurement were performed under the relatively slow heating rate (0.96 ^{o}C/min). Thus, the relationship between the kebab thickness and temperature can be used to determine the equilibrium melting temperature, T_m^o, for PE. The T_m^o value is defined as the melting temperature of the lamella with infinite thickness.[27] Since the crystallization phenomenon such as lateral growth rate and nucleation rate is controlled by the degree of supercooling, ΔT ($\equiv T_m^o - T_c$), T_m^o has been one of the most important physical quantities for crystallization in polymers. Accordingly, a great deal of efforts and approaches are seen in the literature to determine the reliable T_m^o value especially for PE.[27-35] Two methods have often been used to determine T_m^o. One is the Gibbs-Thomson method, and another is the Hoffman-Weeks method, typically used for the analysis of the thermal analysis data.

Our experimental data was analyzed by the Gibbs-Thomson equation expressed as follows[36]

$$T_m = T_m^o \left[1 - \frac{2\sigma_e}{l \rho_c \Delta H_u^o} \right] \tag{8}$$

where σ_e represents the lamellar fold surface free energy, ΔH_u^o is the heat of fusion per unit mass, and ρ_c is the crystal phase density,. Thus, by plotting the melting temperature, T_m, versus measurable reciprocal of lamellar thickness, $1/l$, the intercept gives the value

of $T_m°$ at $l = \infty$. Using the thickness data for both LLDPE and HDPE kebabs, estimated by the Vonk method, as a function of temperature, we have extrapolated $T_m°$ value to be 142.6 ^oC, which was lower than the value for perfect linear PE suggested by Flory (145.5 ^oC) [27]. We consider our estimated value to be in a reasonably good agreement with the theoretical value. The discrepancy between experimental T_m^o and thermodynamic value (by Flory) can be attributed to the non-equilibrium crystallization conditions, resulted from the kinetic constraints, such as limited transport of chain segments to growth face and secondary nucleation barrier. Although the chosen heating rate was relatively small (0.97 ^oC/min), the kinetic constraint of less or noncrystallizable chains in the chosen systems cannot be totally eliminated.

3.4 Conclusions

In-situ synchrotron SAXS and WAXD were utilized to examine the nature and thermal stability of flow-induced crystallization precursor structures in LLDPE and HDPE/LLDPE blown films during restrained melting. Around the high nominal melting temperature ($T_{m,H}$ in DSC), both LLDPE and HDPE/LLDPE blend samples exhibited oriented crystalline reflections in WAXD and meridional streak in SAXS, which are characteristics of kebabs in the first formed shish kebab structures. By using the Ruland streak analysis, the average kebab diameter and the orientation distribution width were estimated. Results indicated that during melting, both kebab diameter and orientation decrease with temperature. The loss of correlation between the kebabs allowed us to use the Vonk method for single lamella scattering to estimate the average kebab thickness, which was found to increase linearly with temperature for both LLDPE and

HDPE/LLDPE samples. The presence of HMW-HDPE, which was above the overlap concentration (c^*), exhibited a profound role of enhancing the flow-induced crystallization precursor structures (shish kebabs) at high temperatures, which caused faster crystallization rate and higher crystal orientation for the blend. Even after the film was held in the molten state at 135 ^oC for 10 min, the extension and orientation of the HMW-HDPE chains did not completely relax and continued to provide nucleating sites for the LLDPE/HDPE matrix upon cooling, evidenced by the nature (oriented) of the room temperature 2D SAXS patterns. The relations between the kebab thickness and temperature (above $T_{m,H}$) for both LLDPE and HDPE/LLDPE samples were used to determine the equilibrium melting temperature (T_m^o = 142.6 ^oC) using the Gibbs-Thomson equation. The estimated T_m^o value was in a reasonable agreement with the theoretical value (T_m^o = 145.5 ^oC) predicted by Flory, where the discrepancy might be due to the non-equilibrium crystallization conditions during SAXS measurement.

3.5 References

1. Kobayashi, K.; Nagasawa, T. J. *Macromol. Sci. (Phys.)* **1970**, *B4*, 331.
2. Flory, P. J. *J. Chem. Phys.* **1974**, *15*, 397.
3. Ziabicki, A.; Jarecki, L. In High-Speed Fiber Spinning; Ziabicki, A., Kawai, H., Eds.; Wiley: New York, **1985**; 225.
4. Somani, Rajesh H.; Yang, Ling; Hsiao, Benjamin S.; Agarwal, Pawan K.; Fruitwala, Hitesh A.; Tsou, Andy H. *Macromolecules* **2002**, *35*, 9096.
5. Yang, L.; Somani, R. H.; Sics, I.; Hsiao, B. S.; Kolb, R.; Fruitwala, H.; Ong, C. *Macromolecules* **2004**, *37(13)*, 4845.

6. Somani, R. H.; Yang, L.; Sics, I.; Hsiao, B. S.; Pogodina, N. V. H. H. Winter, P. Agarwal, H. Fruitwala, A. Tsou, *Macromol.Symp.* **2002**, *185*, 105.

7. Keller, A., and Machin. M.J. *Macromol. Sci. (Phys.)* **1967**, *B1*, 41.

8. Pazur, J. M., Prud'homme, R.E. *Macromolecules* **1996**, *29*,119.

9. Lu, J., and Sue, H. J. *Macromolecules* **2001**, *34*, 2015.

10. Prasad, A., Shrof, R., Rane, S., and Beaucage, G. *Polymer* **2001**, *42*, 3103.

11. Wang, K.H., Koo, C. M, and Chung, I. J. *J. Appl. Polym. Sci.* **2003**, *89*, 2131.

12. Luettmer-Strathmann, J., and Lipson, J. E. G. *Macromolecules* **1999**, *32*, 1093.

13. Agamalian, M., Alamo, R. G. Kim, M. H., Londono, J. D., Mandelkern, L., and Wignal, G. D. *Macromolecules* **1999**, *32*, 3093.

14. Ruzette, Anne-Valerie G., and Mayes, Anne M. *Macromolecule*s **2001**, *34*, 1894.

15. Somani, R. H.; Hsiao, B. S.; Nogales, A.; Srinivas, S.; Tsou, A. H.; Sics, I.; Balta-Calleja, F. J.; Ezquerra, T. A. *Macromolecules* **2000**, *33*, 9385.

16. Seki, M.; Thurman, D. W.; Oberhauser, J. P.; Kornfield, J. A. *Macromolecules* **2002**, *35*, 2583.

17. Pogodina, N. V.; Lavrenko, V. P.; Winter, H. H.; Srinivas, S. *Polymer* **2001**, *42*, 9031.

18. de Gennes, P. G., Scaling Concepts in Polymer Physics, Cornell University Press, 1979, Ithaca, NY.

19. Ballard, D. G. H.; Cheshier, P.; Longman, G. W.; Schelten, J. *Polymer* **1978**, *19*, 379.

20. Dukovski, I., Muthukumar, M. *J. Chem. Phys.* **2003**, *118*, 6648.

21. Ran, S.; Zong, X.; Fang, D.; Hsiao, B. S.; Chu, B.; Phillips, R. A. *Macromolecules* **2001**, *34(8)*, 2569.

22. Ran, S., Zong, X., Fang, D., Hsiao, B. S., Chu, B., Ross, R. *J. Appl. Crystallogr.* **2000**, *33*, 1031.

23. Keum, J. K.; Burger, C.; Hsiao, B. S.; Somani, R.; Yang, L.; Kolb, R.; Chen, H.; Lue, C. T. *Progress in Colloid and Polymer Science* **2005**, accepted.

24. Perret, R.; Ruland, W. *J Appl. Cryst.* **1969**, *2*, 209.

25. Ruland, W. *J. Polym. Sci. Part C* **1969**, *28*,143.

26. Vonk, C. G.. *J. Polym. Sci., Polym. Phys. Ed.* **1985**, *23*, 2539.

27. Flory, P. J. *Trans. Faraday Soc.* **1955**, *51*, 848.

28. Crist, B., Howard, P. R. *Macromolecules* **1999**, *32*, 3057.

29. Mirabella, F. M., Westphal, S. P., Fernando, P. L., Ford, E. A., Williams, J. G. *J. Polym. Sci. Polym. Phys. Ed.* **1988**, *26*, 1995.

30. Krigas, T., Carella, J., Struglinski, M., Crist, B., Graessley, W. W., Schilling, F. C. *J. Polym. Sci. Polym. Phys. Ed.* **1985**, *23*, 509.

31. Roe, R. J., Bair, H. E. *Macromolecules* **1970***, 3*, 454.

32. Yamada, K., Hikosaka, M., Toda, Yamazaki, S., Tagashira, K. *Macromolecules* **2003***, 36*, 4790.

33. Sanchez, I. C., Eby, R. K. *Macromolecules* **1975***, 8*, 639.

34. Fischer, E. W., Schnidt, G. F. *Angew. Chem.* **1962***, 74,* 551.

35. Statton, W. O., Geil, P. H. *J. Appl. Polym. Sci.* **1960***, 9,* 357.

36. Wunderlich, B. *Macromolecular Physics*, Academic, New York 1973

Table 3.1

Samples	Density, ρ (g/cm^3)	$\overline{M}_w$ (kg/mol)	$\overline{M}_n$ (kg/mol)	MWD ($\overline{M}_w / \overline{M}_n$)
LLDPE[a]	0.920	116	48	2.4
HDPE[b]	0.964	130	15	8.7

[a] Polymerized with 2.4 mole % of hexene comonomer using the metallocene catalyst method.

[b] Polymerized with the Ziegler-Natta catalyst method, which contained a bimodal molecular weight distribution ($\overline{M}_w$ =99 kg/mol at about 80 wt % and 1,100 kg/mol at about 20 wt%).

Table 3.2

Samples	Quiescently crystallized samples	Blown films	
	T_m (°C)	$T_{m,L}$ (°C)	$T_{m,H}$ (°C)
HDPE/LLDPE	114.9	115.5	122.2
LLDPE	113.2	114.1	118.0

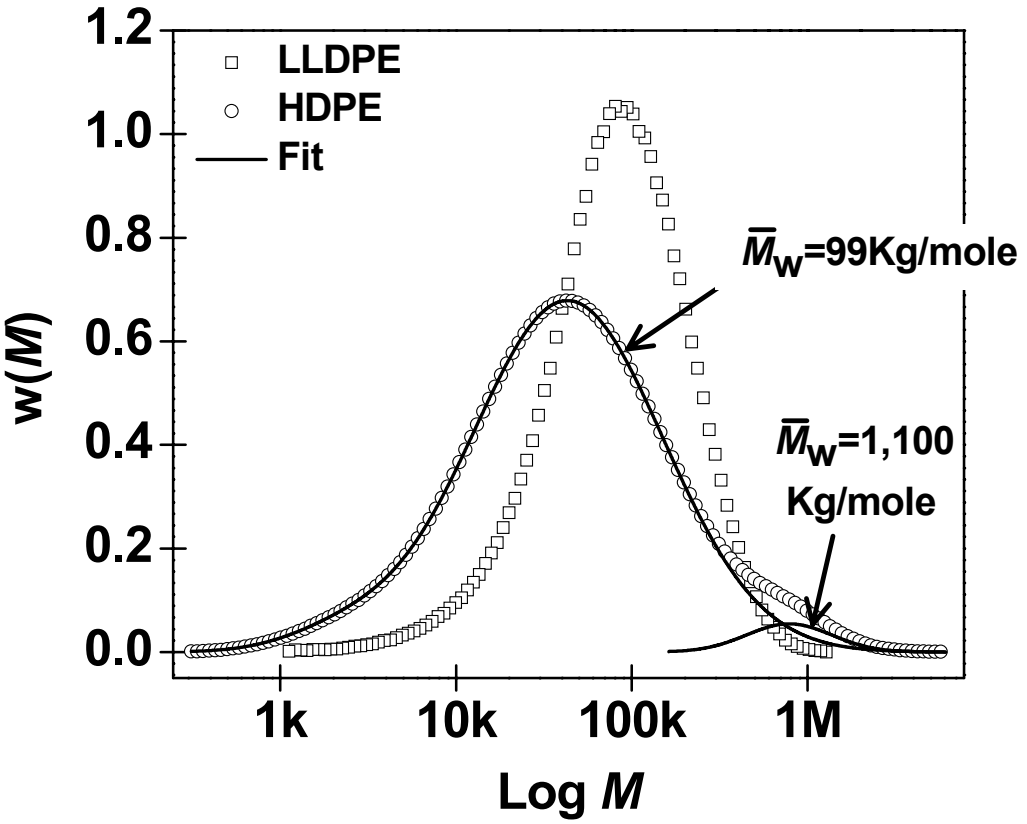
LLDPE
HDPE
Fit
$\bar{M}_w$=99Kg/mole
$\bar{M}_w$=1,100
Kg/mole
w(M)
Log M
1.2
1.0
0.8
0.6
0.4
0.2
0.0
1k
10k
100k
1M

Figure 3.1

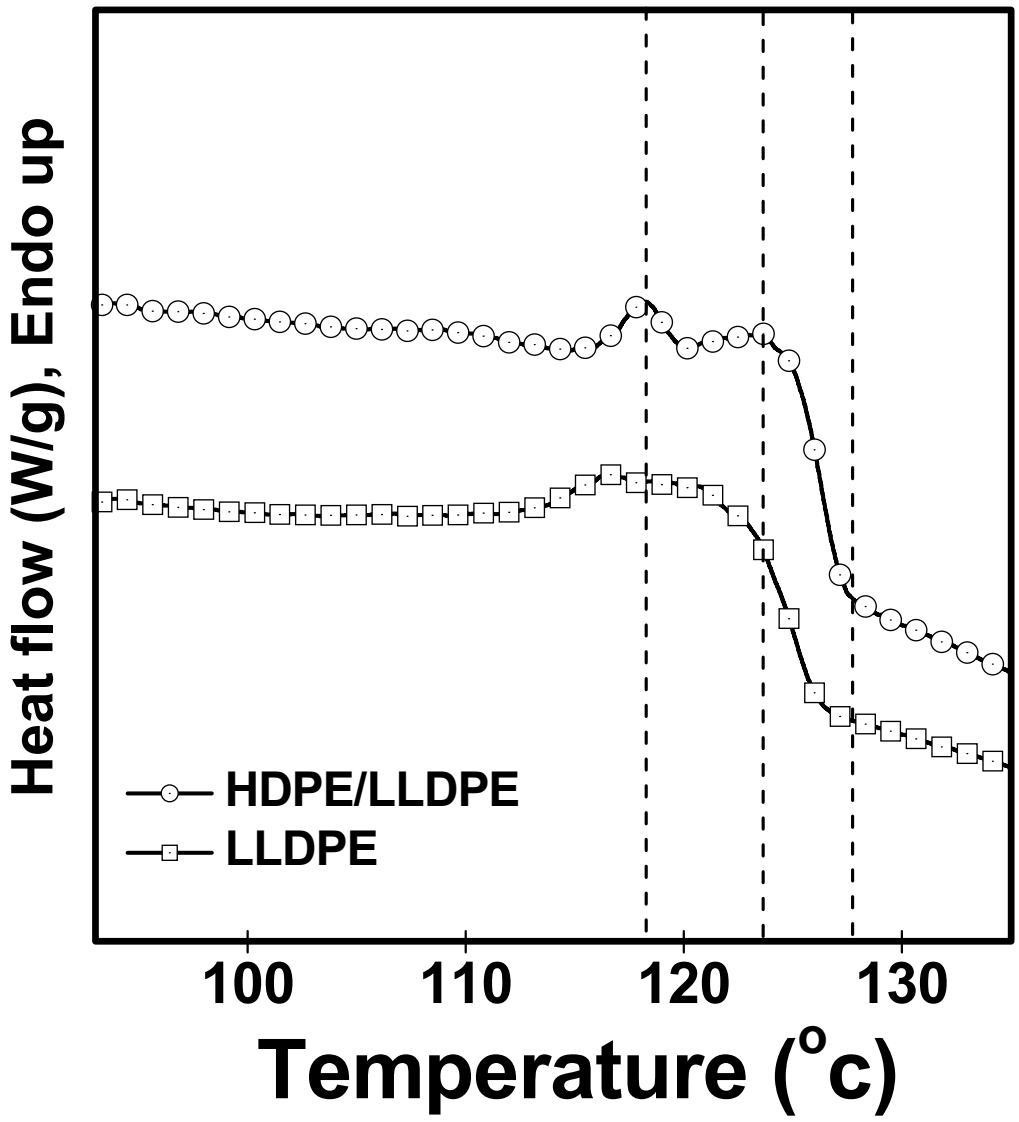
Heat flow (W/g), Endo up
HDPE/LLDPE
LLDPE
100
110
120
130
Temperature (°c)

Figure 3.2

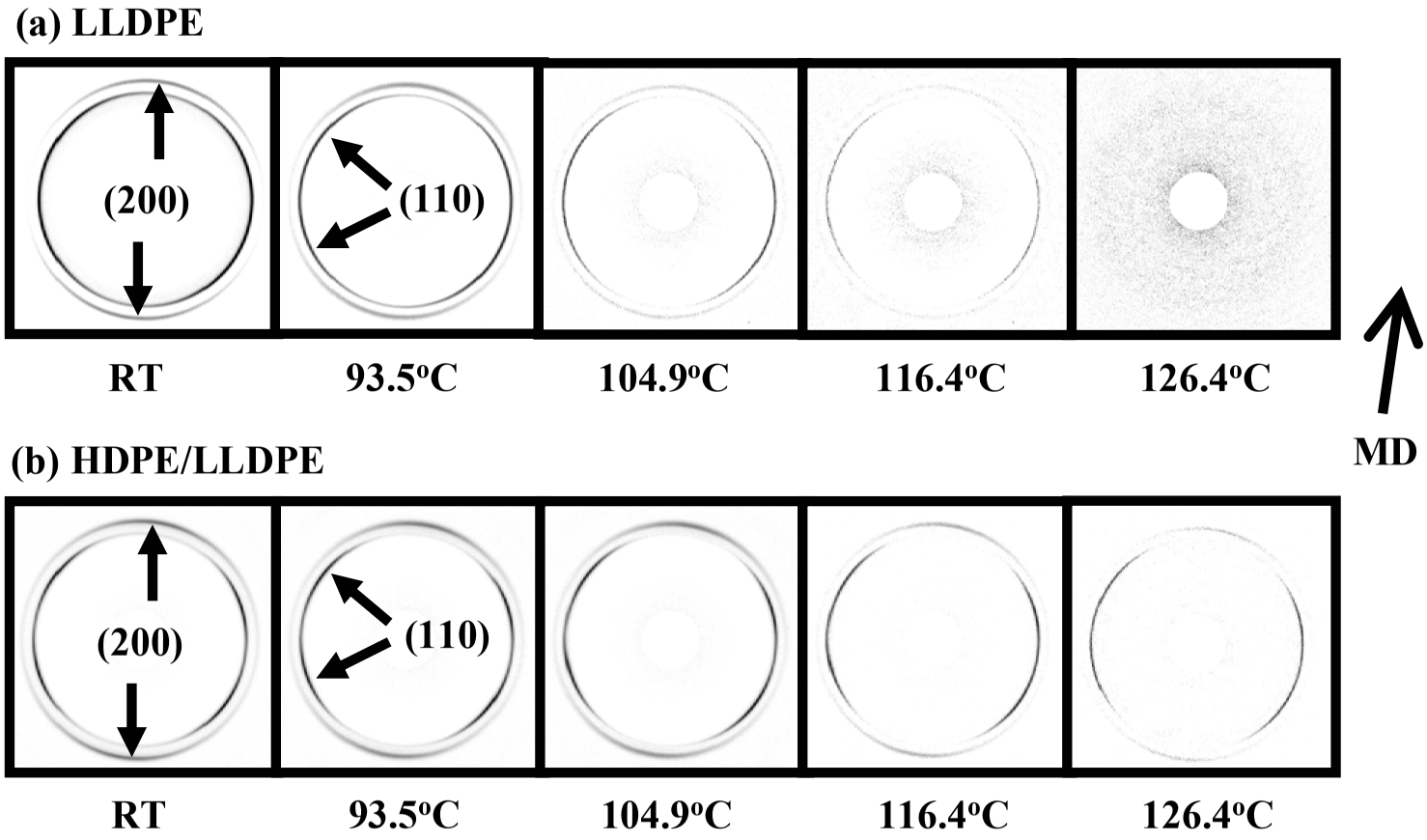

Figure 3.3(a) and 3.3(b)

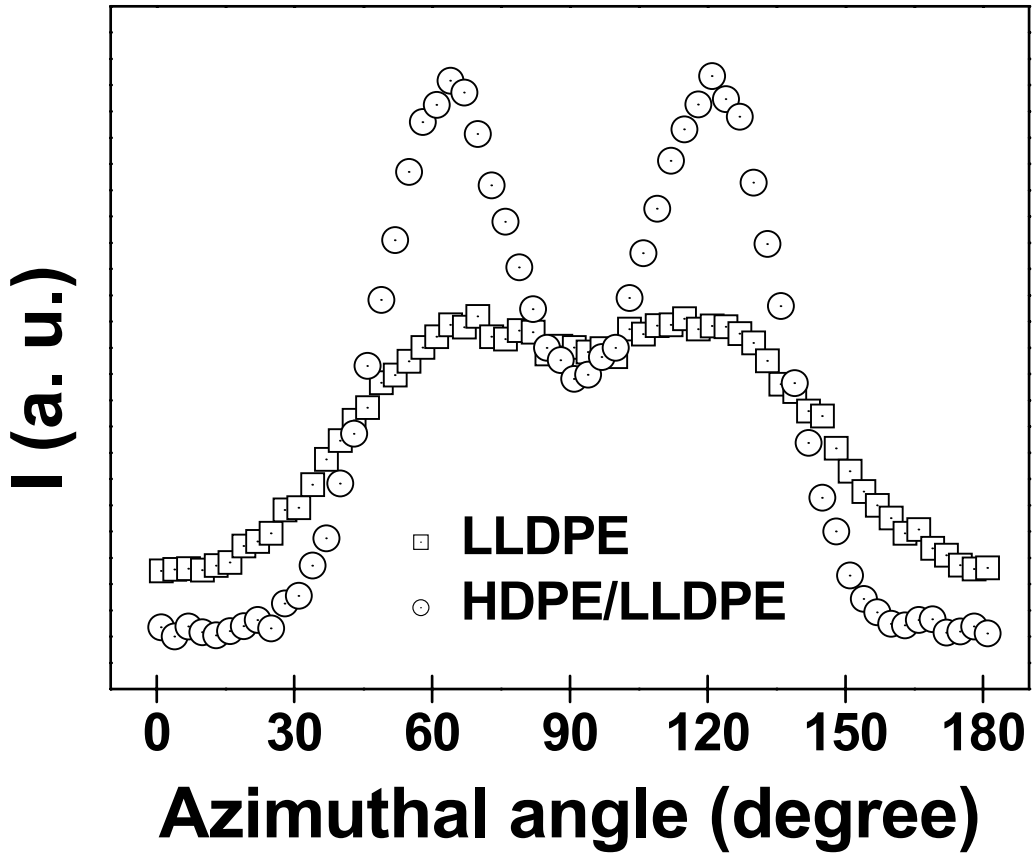
I (a. u.)
LLDPE
HDPE/LLDPE
0
30
60
90
120
150
180
Azimuthal angle (degree)

Figure 3.3(c)

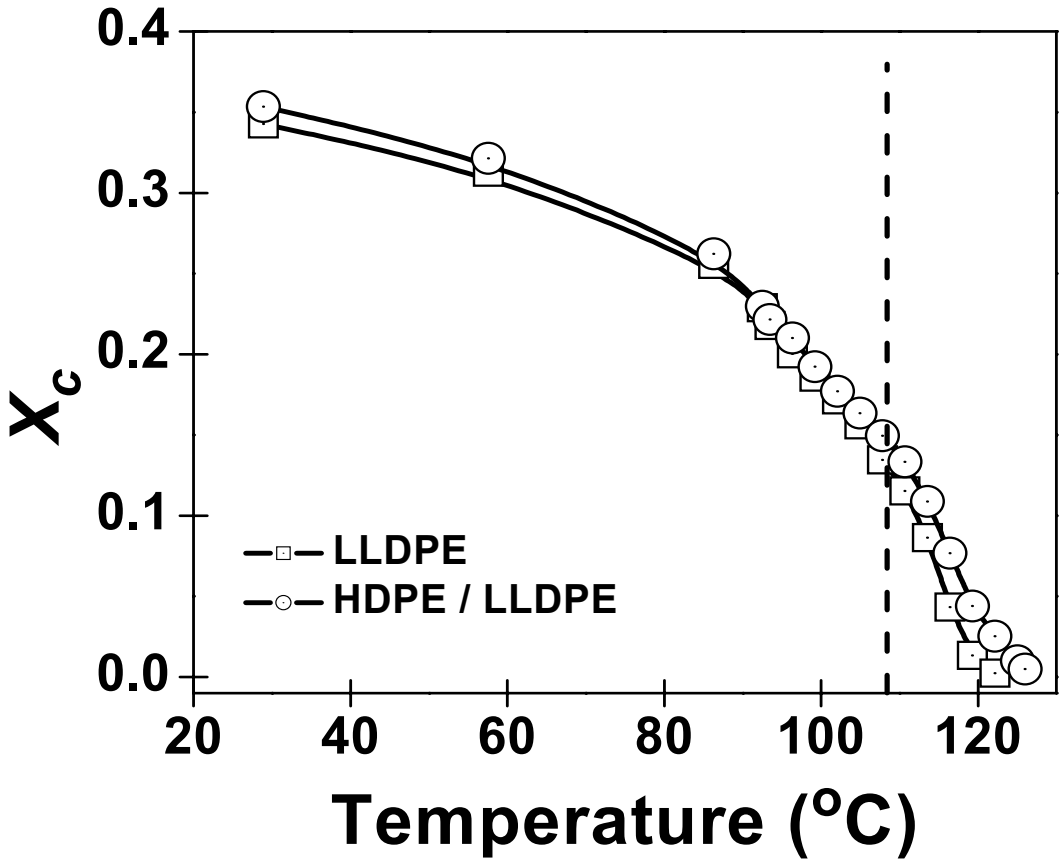
0.4
0.3
0.2
0.1
0.0
X_c
LLDPE
HDPE / LLDPE
20
40
60
80
100
120
Temperature (^{o}C)

Figure 3.4(a)

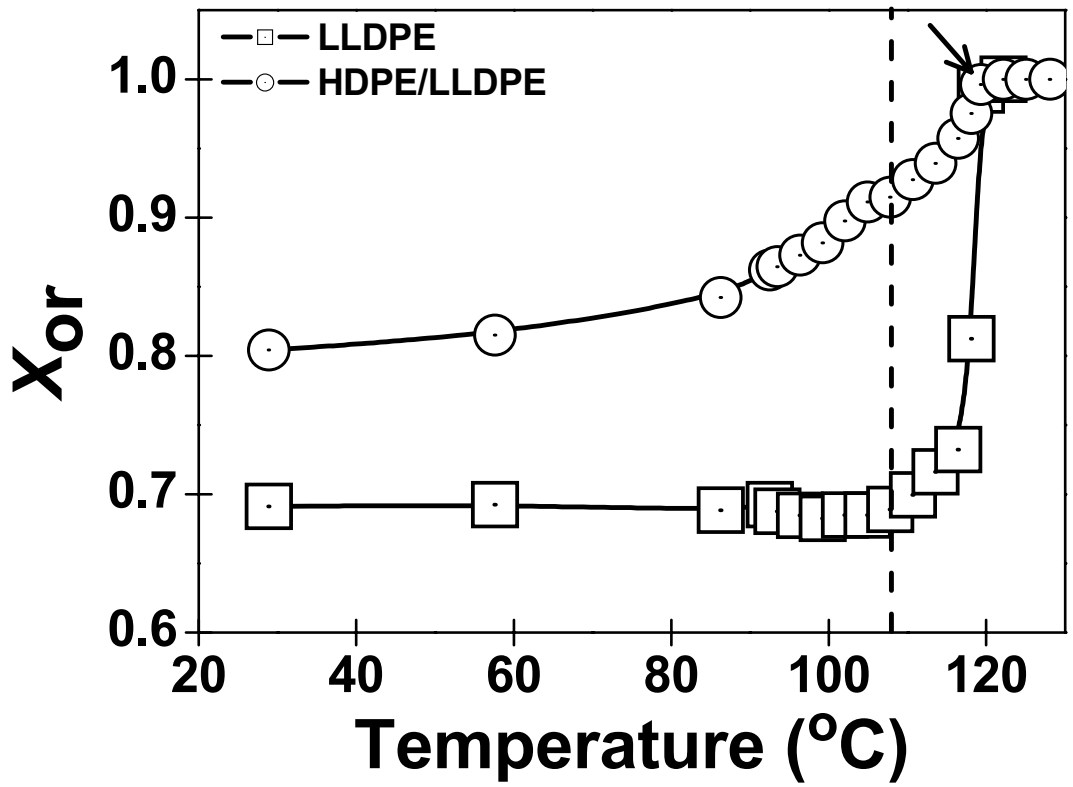
LLDPE
HDPE/LLDPE
1.0
0.9
0.8
0.7
0.6
X_{or}
20
40
60
80
100
120
Temperature (°C)

Figure 3.4(b)

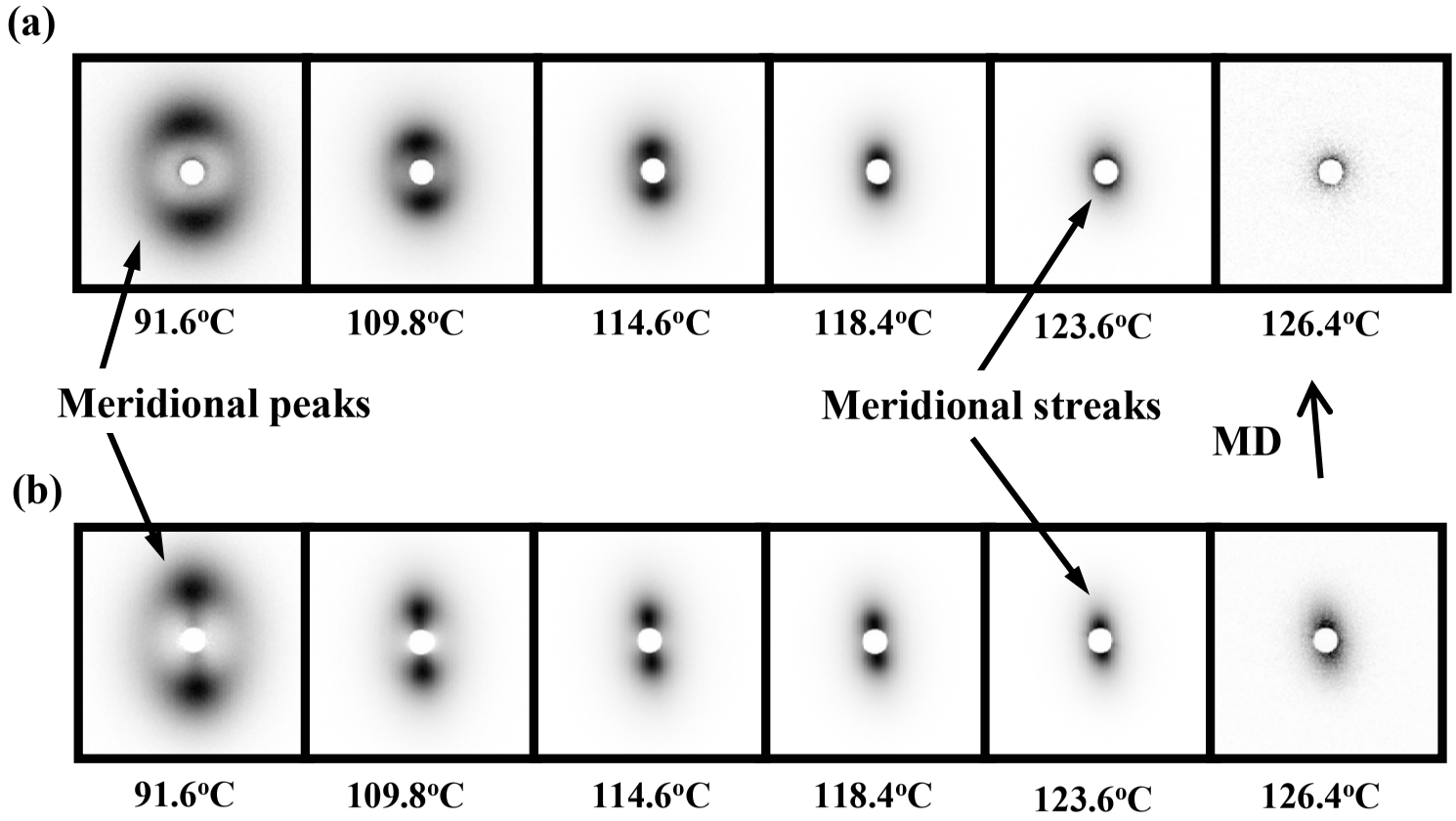

Figure 3.5(a) and 3.5(b)

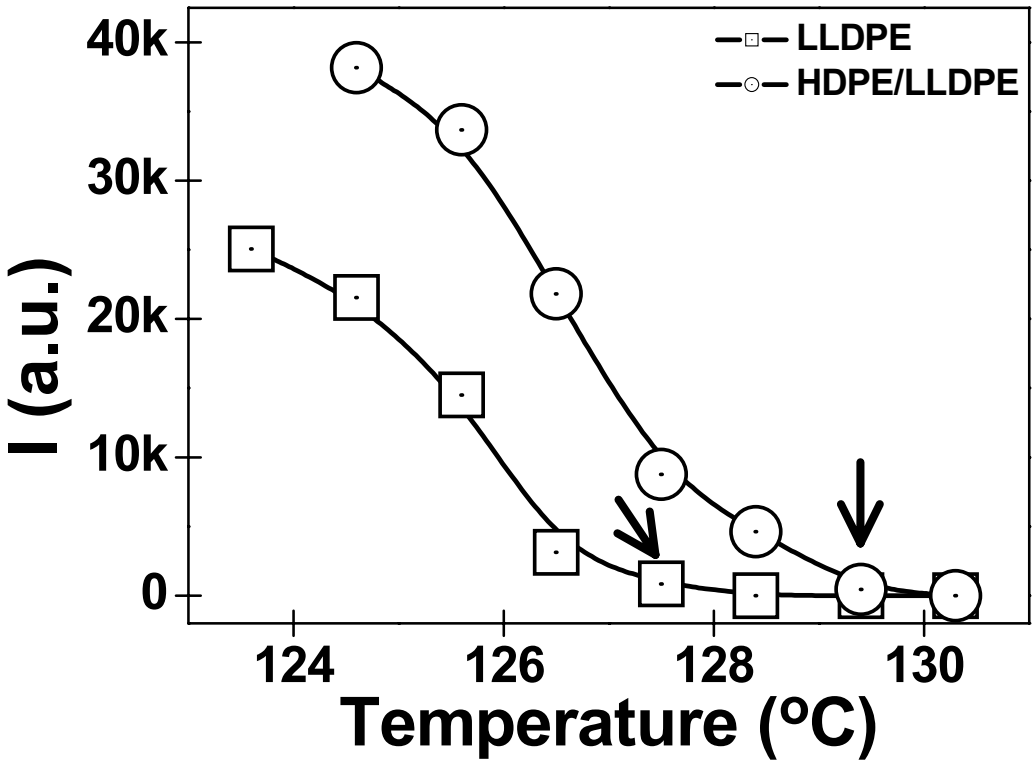
LLDPE
HDPE/LLDPE
40k
30k
20k
10k
0
I (a.u.)
124
126
128
130
Temperature (ºC)

Figure 3.5(c)

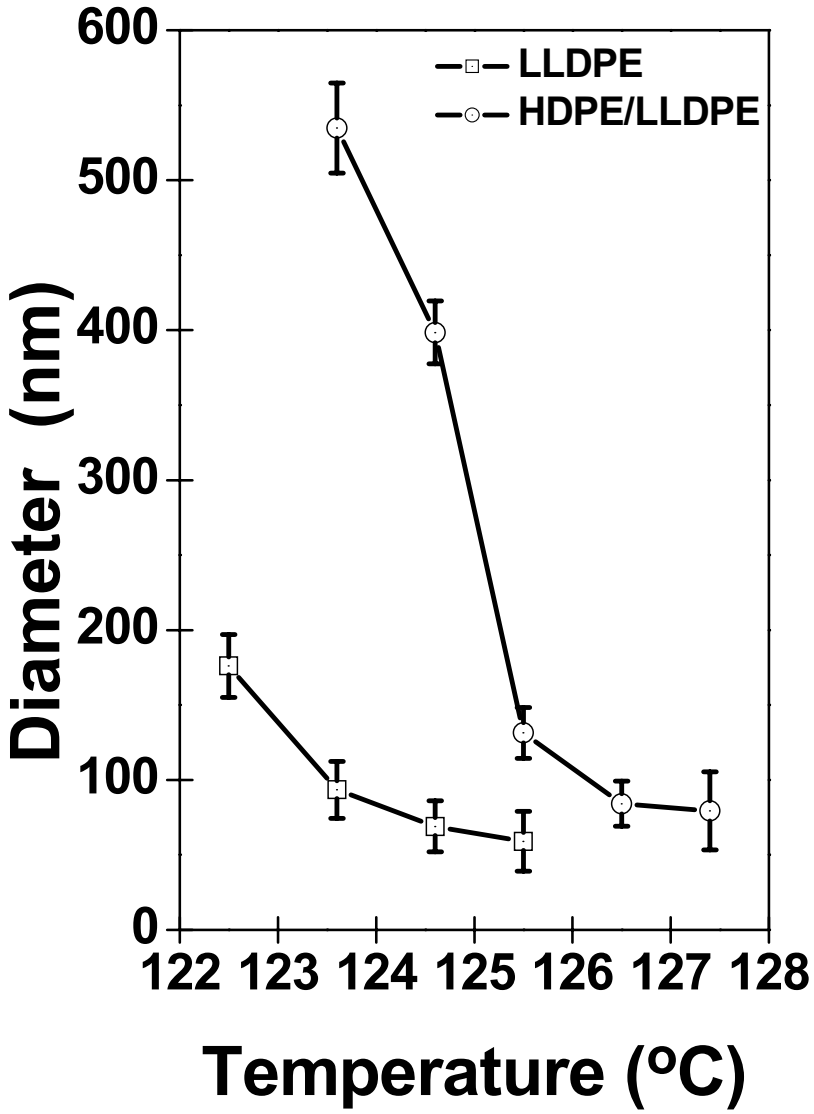
LLDPE
HDPE/LLDPE
Diameter (nm)
600
500
400
300
200
100
0
122 123 124 125 126 127 128
Temperature (ºC)

Figure 3.6(a)

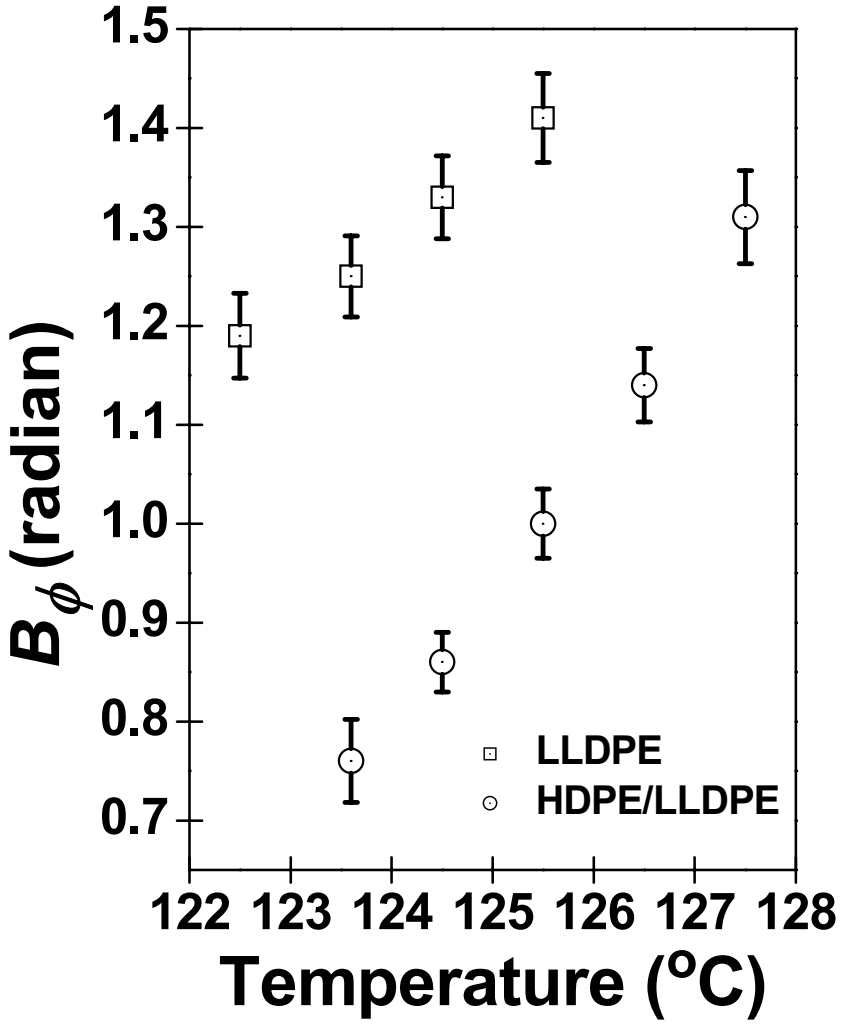
1.5
1.4
1.3
1.2
1.1
1.0
0.9
0.8
0.7
B_ϕ (radian)
LLDPE
HDPE/LLDPE
122 123 124 125 126 127 128
Temperature (°C)

Figure 3.6(b)

(a) LLDPE **(b) HDPE/LLDPE**

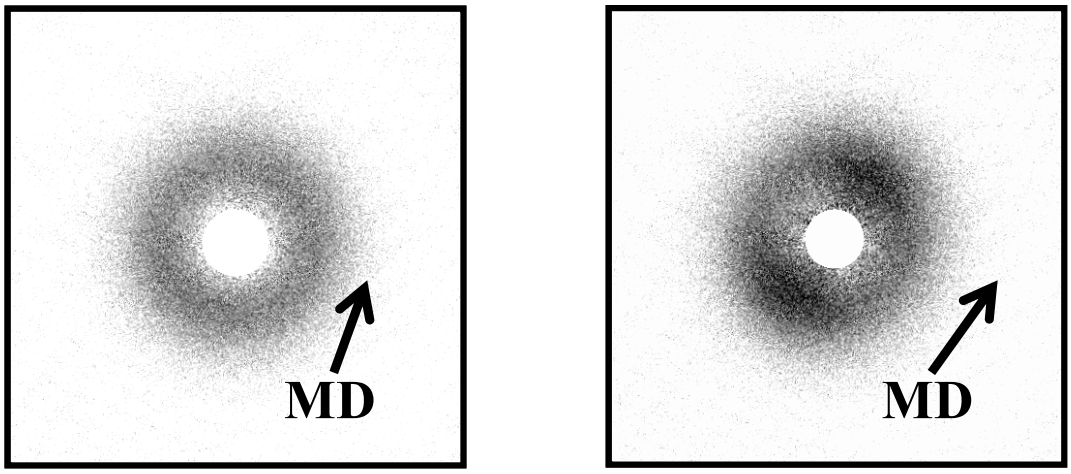

Figure 3.7(a) and 3.7(b)

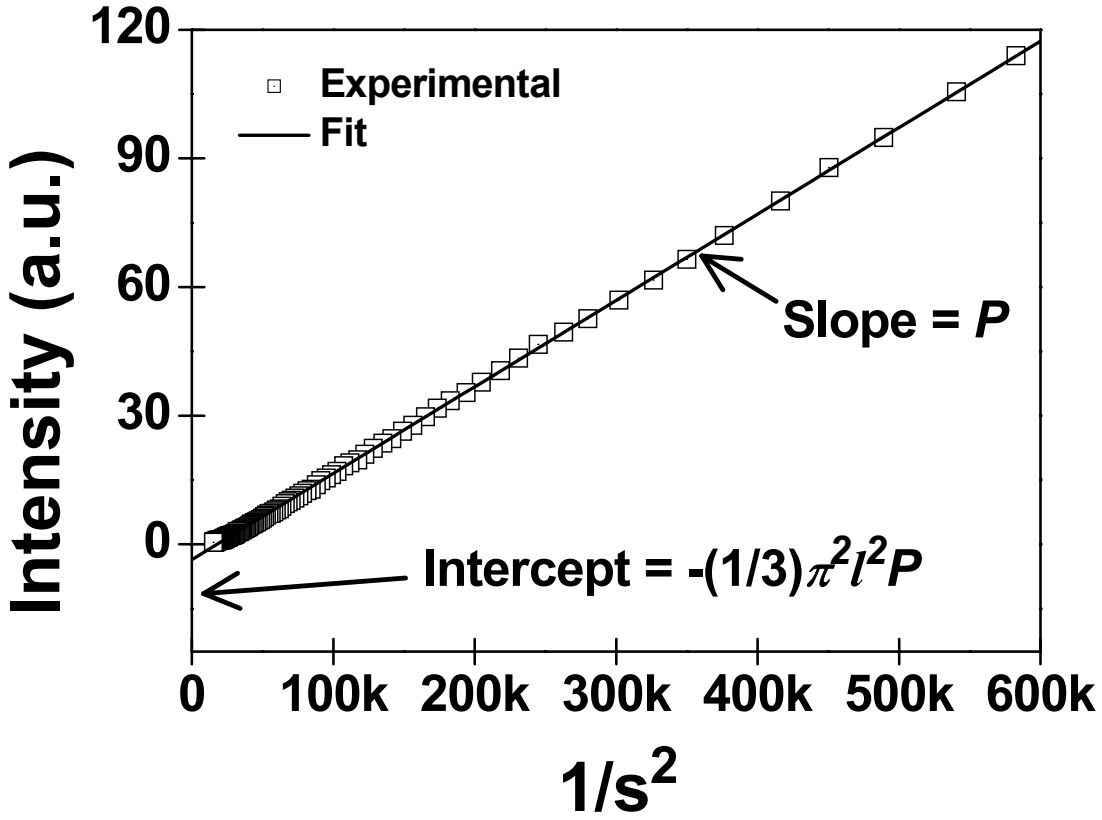
120
90
60
30
0
Intensity (a.u.)
Experimental
Fit
Slope = P
Intercept = -(1/3)π²l²P
0
100k
200k
300k
400k
500k
600k
1/s²

Figure 3.8(a)

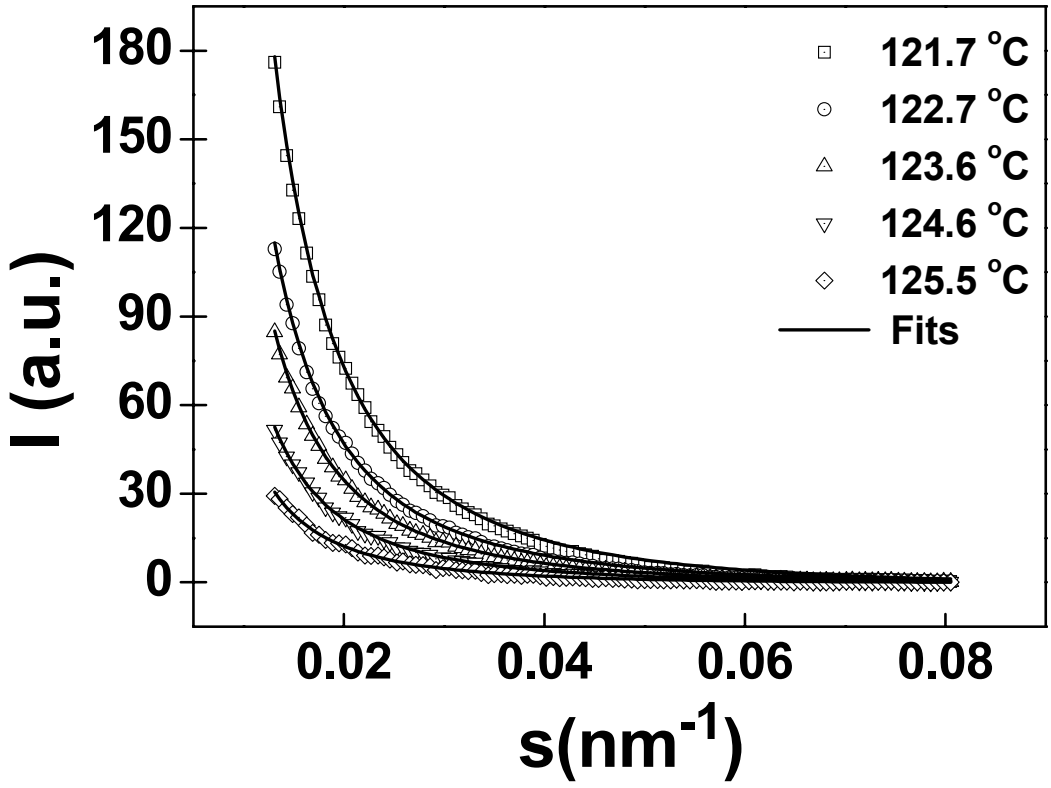
180
150
120
90
60
30
0
I (a.u.)
0.02
0.04
0.06
0.08
s(nm-1)
121.7 °C
122.7 °C
123.6 °C
124.6 °C
125.5 °C
Fits

Figure 3.8(b)

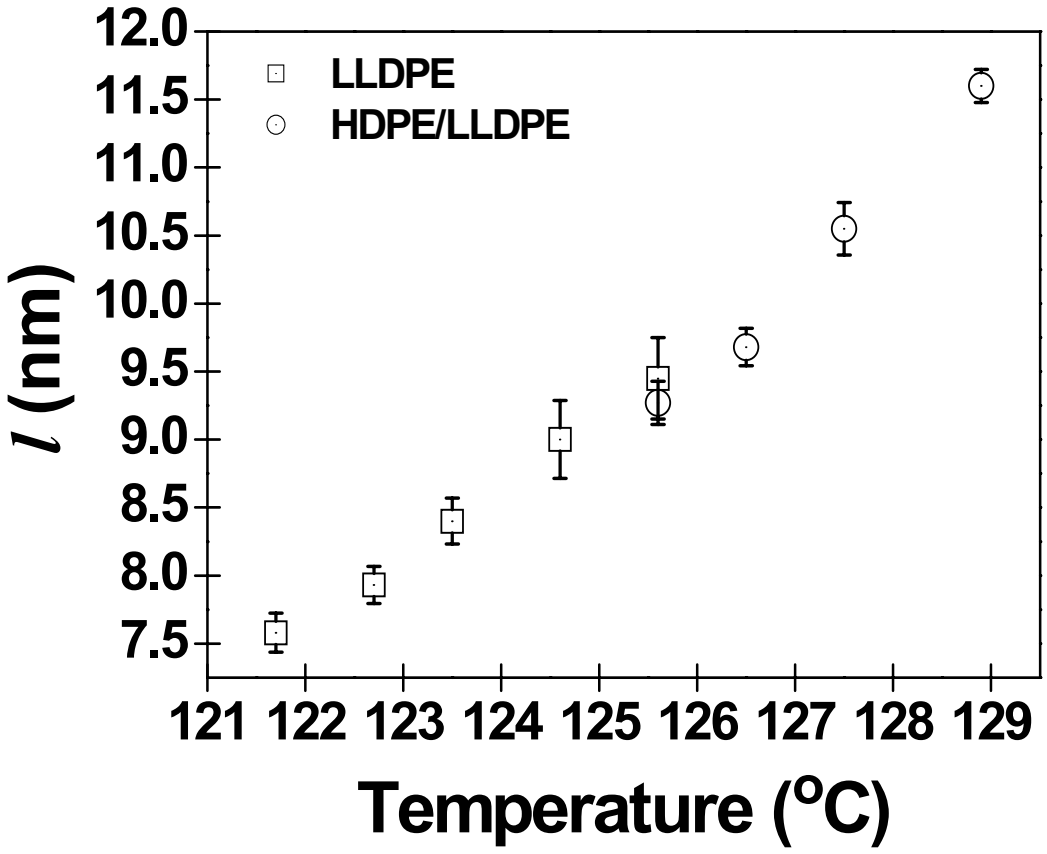
LLDPE
HDPE/LLDPE
l (nm)
12.0
11.5
11.0
10.5
10.0
9.5
9.0
8.5
8.0
7.5
121 122 123 124 125 126 127 128 129
Temperature (°C)

Figure 3.8(c)

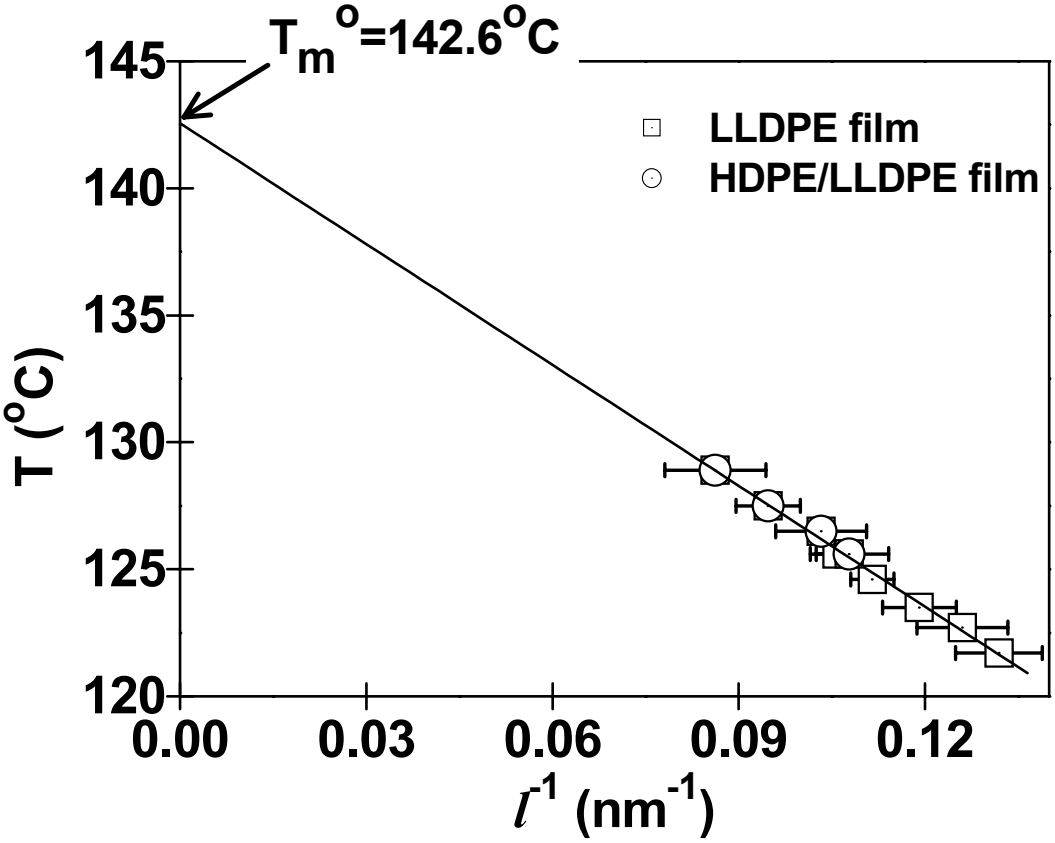
T_m^o=142.6°C
LLDPE film
HDPE/LLDPE film
T (°C)
145
140
135
130
125
120
0.00
0.03
0.06
0.09
0.12
l^{-1} (nm^{-1})

Figure 3.9

Chapter 4. Probing Nucleation and Growth Behavior of Twisted Kebabs from Shish Scaffold in Sheared Polyethylene Melts by In-Situ X-Ray Studies

4.1 Introduction

It has been suggested that the formation of flow-induced shish-kebab structure is intimately associated with the stretch-coil transition of polymer chains in entangled melts, where the long chain species play a much more important role than the short chain species.[1,2] Due to the high entanglement in long chains, two stable conformations (i.e., stretched and coiled) can coexist in segments between the entanglement points after deformation. The stretched-chain conformation can lead to extended-chain crystallization and form shish; the shish structure can subsequently induce folded-chain crystallization of nearby coiled chain segments through an adoption process.[3] Such a mechanism is thought to form the molecular basis for flow-induced shish-kebab formation. Recently, a scanning electron microscopy (SEM) study of the extracted shish-kebab structure from ultra-high molecular weight polyethylene (UHMWPE) in a sheared polyethylene (PE) blend revealed two interesting features of flow-induced precursor structure.[4] (1) The shish structure consisted of several fibrils (so-called 'multiple-shish') instead of a single fibril typically observed in the isolated shish-kebab structure from dilute solutions.[5] (2) The kebab structure showed a single crystal-like layer structure with well defined crystallographic facets and folded chain conformation. In this study, we aimed to deepen our understanding on the nucleation and growth behavior of twisted kebabs from the shish scaffold in the early stages of flow-induced crystallization in polyethylene (PE).

It is well known that in oriented PE samples (e.g. fibers and blown films), kebabs with folded-chain conformation are nucleated from the shish and they subsequently grow into twisted lamellae at the late stages of crystallization.[2,6-10] The lamellar twisting also takes place during spherulite growth from quiescent melts.[12-17] The schematic diagram of a twisted kebab is illustrated in Figure 4.1, where the twisting process leads to rotations of crystallographic *a-axis* and *c*-axis around the *b*-axis in real space, based on an orthorhombic unit cell.[6-8] This phenomenon has been well documented by Keller *et al.*, [2,6] Nagasawa *et al*.[7,8] and Schultz *et al*.[10] In their studies, two scenarios of crystal orientation were presented, depending on the level of the applied stress in flow. Generally, weak flow produces kebabs in the form of twisted ribbons, resulting in off-axis (110) and meridional (200) reflections. This structure is termed the 'Keller/Machin I' mode (or 'row orientation'). Earlier, Lindenmeyer and Lustig also observed a similar structure in tubular film using the pole figure technique; where they termed this orientation as the *a*-axis orientation.[18] In contrast, strong flow often produces kebabs in the 'Keller/Machin II' mode (or the '*c*-axis orientation'), in which the kebabs are flat and the corresponding *c*-axis remains parallel to the flow direction. The characteristic feature of this orientation is the appearance of equatorial (110) and (200) reflections. The Keller/Machin II mode has frequently been observed in HDPE blown films.[9] When the magnitude of flow is in-between the two extremes, an 'intermediate' mode can be generated, resulting in off-axis (200) and (110) reflections. It is thought that since the lateral growth of kebabs is restricted by the adjacent shish-kebab entities, the concentration of shish, which is a strong function of the applied flow, governs the degree of kebab twisting and thus the final orientation mode.

The phenomenon of lamellar twisting in PE crystals has been extensively investigated.[11-17] The origin of the twisting can be attributed to the surface stress resulted from different congestions of the fold surfaces, which was discussed by Lauritzen and Hoffman,[11] Keith and Padden,[12] and Lotz and Cheng.[13] Although the lamellar twisting has been well recognized in the filed of polymer crystallization, the *in-situ* investigation of lamellar twisting, especially during the initial stage of the kebab growth, has never been reported. Some curiosities about the nucleation and growth process of twisted kebabs from the shish scaffold still remain. In chapter 4, we aimed to obtain some new insights into the nucleation and growth behavior of twisted kebabs in sheared HDPE melts to fill this knowledge gap. Specifically, we have carried out 2D rheo-WAXD (wide-angle X-ray diffraction) and rheo-SAXS (small-angle X-ray scattering) measurements after cessation of a step shear. The results were analyzed by a simple shish-kebab model, consisting of central shish and sectorial twisted kebabs, in which each kebab forms sector-like fold surface as it grows outwards and gradually twists (Figure 4.1). In this simple model, when the degree of lamellar twisting is very small, the changes of (110) and (200) reflection patterns are significantly affected by the outer parts of each twisting kebab. This is because the volume of individual kebab would increase as it grow outwards, where the diffraction intensity (I) is proportional to the total crystal volume (V), $I \propto V$.[19,20] In addition, a simplified Avrami equation was applied to examine the nucleation and growth mechanism of the twisted kebabs from the shish scaffold.

4.2 Experimental

The chosen experimental HDPE sample was prepared by the Ziegler-Natta polymerization method. Its number average molecular weight, $\overline{M}_n$, and weight average molecular weight, $\overline{M}_w$, were 18,000 and 57,000 g/mol, respectively. The molecular weight distribution, MWD, of the sample was about 3.2. The sample density at ambient temperature was 0.95 g/cm^3. Synchrotron rheo-WAXD and rheo-SAXS measurements were carried out at the X27C beamline in the National Synchrotron Light Source (NSLS), Brookhaven National Laboratory (BNL). The chosen X-ray wavelength was 1.371 Å. 2D SAXS and WAXD patterns were collected with a MAR CCD detector (MARUSA) having the resolution of 1024×1024 pixels (pixel size = 158.44 μm). The image collection and storage times were 10 and 5 s, respectively. The sample to detector distances for SAXS (1975.6 mm) and WAXD (102.3 mm) were calibrated by AgBe (silver behenate) and Al_2O_3 (aluminum oxide) as the standards. The corrections for background scattering, air scattering, sample absorption and synchrotron beam fluctuation were carried out by using an ion chamber and a pinhole photodiode before and after the sample, respectively.

A modified Linkam shear stage with parallel plates was utilized to perform *in-situ* X-ray measurements. The sample was subject to a step shear at 134 ^oC (near the nominal melting temperature of the HDPE sample) to investigate the earliest event of the shish-kebab formation. Subsequently, the temperature was cooled down to 129 ^oC (at a rate of 1 ^oC/min) to examine the subsequent kebab growth. The chosen shear rates were 70 and 20 s^{-1}, respectively, and the shear duration time was 12 s. HDPE films with about 0.5 mm thickness were prepared by compression molding at 165 ^oC. Samples in the form of a ring (inner and outer diameters were 10 and 20 mm, respectively) were cut from the molded

films for rheo-SAXS or rheo-WAXD measurements. A diamond disc and a Kapton film were used as X-ray windows allowing the passage of X-ray beam. The sample was placed in the gap between the two X-ray windows. Shear flow was applied to the sample by rotating the bottom window, while the top window was maintained stationary. The detailed experimental information has been described before.[21]

4.3 Results and Discussion

4.3.1 Comparisons of rheo-SAXS and rheo-WAXD results

Figure 4.2 shows selected 2D SAXS patterns of the molten HDPE sample at 134 ^{o}C after shear (rate, $\dot{\gamma}$ = 70 s^{-1}, duration, t_s = 12 s) at different times. These patterns clearly exhibited the emergence of equatorial streaks immediately after shear (e.g. pattern at t = 23 s). The feature of equatorial streak in SAXS can be considered as the sign of shish formation (or multiple-shish formation as we speculate, since single shish may not cause the appearance of equtorial streak[4]) alligned parallel to the flow axis. The meridional maxima emerged afterwards, as seen in the SAXS pattern at t = 38 s. These meridional scattering peaks indicacte the development of layered kebabs aligned perpendicularly to the flow direction. Although the SAXS results indicated that the evolution of the kebab assembly (leading to the lamellar stack) followed the asymptioc growth behavior, they did not provide insight into the growth mechanism of twisted kebabs.

The changes of the scattered intensity from shish (i.e., from equatorial streak) and kebabs (i.e., from meridional peaks), extracted from the 2D SAXS patterns in Figure 4.2, are depicted as a function of time in Figure 4.3. It was seen that shish appeared immediately upon the cessation of shear. During the entire crystallization process, the shish intensity, I_{Shish}, remained about constant. However, the kebab intensity, I_{Kebab}, exhibited a rapid increase. Since no crystallization was observed in the quiescent state at 134 ^{o}C (data not shown), the developments of shish and kebabs were mainly resulted from the influence of flow. The flow-induced shish formation can be explained from both thermodynamical and kinetic viewpoints. Thermodynamically, as stretched (extended) chains lead to reduced entropy, the corresponding free energy barrier for nucleation becomes less to overcome, thus easing the process of shish formation. Kinetically, since the extended chain conformation is close to the chain conformation in the crystalline state, stretched chains encounter a less kinetics barrier to crystallize than that of the coiled state. As a result, extended chain conformation would increase the rate of shish formation. The existence of stable shish can enable the nucleation and growth of kebabs through processes of chain diffusion and adsorption.[22]

Selected 2D WAXD patterns collected during crystallization at 134 ^{o}C in the sheared HDPE melt ($\dot{\gamma}$ = 70 s^{-1}, t_s = 12 s) and corresponding azimuthal profiles at the (110) reflection position are shown in Figures 4.4(a) and 4.4(b), respectively. The (110) azimuthal profiles were obtained using the following procedures, assuming that the sheared sample had a fiber symmetry.[23] To properly consider the (110) reflection in undistorted reciprocal space along the scattering vector ($s = 2\sin\theta/\lambda$, where θ is the half of diffraction angle and λ is the beam wavelength) and the azimuthal angle (ϕ), the measured intensity from the flat-plate detector, $I(s,\phi)$, was first corrected by a geometric

factor, $s \cdot \sin\phi$ (we note that the 2D WAXD images in Figure 4.4(a) were not corrected, but the azimuthal profiles in Figure 4.4(b) were corrected; the flow axis was defined as the reference axis). In Figure 4.4(a), the initial diffraction profile (e.g. t = 98 s) exhibited a pair of faint but highly oriented line-like (110) reflections on the equator, implying that both *a*-axis and *b*-axis were normal to the flow direction. Such a pattern is consistent with the formation of crystalline shish, having *c*-axis parallel to flow axis. As crystallization proceeded, the equatorial 2-arc (110) reflections were broadened azimuthally (e.g. t = 128 s) and then transformed into off-axis 4-arc pattern (e.g. thin arrows at t = 263 s in Figure 4.4(a)), together with the appearance of off-axis 4-arc (200) reflections. Here, it should be noted that the amount of shish might be overestimated because the equatorial (110) intensity could also contain a fraction of kebabs formed at the early stages.

The transformation of the (110) reflection can be better examined in Figure 4.4(b). In this figure, the total integrated intensity of (110) reflection was determined as $2\pi\int_{\min}^{\max} s \cdot ds \int_0^{\pi/2} \sin\phi d\phi I(s,\phi)$, where min and max represent the positions of the lowest and highest ends of the (110) crystalline peak. It was seen that the (110) reflection appeared on the equator ($\phi \approx 90^o$, marked by a vertical arrow) at early stages (t < 98 s), but this reflection began to broaden azimuthally with increasing time (e.g. at t = 128 s) and eventually split into two peaks ($\phi \approx 70^o$ and 110^o, marked by two tilted arrows) at late stages (t > 263 s). The vertical arrow mark at $\phi \approx 90^o$ represents the development of the shish; the tilted arrow mark pointing the (110) reflection splitting indicates the twisting of kebabs (e.g. at t = 263 s). The initial azimuthal broadening at the equator and then the off-axis splitting of the (110) reflection clearly revealed the evolution of kebab twisting. It is clear that as kebabs grows outwards and becomes twisted, the *a*-axis rotates around the *b*-

axis in real space, resulting in the rotation of reciprocal vector for the (110) plane, $\vec{r}^{*}_{110}$. Thus, it is thought that the initially broadening of the equatorial (110) reflection can be associated with the Keller/Machin II mode, where the off-axis appearance of (110) and (200) reflections is due to the incomplete twisting of kebabs (i.e., the intermediate mode).

Using Gaussian functions, the azimuthal intensity profile of the (110) reflection in Figure 4.4(b) could be curve-fitted to estimate the crystallization contributions from shish (peak at $\phi \approx 90^{o}$) and kebabs (peaks at $\phi \approx 70^{o}$ and 110^{o}), respectively. The results are illustrated in Figure 4.4(c). In this figure, the intensity of the equatorial (110) reflection (from shish) was found to increase initially, but reached a plateau value after t = 98 s. In contrast, the intensity of the off-axis (110) reflection (from twisted kebabs) increased almost linearly with time, indicating the continuous development of crystallinity.

After shear-induced crystallization at 134 ^{o}C for 45 min, further kebab growth was induced by cooling of the sample from 134 ^{o}C to 129 ^{o}C at 1 ^{o}C/min rate. The resulting degrees of crystallinity at 134 ^{o}C to 129 ^{o}C were about 2 % and 10 %, respectively. Selected 2D WAXD patterns collected during cooling is shown in Figure 4.5. It was seen that the displacement angle of the off-axis (200) reflection gradually increased with decreasing temperature and the corresponding 4-arc pattern was transformed into a broad 2-arc pattern with (200) reflections aligned on the meridian. The observed phenomena imply change of orientation from the intermediate mode to the Keller/Machin I mode due to the further twisting of kebabs. Since the crystallinity was very low (2 %) at 134 ^{o}C the shish-kebab entities were somewhat isolated without notable intra-shish-kebab impingement, where further kebab twisting was permitted.

Figure 4.6 shows selected time-resolved 2D WAXD patterns of the sheared HDPE melt collected at 129°C. In this experiment, the sample was initially sheared at 134 °C ($\dot{\gamma}$ = 20 s^{-1}, t_s = 12 s) and then subsequently held for 45 min. Afterwards, the temperature was cooled to 129 °C at 1°C/min. Different from the previous results at a higher shear rate ($\dot{\gamma}$ = 70 s^{-1}, t_s = 12 s), no apparent crystallization in WAXD was observed during cooling. In addition, no equatorial streak in corresponding SAXS was seen (data not shown). However, when the temperature decreased to 129 °C, the WAXD patterns clearly developed distinct off-axis 4-arc (110) reflections at t = 15 s and then off-axis 4-arc (200) reflections at t = 30 s, respectively. This observation indicates the 2D growth of twisted kebabs, similar to that after the application of shear at a shear higher rate (70 s^{-1}). The above results are consistent with Keller's hypothesis of critical orientation molecular weight, M^* [24] as well as our results in an earlier study.[21] In brief, in a sheared polymer melt with polydispersity at a given temperature, only the chains longer than M^* can remain stretched and oriented after deformation, while the shorter chains would quickly relax back and return to the random coil state. The increase in the shear rate would decrease the value of M^* and increase the fraction of stretched chains. This hypothesis agrees well with the results after 70 s^{-1} shear at 134°C, where a pair of equatorial line-like (110) reflections in WAXD and an equatorial scattering streak in SAXS were seen. The appearances of equatorial (110) reflections in WAXD and equatorial streak in SAXS clearly indicate the shish formation. However, the absence of equatorial (110) reflection (Figure 4.6) and equatorial scattering streak (data not shown) after the application of a lower shear rate (20 s^{-1}) at 134 °C does not necessarily indicate the absence of shish; instead it may suggest that the flow-induced shish scaffold is too weak or too dilute to be detected X-rays. Without question, this weak shish scaffold is

still effective to induce kebabs at lower temperatures, as evidenced by the the appearance of arc-like off-axis (110) and (200) reflections at 129 ^{o}C. Since the shish density is smaller at lower shear rates, the twisting of kebabs would be more prominent, which is consistent with the above finding.

It is noted that the transformations of (110) reflection from equatorial to off-axis and of (200) reflection from off-axis to meridian can be explained by the volume change of the individual twisting kebab (V_i), which is a function of the distance from the nucleating center (d). If one considers that the individual kebab at the initial stages prior to any physical limit can be simplified by a narrow ribbon (lamella), and the twisted kebab can branch into a multitude and fill the sectorial space, the relationship $V_i(d) \propto d$ should hold. However, if the physical limit is imposed (e.g. due to the concentration gradient effect), the dimension of the lamella would decrease by forming rounded growth fronts and the above relationship would not be valid. Hence, a question can be raised if the occurrence of twisted ribbon and its random branching are the only choices for the space filling process before the physical limit is reached. We believe this is the case and the following scenario is likely to occur. Based on ample microscopic evidences, one can consider that the individual kebab at the initial stages is sectorized. For example, in hexagonal shape PE single crystal, its lateral growth often exhibited sectorial habits[25]; the solvent extracted melt-crystallized shish-kebabs[4] and solution grown shish-kebabs[2] also showed the circular (or hexagonal) shape kebab morphology. The sectorial kebab can be readily twisted and then branch into a multitude and fill the space. In this scenario, the relationship, $V_i(d) \propto d^2$, can be justified.

4.3.2 The growth behavior of twisted kebabs in entangled melts

In order to investigate the nucleation and growth behavior of twisted kebabs, a simplified Avrami analysis was used to analyze the above results. The conventional Avrami equation can be expressed as[26]

$$v_c(t) = 1 - \exp(-Kt^n) \tag{1}$$

where $v_c(t)$ is the volume fraction of crystals at different time (t), n is the Avrami exponent and K is the Avrami constant. In semi-crystalline polymers, since the volume fraction of crystals behind the growth front is always less than 1, the Avrami equation is often modified as[25]

$$\frac{v_c(t)}{v_\infty} = 1 - \exp(-Kt^n) \tag{2}$$

where v_∞ is the volume fraction of crystals at time infinity (∞). In the current X-ray diffraction study, the following two relationships can be assumed: (1) $v_c(t)/v_\infty$ (where $v_c(t)/v_\infty \propto$ the crystal volume $V(t)$) $\propto I_c(t)/I_\infty$ (where $I_c(t)/I_\infty \propto I_c(t)$), and (2) $\exp(-Kt^n) \approx 1-Kt^n+\cdots$, where $I_c(t)$ and I_∞ are crystal reflection intensities at time (t), and infinity (∞), respectively. The Avrami equation thus becomes

$$I_c(t) \propto Kt^n \tag{3}$$

This equation indicates that during crystallization, the change in the crystal diffraction intensity as a function of time should follow a power law with an Avrami exponent (n) at the early stages of crystallization, where t is small. Such an expression should be valid at the initial stage of crystallization, but would fail at the later stage due to some physical limits such as impingements and loss of crystallizable chains.

Figure 4.7 shows the relationship between the logarithmic integrated (110) intensity for only kebabs as a function of logarithmic time as well as the Avrami fits

using Equation 3 at the early stages of crystallization under two different crystallization conditions (i.e., crystallization at 134 ^{o}C immediately after shear ($\dot{\gamma}$ = 70 s^{-1}, t_s = 12 s) and at 129 ^{o}C after cooling from 134 ^{o}C (the sample was first sheared at 134 ^{o}C; $\dot{\gamma}$ = 20 s^{-1}, t_s = 12 s)). The fitted Avrami exponents *n*'s for both processes were found to be about 3. This suggests that the growth of twisted kebabs can either possess the 2D geometry under thermal (sporadic) nucleation or the 3D geometry under athermal (instantaneous) nucleation (Table 4.1). In order to determine the probable nucleation type, i.e., thermal *versus* athermal nucleation, the change in long period of the layered kebabs was also examined from the SAXS data. Under the assumption of isolated shish-kebabs structure (i.e., without the inter-shish-kebab impingement) at the initial stages, the nucleation of kebabs should be thermal if the lamellar long period decreases as a function of time; whereas the nucleation should be athermal if the long period is constant. The changes of long period for both crystallization conditions are illustrated in Figure 4.8. It was found that both long periods decreased rapidly with time at the initial crystallization stage. This suggests that the nucleation process for kebabs is mainly thermal (sporadic) with 2D growth geometry, initiated from the surface of shish. It is imperative to point out that the Avrami analysis cannot distinguish the different modes of kebab growth, e.g. circular, sectorial and kebab branching.

Some insightful information about the growth of twisted kebabs was obtained by examining the change of displacement angle for the (110) reflection of kebabs with respect to the equator and the corresponding evolution of the (110) intensity. The results for crystallization at 134 ^{o}C after shear ($\dot{\gamma}$ = 70 s^{-1}, t_s = 12 s) and at 129^{o}C after shear at 134^{o}C ($\dot{\gamma}$ = 20 s^{-1}, t_s = 12 s) are shown in Figures 4.9(a) and 4.9(b), respectively. As mentioned earlier, no crystallization was observed at 134 ^{o}C after shear at $\dot{\gamma}$ = 20 s^{-1}. In

Figure 4.9(a), the displacement angle of (110) reflection at 134 ^{o}C was found to increase at two different rates: a sharp increase in the initial stage and a very slow increase (eventually reaching a plateau value) at t > 600 s. It is interesting to note that the displacement angle (twisting angle) of the (110) reflection increased only slightly at t > 600 s, but the corresponding increase in the (110) intensity was quite notable. This indicates that the volume of kebabs increased rather fast, even when the change in the lateral dimension of kebabs slowed down at t > 600 s. This would be consistent with the 2D growth of twisted kebabs, where $V_i(d) \propto d^2$. In Figure 4.9(b), the displacement angle of (110) reflection exhibited a maximum value at t = 113 s. The decrease in the displacement angle during twisted kebab growth indicates that the twisting angle of kebabs became higher than 90^{o} after t = 113s. This observation again confirms that a lower shish density was generated at a lower shear rate ($\dot{\gamma}$ = 20 s^{-1}), in which the kebab twisting became more prominant.

The shish-kebab structure illustrated in Figure 4.1 contains a single shish and a single twisted sectorial kebab, but this simple structure can effectively explain our X-ray diffraction results (i.e., 4-arc (110) reflections at the off-axis and 2-arc (200) reflections on the meridian). For instance, the kebab in this structure has only one rotation axis (*b*-axis) and is only moderately twisted without large extension. But this structure can be extrapolated to all directions perpendicular to the shish axis and to large extension and twisting as long as the physical limits such as the loss of crystallizable chains and the steric conflicts between the shish-kebabs entities are not concerned. A calculated 2D WAXD pattern from such a simple shish-kebab model with fiber symmetry, where the twisting angle of kebabs is “infinite” or very large such that the orientations of *a* and *c* crystallographic axes are randomized around the b-axis, is shown in Figure 4.10. The

calculated pattern exhibits 4-arc (110) reflections at the off-axis and 2-arc (200) reflections on the meridian, which is consistent with the 'Keller/Machin I' mode proposed by Keller *et al.*[2]

4.4 Conclusions

By utilizing synchrotron rheo-WAXD and -SAXS techniques, the nucleation and growth behavior of twisted kebabs from shear-induced shish scaffold in entangled HDPE melts was examined. Under strong shear (e.g. $\dot{\gamma}$ = 70 s^{-1}, t_s = 12 s) at 134^{o}C, distinct orientation changes of twisted kebabs from 'Keller/Machin II' to 'intermediate' and finally to 'Keller/Machin I' modes were seen. Under a relatively weak shear field ($\dot{\gamma}$=20 s^{-1} and t_s = 12 s) at 134 ^{o}C, although no apparent shish was detected first, the subsequent kebab growth at 129 ^{o}C also exhibited orientation changes from 'intermediate' to 'Keller/Machin I' modes. The lower shear rate generates a lower shish density, which enhances the kebab twisting. The integrated (110) diffraction intensity of kebabs in WAXD developed at the early stages of crystallization could be described by a simplified Avrami equation, $I(s,\phi) \propto kt^n$ with $n \approx 3$, where the corresponding long period of kebabs in SAXS was found to decrease with time. The combined SAXS/WAXD results were consistent with the 2D growth of sectorial kebab under thermal (sporadic) nucleation.

4.5 References

1. Keller, A., Odell, J. A. *Colloid. Polym. Sci.* **1985**; 263: 181.

2. Keller, A., Kolnaar, J. W. H. *Prog Colloid. Polym. Sci.* **1993**; 92: 81.

3. Loos, J., Katzenberg, F., Petermann, J. *J. Mat. Sci.* **1997**; 32: 1551.

4. Hsiao, B. S., Yang, L., Somani, R. H., Avila-Orta, C. A., Zhu, L. *Phys. Rev. Lett.* **2005**; 94: 117802.4.

5. Perterlin, A. *Pure Appl. Chem*. **1966**; 12: 563.

6. Keller, A., Machin, M. J. *J. Macromol. Sci. Phys*. **1967**; B1 (1): 41.

7. Nagasawa, T., Matsumura, T., Hoshino, S. *Appl. Polym. Symp.* **1973**; 20: 295.

8. Nagasawa, T., Matsumura, T., Hoshino, S. *Appl. Polym. Symp.* **1973**; 20: 275.

9. Lu, J., Sue, H. J. *Macromolecules* **2001**; 34: 2015.

10. Nadkarni, V. M., Schultz, J. M. *J. Polym. Sci. Phys. Ed.* **1977**; 15: 2151.

11. Hoffman, J. D., Lauritzen Jr, J. I. *J. Res. Nat. Bur. Stand*. *(US)* **1961**; 65A: 297.

12. Keith, H. D., Padden, F. J. *Polymer* **1984**; 25: 8.

13. Lotz, B., Cheng, S. Z. D. *Polymer* **2005**; 46: 577.

14. Bassett, D. C., Hodge, A. M. *Polymer* **1978**; 19: 469.

15. Bassett, D. C., Hodge, A. M. *Proc. R. Soc. Lond.* **1981**; A377: 61.

16. Bassett, D. C., Hodge, A. M. Proc. *R. Soc. Lond.* **1979**; A359: 121.

17. Schultz, J. M. *Polymer* **2003**; 44: 433.

18. Lindenmeyer, P. H., Lustig, S. *J. Appl. Polym. Sci*. **1965**; 9 : 227.

19. Guinier, A. *X-ray Diffraction*, W. H. Freeman and Company; San Francisco and London; **1963**.

20. Roe, R. J. *Methods of X-ray and Neutron scattering in Polymer Science*, Oxford University Press; New York; **2000**.

21. Somani, R. H., Hsiao, B. S., Nogales, A., Srinivas, S., Tsou, A. H., Sics, I., Balta-Calleja, F. J., Ezquerra, T. A. *Macromolecules* **2000**; 33: 9385.

22. Dukovski, I., Muthukumar, M. *J. Chem. Phys.* **2003**; 118: 6648.

23. Fraser, R. D. B., Macrae, T. P., Miller, A., Rowlands, R. J. *J. Appl. Cryst.* **1976**; 9: 81.

24. Keller, A., Kolnaar, H. W. *Mater. Sci. Technol*. **1997**; 18: 189

25. Gedde, U. W. *Polymer Physics*, Chapman & Hall; New York; **1995**.

26. Avrami, M. *J. Chem. Phys*. **1939**; 7:1103.

Table 4.1

Growth Geometry	Nucleation	
	Athermal	Thermal
Linear	1	2
Two-dimensional (2D)	2	3
Three-dimensional (3D)	3	4

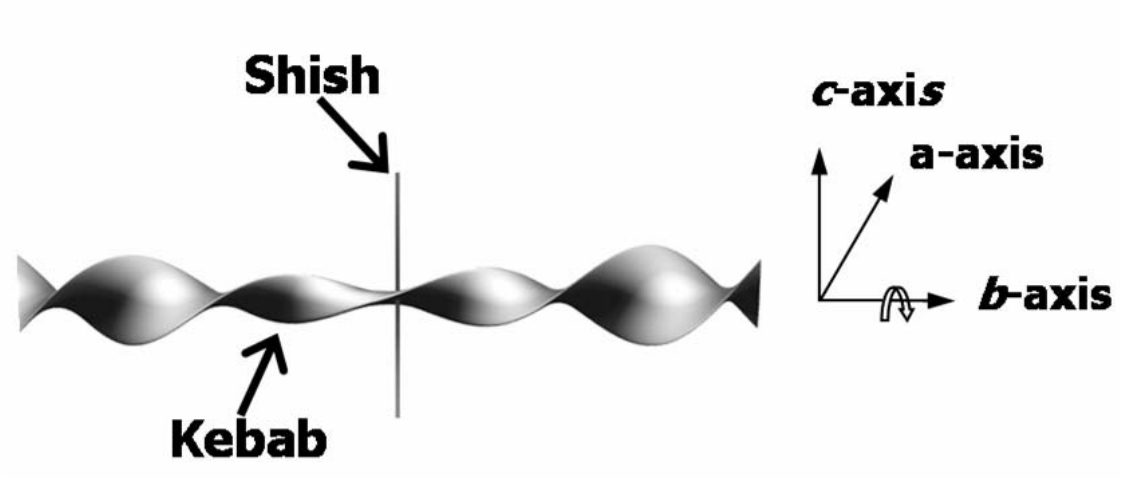

Figure 4.1

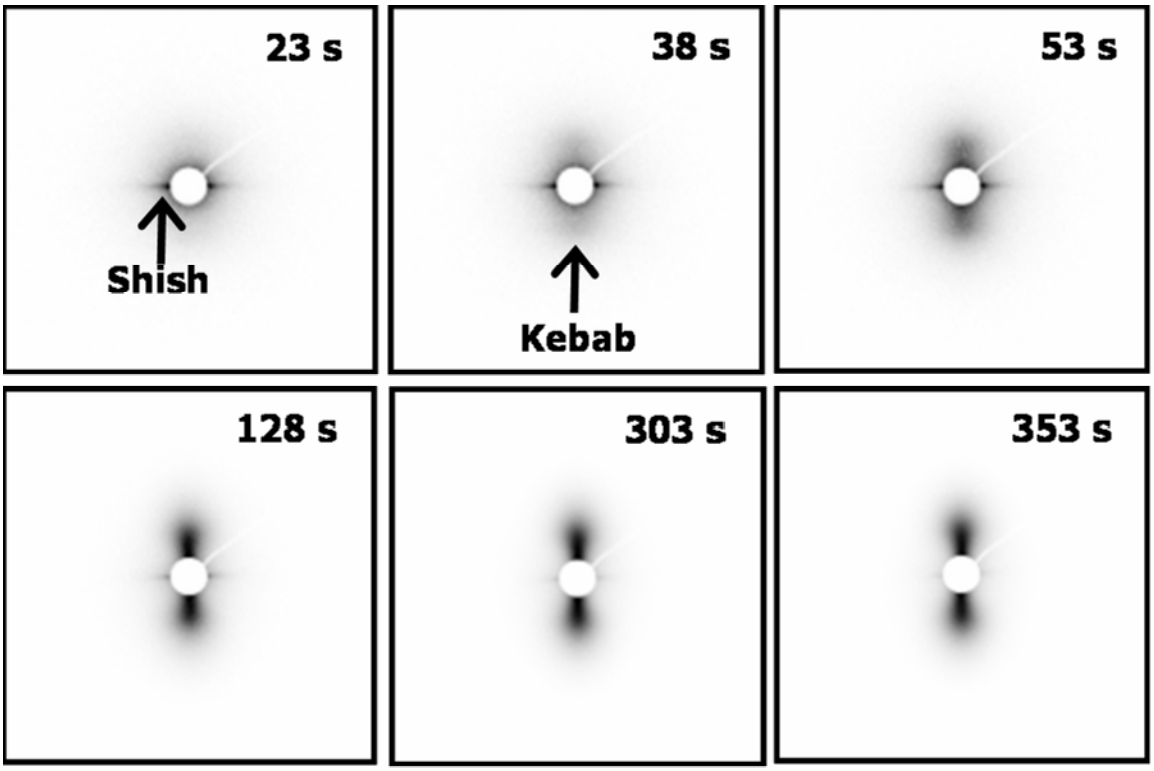

Figure 4.2

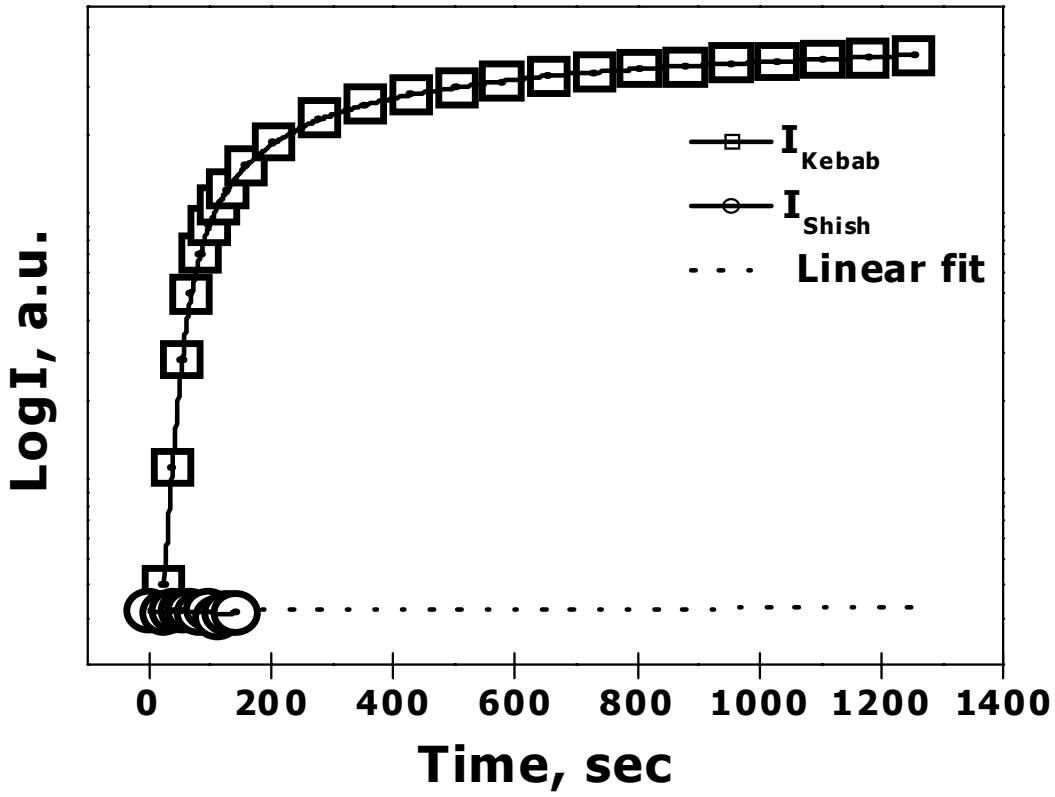
LogI, a.u.
Time, sec
0
200
400
600
800
1000
1200
1400
I Kebab
I Shish
Linear fit

Figure 4.3

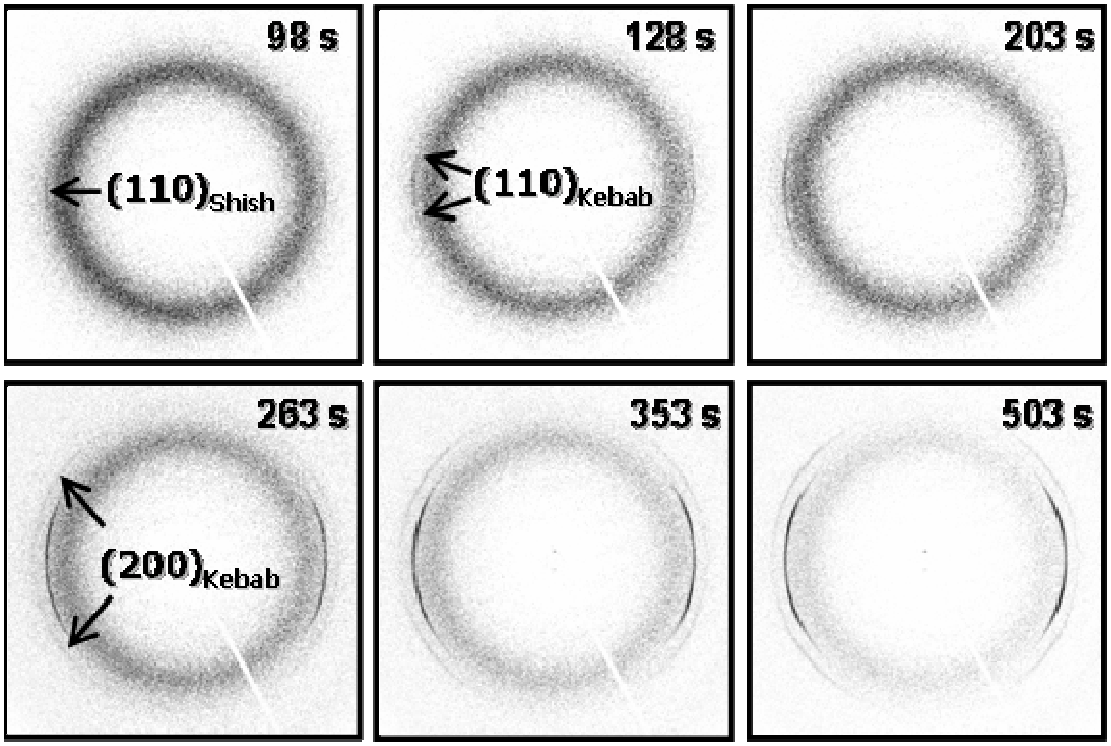

Figure 4.4(a)

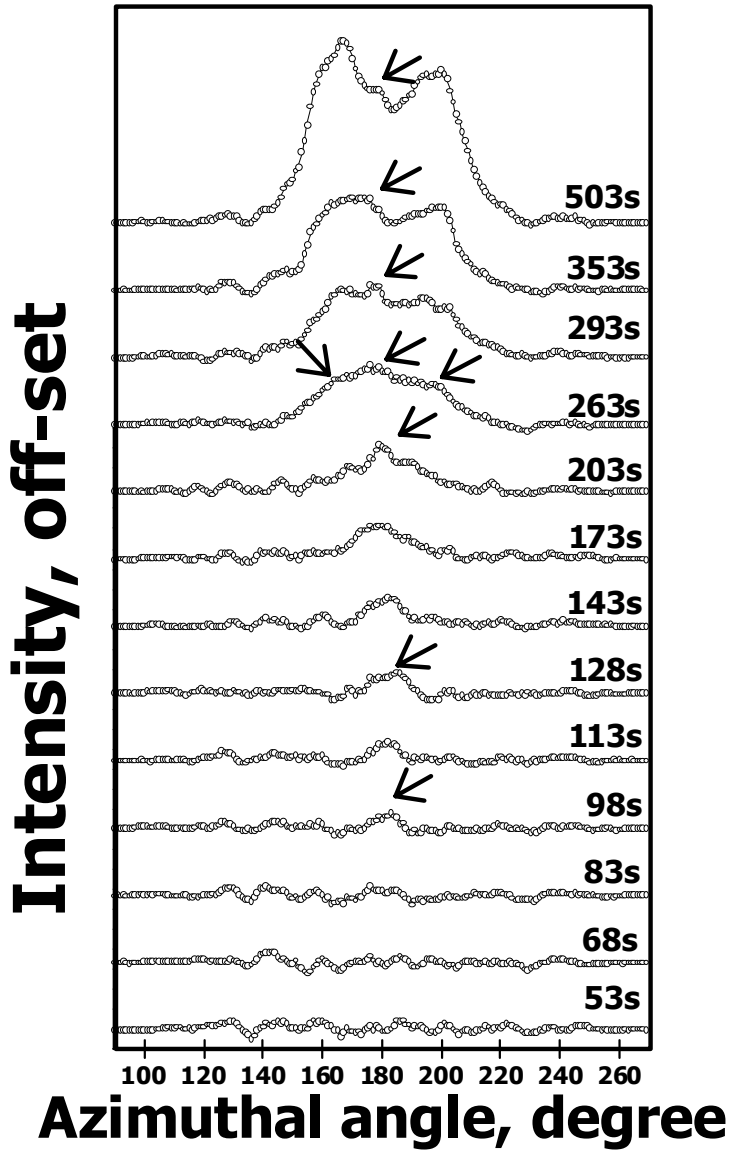
Intensity, off-set
503s
353s
293s
263s
203s
173s
143s
128s
113s
98s
83s
68s
53s
100 120 140 160 180 200 220 240 260
Azimuthal angle, degree

Figure 4.4(b)

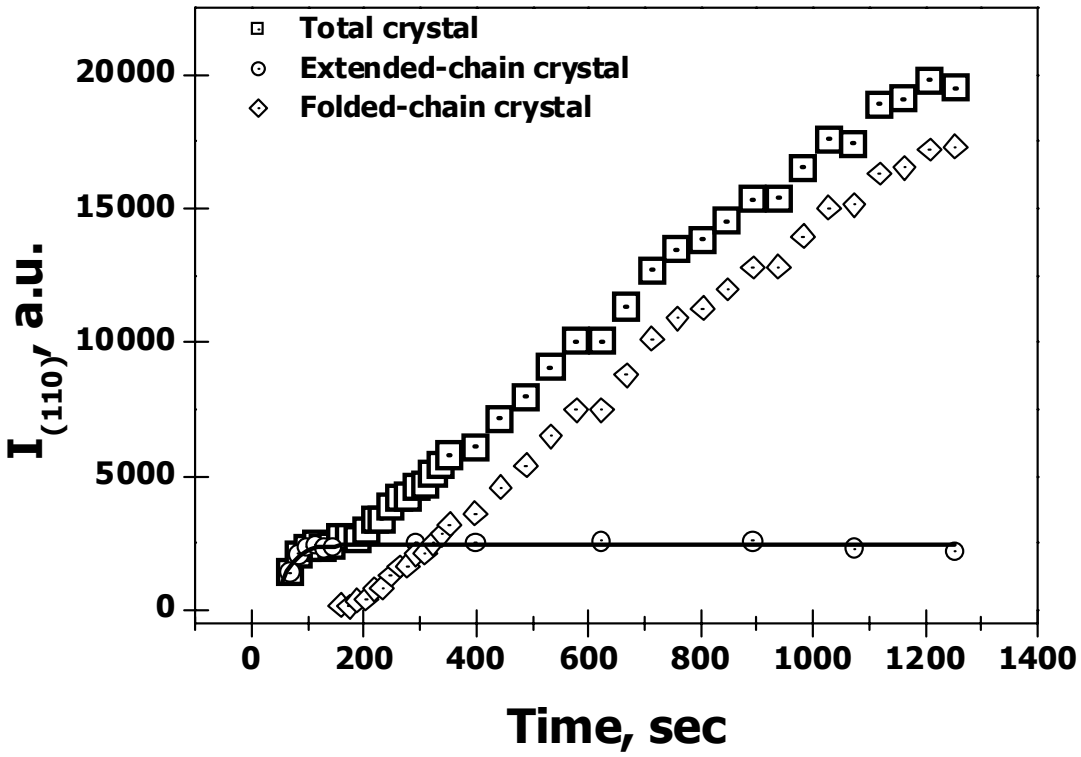
Total crystal
Extended-chain crystal
Folded-chain crystal
20000
15000
10000
5000
0
$I_{(110)}$, a.u.
0
200
400
600
800
1000
1200
1400
Time, sec

Figure 4.4(c)

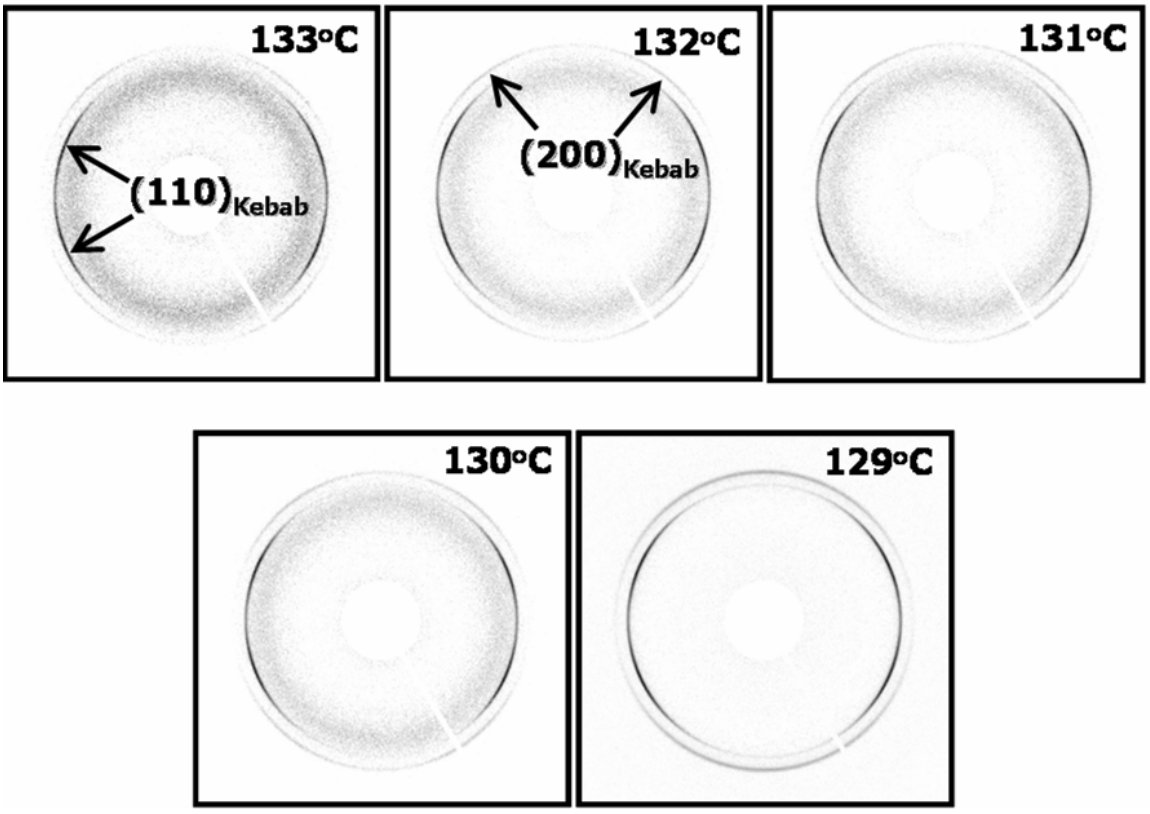

Figure 4.5

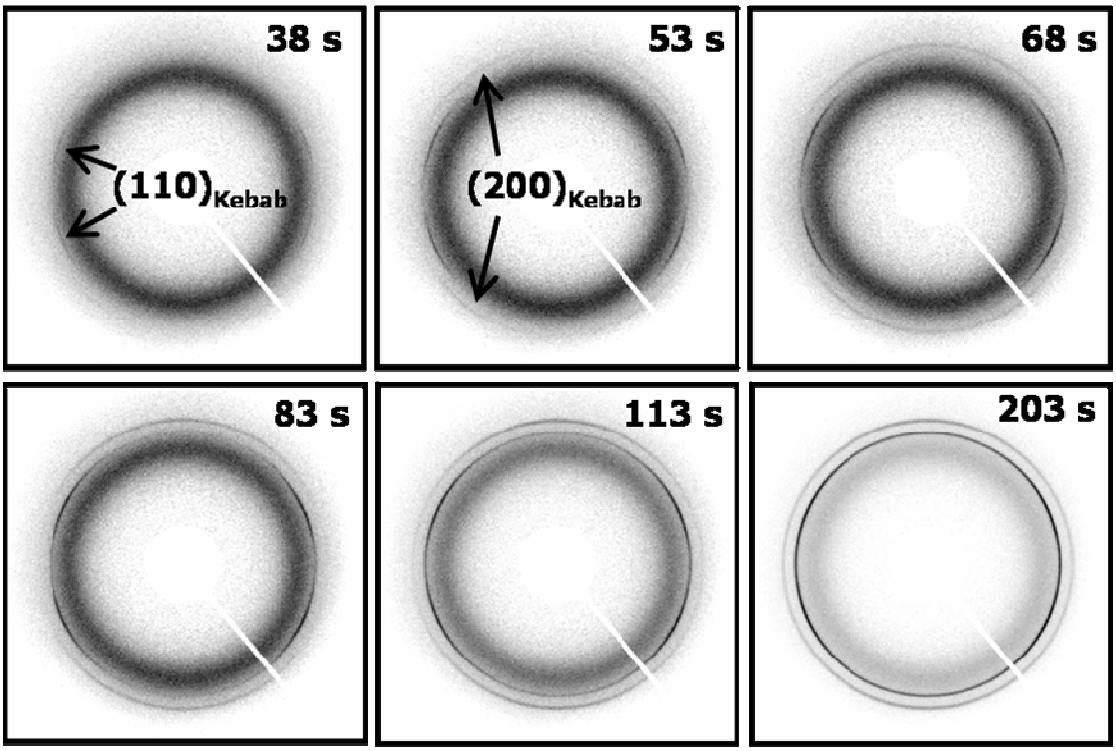

Figure 4.6

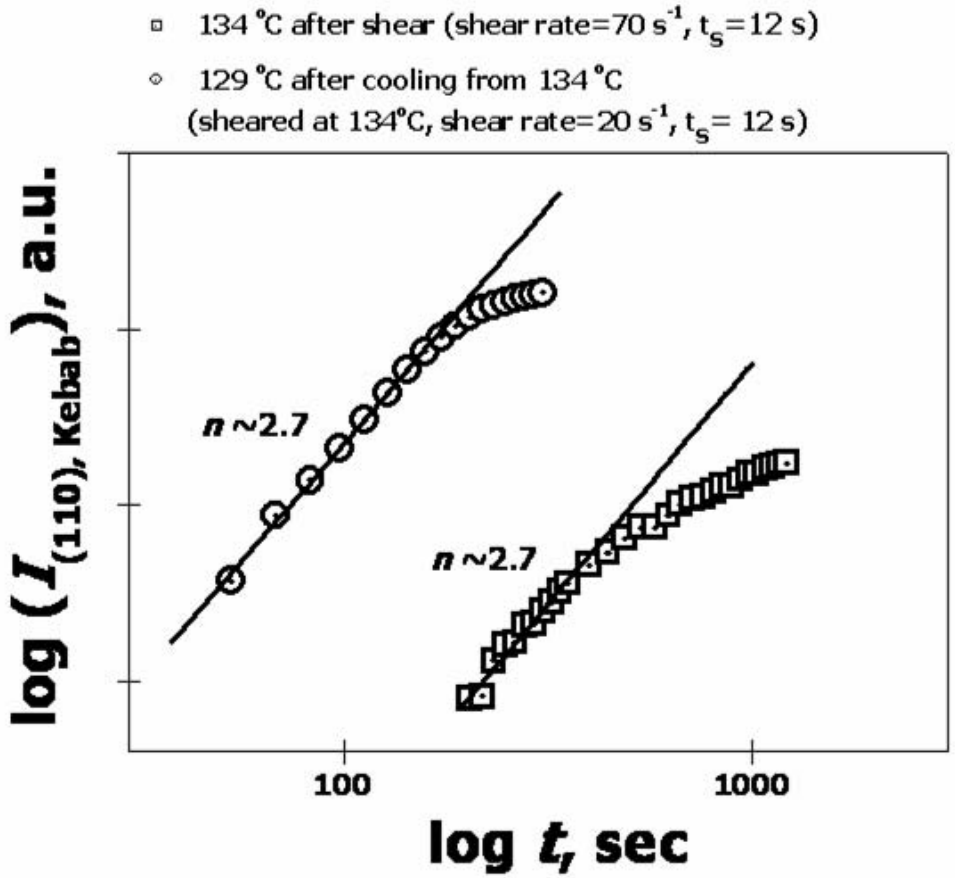
134 °C after shear (shear rate=70 s-1, ts=12 s)
129 °C after cooling from 134 °C
(sheared at 134°C, shear rate=20 s-1, ts= 12 s)
log (I(110), Kebab), a.u.
n ~2.7
n ~2.7
100
1000
log t, sec

Figure 4.7

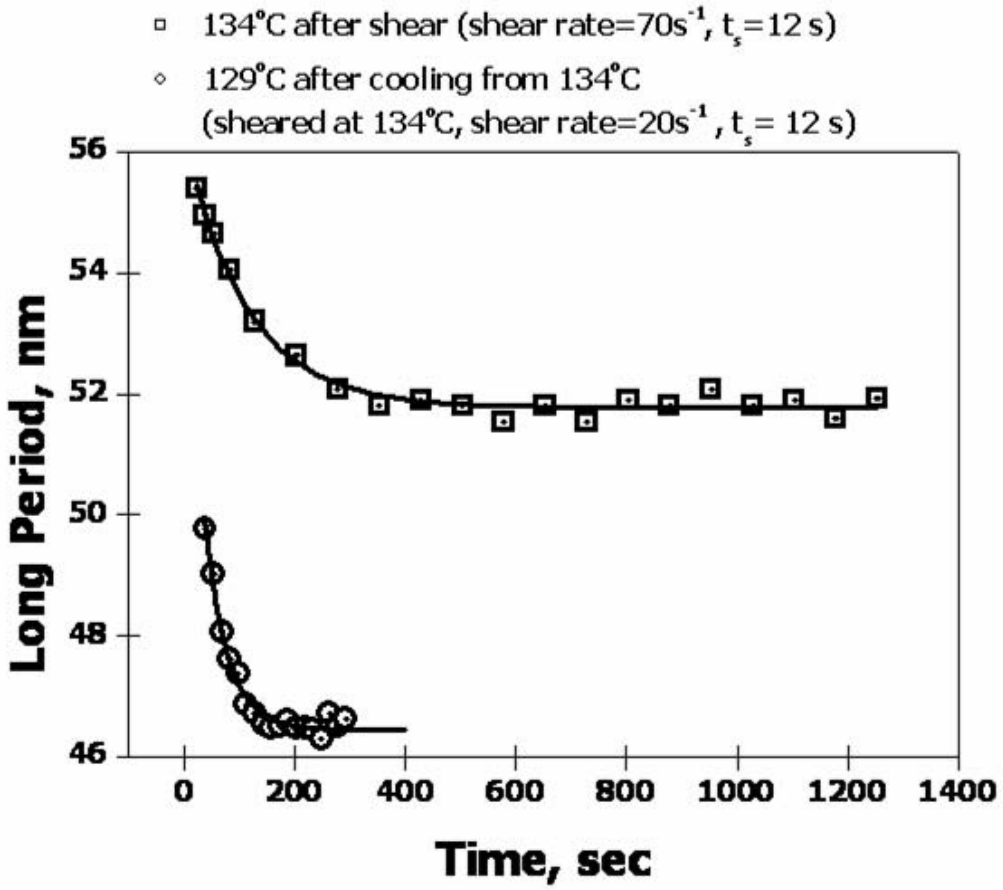
134°C after shear (shear rate=70s-1, ts=12 s)
129°C after cooling from 134°C
(sheared at 134°C, shear rate=20s-1, ts= 12 s)
Long Period, nm
56
54
52
50
48
46
0
200
400
600
800
1000
1200
1400
Time, sec

Figure 4.8

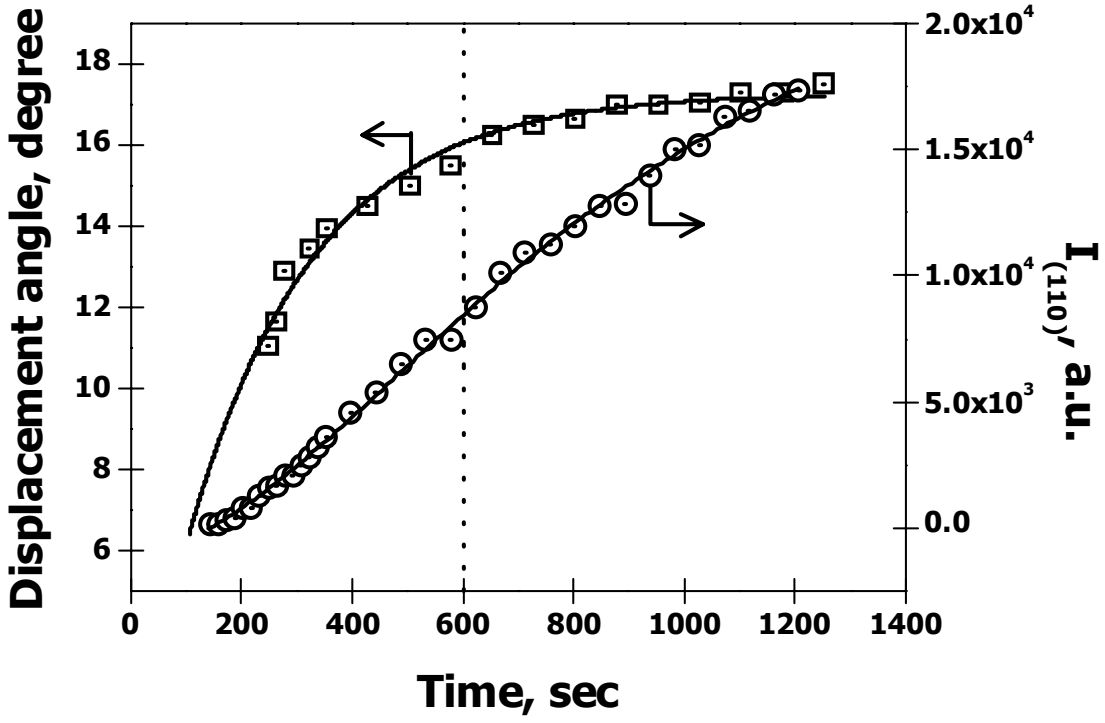
Displacement angle, degree
18
16
14
12
10
8
6
0
200
400
600
800
1000
1200
1400
Time, sec
2.0x10^4
1.5x10^4
1.0x10^4
5.0x10^3
0.0
I(110), a.u.

Figure 4.9(a)

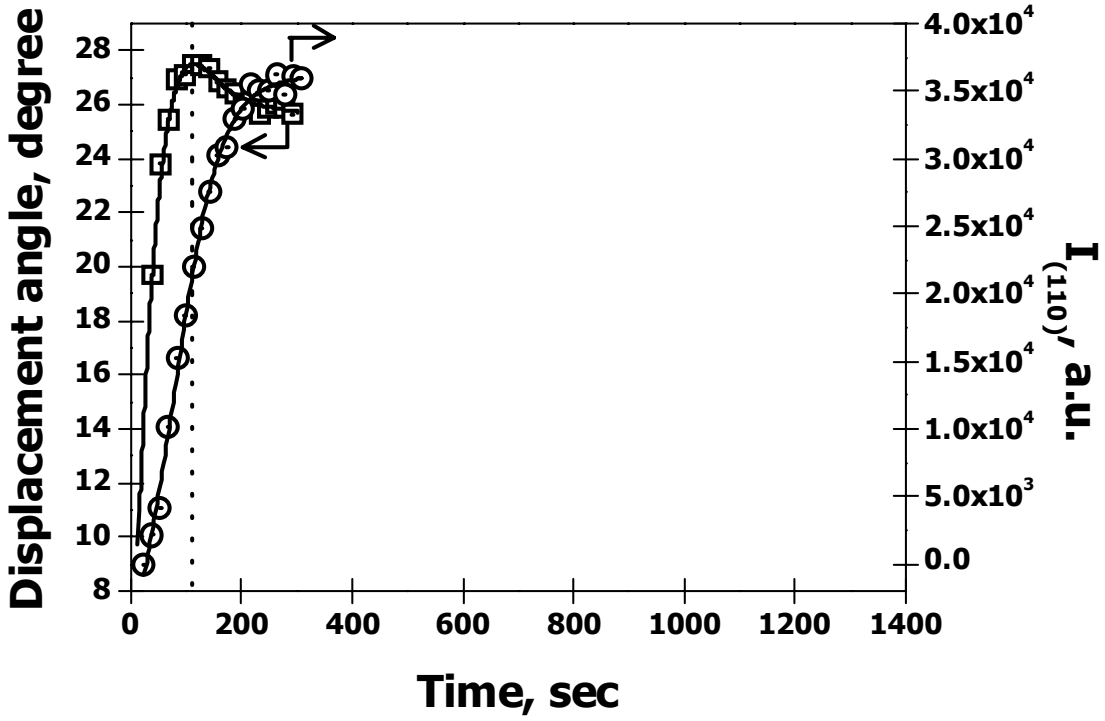
Displacement angle, degree
28
26
24
22
20
18
16
14
12
10
8
0
200
400
600
800
1000
1200
1400
Time, sec
4.0x10^4
3.5x10^4
3.0x10^4
2.5x10^4
2.0x10^4
1.5x10^4
1.0x10^4
5.0x10^3
0.0
I(110), a.u.

Figure 4.9(b)

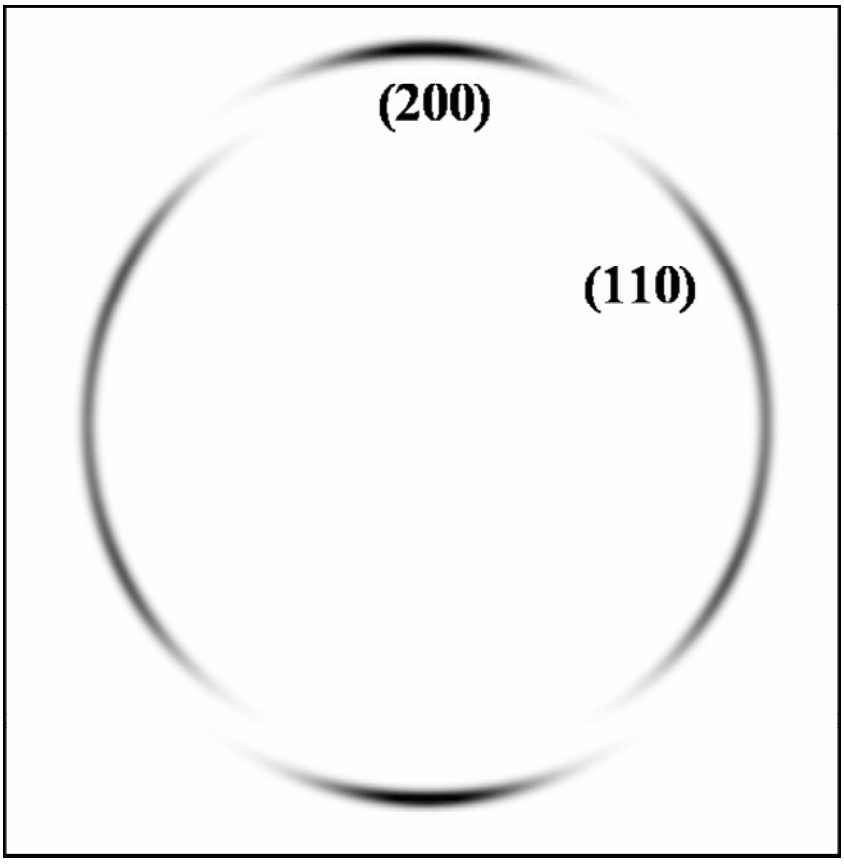

Figure 4.10

Chapter 5. Flow-Induced Crystallization Precursor Structure in High Molecular Weight Isotactic Polypropylene (HMW-iPP)/Low Molecular Weight Linear Low Density Polyethylene (LMW-LLDPE) Binary Blend Melts

5.1 Introduction

The molecular mechanism, responsible for the flow-induced crystallization behavior, has been linked to the concept of coil-stretch transition for polymer chains, which was first proposed by de Gennes decades ago, based on the chain dynamics in dilute polymer solutions.[1] For flow-induced crystallization in concentrated or entangled polymer melts, Keller also adopted the concept, whereby he proposed the 'two-fold criticality' of the coil–stretch transition.[2] That is, for a monodisperse polymer, there exists a critical strain rate ($\dot{\varepsilon}_c$) and, for a given strain rate, there exists a critical orientation molecular weight (M_c). The former indicates that, in a monodisperse polymer solution or melt, the polymer chains can be stretched out only when the strain rate level is higher than $\dot{\varepsilon}_c$, whereas, the latter means that, in a polydispersed solution or melt at a fixed strain rate, only chains longer than M_c will be stretched out while the rest of shorter chains remains in random-coiled state without experiencing the transition. In the latter case, the increase in strain rate increases the amount of chains that becomes extended by decreasing M_c in the molecular weight distribution. Based on the above findings, it has been hypothesized that the final morphology of oriented polymers, i.e., fibers and blown films, is a direct consequence of the initial state of crystallization induced by flow, where the high molecular weight tail in the molecular weight distribution plays a much more important role than the rest of shorter chains. For example, the shish-kebab structure

consisting of an extended-chain crystal (shish) and folded-chain lamella (kebabs) is thought to be the direct indication of the coil-stretch transition of polymer chains in which, while the stretched chains (higher molecular weight species) forms shish, the coiled chains (lower molecular weight species) crystallize into kebabs.

Recent simulation study has shown that even monodisperse polymer can exhibit two stable populations of stretched and coiled states at a given strain rate depending on the local concentration fluctuation in polymer solution.[3] The stretched chains finally transformed into shish, while the coiled chains could form kebabs (folded-chain lamellae) by means of adsorption process. Also, changing strain rate altered the two populations significantly and thus affecting the initial stages of flow-induced crystallization. Also, the coil-stretch transition at the whole chain length level in entangled polymer melt is still controversial. This is because it is very unlikely that long and entangled chain fully disentangles itself and undergoes the coil-stretch transition under typical experimental conditions, as in our recent *rheo*-X-ray studies.[4-7] In the studies, it was argued that the deformation of highly entangled species (entanglement network) in the melt directly results in generations of both stretched and coiled chain segments between entanglement points, where the stretched chain segments formed shish (i.e., extended-chain crystal or oriented mesomorphic structure) by accompanying folded-chain crystallization forming kebabs.

Hashimoto et al. have shown the existence of flow-induced concentration fluctuation (liquid-liquid phase separation) prior to the flow-induced crystallization in concentrated polyethylene/paraffin wax solution.[8] In their studies, they argued that the initial flow-induced crystallization might be driven by flow-induced phase separation. Olmsted *et. al*., have shown that the possibility of interplay between strain and nematic-

like short-range orientational interaction of stretched chain segments can induce the anisotropic spinodal decomposition in bidiperse polymer blend of which molecular weights are well-separated.[9] In this study, the miscibility between the two species was frustrated upon applying flow, since the two species with well-separated relaxation times responds fairly differently to an external flow field. De Gennes et al. argued that even molten polymer can exhibit spinodal decomposition if temporary chain orientation is given by rapid stretching.[10] Also, Olmsted et al. suggested that the interplay between extended-chin conformation and packing induces liquid-liquid bimodal phase and applied shear enhance the kinetic role of the bimodal phase.[11] Even though the explanations are slightly different one to another, they seem to agree that there exists a preexisting state induced by the coupling between applied flow and interaction between stretched chain segments (flow-induced phase separation). It can be thought that such coupling may form the basis of oriented superstructure. However, it is conceived that if such process (bimodal or spinodal process) alone can explain the 'thermodynamic' initial crystallization precursor structure ('stable' critical nucleus) formation.

A great deal of studies has been performed to clarify the molecular basis for the flow-induced crystallization in polymer solutions or polymer melts for last several decades. However, more insight into the exact molecular mechanism in forming the initial crystallization precursor structure in the presence of flow, prior to the full scale crystallization mechanism is still an important subject to be elucidated.

In semicrystalline polymer blend system, the level of molecular mixing plays a major role in the structure development of final products. Thus, the phase behavior of semicrystalline polymer blend system has long been an important subject during past several decades. In iPP/PE binary blends, it is known that iPP is immiscible with

polyethylene.[12-14] However, some group has recently reported that iPP can be miscible with PE within limited temperature window and composition.[15-19] Indeed, based on the Flory-Huggins theory,[20] the iPP/LLDPE blend system should follow an upper-critical solution temperature (UCST) behavior.

In chapter 5, we have designed a unique polymer blend system containing higher molecular weight isotactic polypropylene (HMW-iPP) and lower molecular weight linear low-density polyethylene (LMW-LLDPE). Two experimental temperatures (130 ^{o}C and 140 ^{o}C) above cloud points were chosen by assuming UCST behavior; the temperatures were sufficiently low to enable the crystallization of iPP (can be viewed as the solute) in the presence of flow but high enough to prevent the crystallization of LLDPE (can be viewed as the solvent). The flow-induced crystallization behavior of HMW-iPP in this blend system was investigated by synchrotron *rheo*-WAXD (wide-angle X-ray diffraction) and *rheo*-SAXS (small-angle X-ray scattering) techniques. Specifically, by varying the composition of the blends, the effect of concentration (directly related to the density of chain entanglement) in the early stages of flow-induced crystallization was explored.

5.2 Experimental

5.2.1 Materials and sample preparation

A high molecular weight iPP, HMW-iPP; M_w= 580,000 g/mol, polydispersity = 3.5 and low molecular weight LLDPE, LMW-LLDPE; M_w = 50,000 g/mol, polydispersity = 2.3 were chosen to prepare polymer blends for this study. Polymer blends, containing 3,

6 and 9 wt% of iPP in LLDPE matrices, were prepared by solution blending procedure to ensure the blending of the two different species at the molecular level. First, iPP and LLDPE were dissolved in Xylene at 140 °C under continuous stirring until a transparent homogeneous solution was formed. Then the solution was poured into chilled methanol of which volume was 5 times higher than the solution volume under vigorous stirring to precipitate the polymer mixture. The polymer blend slurry was then filtered from a xylene and methanol mixture and vacuum dried at 80 ^{o}C for 24 hours. In order to investigate the formation of flow-induced crystallization precursor scaffold in HMW-iPP/LMW-LLDPE blend melts in view of concentration-dependent entanglement between HMW-iPP, the overlap concentration of HMW-iPP was calculated based on the equation, $c^* = 3M_w \Big/ 4\pi\left[\left\langle R_g^2\right\rangle^{1/2}\right]^3 N_a$, where, $\left\langle R_g^2\right\rangle^{1/2}$ being the root-mean-square radius of gyration and N_a being the Avogadro's number.[21-23] The estimated overlap concentration was, $c^* \cong$ 1 wt%. Thus, the respective concentrations of iPP in these blends, 3, 6 and 9 wt%, were higher than the calculated overlap concentration.

5.2.2 Instrumentation

A Linkam CSS-450 optical shear stage, modified for *in-situ. rheo*-X-ray studies was used to apply controlled shear conditions to the polymer blend melts. The details of this modified shear apparatus have been described elsewhere.[24] Polymer films with about 0.5 mm thickness were prepared by compression molding at 210 ^{o}C. Samples in the form of a ring (inner diameter = 10 mm, outer diameter = 20 mm) were cut from the melt pressed films for *rheo*-X-ray measurements. The sample was placed in the gap between

two X-ray windows (i.e., a diamond window and a Kapton window) and completely enclosed in the measuring cell. The chosen shear rate and shear duration time were shear rate, $\dot{\gamma} = 110\, s^{-1}$, shear duration, $t_s = 5\, s$, respectively. Thus, the applied strain, $\varepsilon = \dot{\gamma} \cdot t_s$, constantly imposed to samples was 550. *In-situ rheo*-2D WAXD and -SAXS measurements were carried out at the X27C beamline in the National Synchrotron Light Source (NSLS), Brookhaven National Laboratory (BNL). The wavelength of the synchrotron radiation was 1.366 Å. 2D *Rheo*-WAXD and -SAXS patterns were collected by using MAR CCD X-ray detector (MAR-USA), which had a resolution of 1024×1024 pixels (pixel size = 158.44 μm). For SAXS measurements, the sample-to-detector distance was 1765 mm and the scattering angle was calibrated by using silver behenate (AgBe); for WAXD measurements, the sample-to-detector distance was 111.5 mm and the diffraction angle was calibrated by using aluminum oxide (Al_2O_3). All X-ray images (SAXS and WAXD) were corrected for background scattering including air scattering, sample absorption and synchrotron X-ray beam fluctuations. Also, to obtain cloud points of each blend, the Linkam CSS-450 optical shear stage with original design was used to perform laser transmission measurement under quiescent condition. The wavelength of He-Ne laser was 632.8nm and the transmitted laser was counted by using pindiode. Also, to investigate the crystallization behavior during cooling, DSC measurements were performed by using Perkin-Elmer DSC 7 instrument. The cooling rate was -1K/min. All the DSC runs were carried out under nitrogen gas flow to minimize the sample degradation. An indium standard was used to calibrate the temperature.

5.2.3 Experimental Procedure

In order to ensure that the polymer melts were free of any memory effects associated with the prior thermal and orientation history, all polymer samples were subjected to heating to 210 ^{o}C which is substantially higher than the theoretical equilibrium melting temperature of polyethylene and polypropylene and held for 10 min. The melts were then cooled down to the chosen crystallization temperature of 130 and 140 ^{o}C at the rate of -30 K/min. When the temperature was reached the chosen crystallization temperatures, SAXS and WAXD images were begun to collect in real time. All the data acquisition time was 15 s and the data storage time was 5 s for each SAXS and WAXD patterns. In DSC and cloud point measurements, the blends were initially heated up to 210 ^{o}C and maintained for 10 min to erase all thermal and orientation history. Then the temperature was slowly decreased to ambient temperature at a rate of -1 K/min.

5.3 Results and discussions

5.3.1 DSC and cloud point measurement (Laser transmission)

Prior to the investigation of the flow-induced crystallization behavior in HMW-iPP/LMW-LLDPE blends with synchrotron X-rays, the measurements of DSC and classical light transmission using He-Ne laser were carried out to determine the crystallization temperature and the cloud point at quiescent state. Figure 5.1 shows DSC cooling thermograms, showing the crystallization exotherms, for 3/97, 6/94 and 9/91 HMW-iPP/LMW-LLDPE blends. Thermograms of pure samples, i.e., HMW-iPP and LMW-LLDPE, were also added in Figure 5.1. It is shown that these blends only exhibit

single narrow exotherm with peak temperature (T_c) around 105 ± 0.3 ^oC, consistently with the T_c of LMW-LLDPE. It is also seen that no clear sign of HMW-iPP crystallization at around 115 ^oC is appeared in the thermograms of the blends. We note that, upon heating, the heating thermograms of the blends clearly exhibited small but discrete melting endotherms of HMW-iPP at around 165 ^oC. This implied that the HMW-iPP in the blends obviously crystallized during cooling and they melt away under heat energy. Thus, it can be thought that the observed single exothermic peak of the blends is associated with the crystallizations of both HMW-iPP and LLDPE. That is, the crystallization temperature of HMW-iPP in the blends was decreased significantly due to the presence of LMW-LLDPE while its exotherm overlapped with that of LMW-LLDPE and/or the crystallization exotherm of HMW-iPP was very broad thus it was not seen in the DSC thermograms. Indeed, the crystallization temperature depression is general phenomenon in the crystallization of miscible binary polymer blend.[25,26] In PP/PE blend, it has recently been reported that the crystallization of PP in PE matrix was strongly governed by the concentration of PE if the fraction of PP is lower than 20 wt %, where the crystallization rate of PP decreased significantly with the increase of PE concentration.[18] It was argued that the decreased crystallization rate of PP in PE matrix was due to the decreased nucleation density and the diffusion problem to crystal growth fronts. Also, Similar behavior has been reported by Bassett et al.[19] In the report, when the blending composition of PP was higher than 20 wt %, the blends clearly showed two discrete crystallization exotherms at around 89~93 ^oC (PE) and 110 ^oC (PP). As the blending composition of PP was decreased less than 20 wt % (e.g., 10 and 15 wt %) a new exothermic peak at around 81~83 ^oC was observed while PE peak maintained the same. The new peak was assigned as the crystallization of PP in which the crystallization

of PP was decreased significantly due to PE. In both reports, the decreased crystallization temperature of PP was responsible for the good miscibility in a molecular level.

The cloud points (T_{Cloud}) of the blends and pure samples obtained from the laser transmission measurement were depicted in Figure 5.2. Also, DSC crystallization temperatures taken at the peak maximum (T_c), and at the on-set (T_{oc}) point were also added in Figure 5.2 for comparison purpose. In Figure 5.2, the cloud points of pure LMW-LLDPE and HMW-iPP which are somewhat higher than the T_{oc} are obviously related to the initial stages of crystallization at the quiescent condition. However, the cloud point of the binary blends that were shown to increase with the iPP fraction while exhibiting totally different change with T_{oc} can be thought to represent the common UCST phase behavior (Liquid-Liquid phase separation) of PP/PE blends.

Based on the results of DSC and cloud point measurements, we have selected two experimental temperatures (i.e., 130 and 140 ^{o}C) for the study of flow-induced crystallization of HMW-iPP in LMW-LLDPE matrix. In the experimental time frame at the temperatures, all blends appeared to remain in an effectively dispersed state, since any presence of scatter or crystal was detected by SAXS and WAXD measurements. If the chosen temperatures were lower than the phase separation temperatures, we speculate that the phase separation time was significantly longer than the experimental time frame (45 min).

5.3.2 Rheo-WAXD results

Figures 5.3(a), 5.3(b) and 5.3(c) show selected 2D *rheo*-WAXD patterns of the binary blends collected at 130 ^{o}C after shear (shear rate, $\dot{\gamma}$=110 s^{-1}, shear duration time,

t_s=5s), respectively. We note that, under quiescent condition at 130 and 140 ^oC which was higher than cloud points of each blend, no crystalline structure or scatter formation was detected by both WAXD and SAXS. In Figure 5.3 (a), it is seen that the 3/97 blend did not exhibit any sign of crystallization, indicating the presence of a molten amorphous state. The patterns of the 6/94 and 9/91 blends in Figures 5.3(b) and 5.3(c), however, clearly showed distinct crystalline diffractions induced by shear. It was found that the observed crystalline reflections could be indexed from the α-crystal form of iPP, which confirmed that LLDPE merely acted as amorphous polymeric matrix and this will be discussed later in Figures 5.5 (a)-5.5(c). Since no crystallization was observed by SAXS and WAXD in any blend under the quiescent state at 130 ^oC, the observed crystalline reflections in the 6/94 and 9/91 blends were mainly due to the application of shear. Even though the preferred crystal orientation was not clearly discerned in the 2D WAXD patterns, this does not mean that the initial nucleation process was completely random. Rather, we hypothesize that at the very initial stage of flow-induced crystallization, a scaffold of oriented HMW-iPP nuclei was formed. The concentration of these nuclei might be low because the viscosity of the LMW-LLDPE matrix was low, which also reduced the relaxation spectrum of the HMW-iPP component. Consequently, most of the segments in HMW-iPP chains were in the random coiled state, resulting in the growth of unoriented lamellae.

The initial formation of iPP crystallization precursor structure may take place in the following manner (Figure 5.4). Immediately after the cessation of shear, all stretched chain segments begin to relax based on their characteristic relaxation time (τ) that is scaled with the molecular weight (M_w), $\tau \propto M_w^{3.4}$. Clearly, the only species that can retain some molecular orientation is the HMW-iPP chains, which is in the entangled state. The

entanglement density in HMW-iPP chains is a function of its concentration. At higher HMW-iPP concentrations, the entanglement density is higher, leading to a higher concentration of the stretched chain segments but at a lower degree of chain stretching. This may lead to the folded-chain crystallization of α-form iPP crystals (point-like nuclei) or the formation of short mesomorphic fibrils (thread-like nuclei) of which size is comparable to the stable critical nuclei size, r^*. This can initiate the kebab growth of adjacent chain segments in the coiled state. In contrast, at lower HMW-iPP concentrations, the entanglement density is lower, leading to a lower concentration of the stretched chain segments but at a higher degree of chain stretching. This will not lead to the production of an effective nuclei network, which may explain the absence of flow-induced crystallization in the 3/97 blend.

At the elevated crystallization temperature, 140 ^{o}C, under the same shear condition, 6/94 and 9/91 blends also presented promoted crystallization by shear similarly to the crystallization at 130 ^{o}C, while exhibiting weaker crystalline reflection rings. 3/97 blend again showed amorphous halo at the temperature.

In order to probe the crystalline structure evolution in more detail, the 2D *rheo*-WAXD patterns of 6/94 and 9/91 blends obtained at 130 and 140 ^{o}C were integrated and curve-fitted to index the crystalline peaks and to obtain crystallinity. The curve-fitting was carried out by using Voight functions. The integrated WAXD profiles of 6/94 and 9/91 blends obtained at 130 ^{o}C were depicted in Figures 5.5(a) and 5.5(b), respectively. Also, a curve-fitted profile was exemplified in Figure 5.5(c) along with indexed crystalline peaks. In Figures 5.5(a)-5.5(c), it is noted that the sheared 6/94 and 9/91 blend melts exhibit the typical crystalline reflection patterns of α-crystal form of iPP without LLDPE contribution.

Figure 5.6(a) and 5.6(b) present crystallinity changes of 6/94 and 9/91 blend obtained from the 2D *rheo*-WAXD patterns measured at 130 and 140 ^{o}C, respectively. 3/97 blend was remained in molten state at both temperature. It is shown that crystallization rate as well as crystallinity increases with HMW-iPP concentration. It is also seen that the crystallization rate and crystallinity increases as quench depth (ΔT) increases. In crystallization of polymer solution under shear, the concentration of polymer is rate-determining in both nucleation and growth processes because the flow-induced nucleation is strongly governed by the relaxation time of polymer chain where the relaxation time of polymer chain is dominated by the concentration of polymer. Especially, when the concentration of polymer chain (c) becomes higher than the overlap concentration (c^*), $c \geq c^*$, the relaxation time of polymer chain begins to increase greatly as they effectively start to overlap, interpenetrate and become entangled. As a result, as the concentration of polymer chains increases, the system becomes more sensitive in forming initial crystallization precursor structure while enhancing the rate and the density of initial crystallization precursor structure which will finally lead to the increased kebab (folded-chain lamella) growth rate.

On the other hand, in Figures 5.6(a) and 5.6(b), the crystallinity and the crystallization rate which were appeared to be lower at the elevated temperature in both blends can be explained by the view of initial crystallization precursor structure formation as follows. Even though the entanglement density of HMW-iPP in LMW-LLDPE matrix remains the same, the relaxation time of stretched chains becomes shorter with the increase of crystallization temperature due to the increased chain dynamics, whereas, the critical size of stable crystal nuclei becomes larger. Thus, they lead to the decrease the concentration of initial crystallization precursor structure which finally

results in decreased nucleation rate and growth rate. Once the process of initial crystallization precursor structure (nucleation) is finished, the growth rate and the total crystallinity of kebab become dominated by the concentration of crystallizable HMW-iPP.

Even though the *rheo*-WAXD patterns did not exhibit clearly oriented diffraction feature, *rheo*-SAXS patterns obtained at the same conditions confirmed that the observed crystalline reflections were mainly due to the formation of flow-induced crystallization precursor scaffold.

5.3.3 Rheo-SAXS results

Selected 2D *rheo*-SAXS patterns of each blends collected at 130 ^{o}C are shown in Figures 5.7(a)-5.7(c). In Figure 5.7(a), it is seen that 2D *rheo*-SAXS pattern of 3/97 blend exhibits only a molten state even after shear, consistent with the *rheo*-WAXD result. However, the patterns of 6/94 and 9/91 blend in Figures 5.7(b) and 5.7(c) clearly show the formation of oriented kebab (lamella) and their scattered intensities were intensified with time. It is clearly evidenced that the HMW-iPP formed initial crystallization precursor structure by the application of flow and they finally induced oriented kebab evolution. Also, at this crystallization stage, the kebab long period (L_P) of 6/94 and 9/91 blend were remained constant, $L_p \approx 24$ nm, (Figure 5.8). This implied that the concentrations of initial crystallization precursor structure in both blend melts were dilute enough not to allow inter-kebab impingement and the kebab nucleation is instantaneous (athermal nucleation).

In order to compare the orientation distribution of kebabs between the 6/94 and 9/91 blends, the azimuthal intensity distributions at the first-order peak position, s ≈

0.041 nm^{-1}, were obtained from the 2D *rheo*-SAXS patterns collected at t=1810 s. This result is depicted in Figure 5.9. It is seen that the lamella orientation in the 9/91 blend is greater than that of the 6/94 blend, which is consistent with our above argument, i.e., at higher HMW-iPP concentrations, the entanglement density is higher, leading to a higher concentration of the stretched chain segments and thus more stable and oriented nucleation network.

In addition to the chain entanglement argument, the role of HMW-iPP concentration in forming initial crystallization precursor structure can also be explained. based on Keller's concept of critical orientation molecular weight, M_c.[2] That is, in a polydispersed polymer melt, at a fixed strain rate, only chains longer than M_c can remain in the stretched state, while the rest of chains will relax back to the random-coiled state. The increase in strain rate does not affect the degree of chain extension but increases the amount of chains that can remain stretched by decreasing the value of M_c in the molecular weight distribution.

It appears that the value of M_c is also concentration-dependent since the entanglement density and thus the relaxation time spectrum is governed by the concentration, especially when the concentration of polymer chain (c) is larger than the overlap concentration (c^*), $c \geq c^*$. Thus, under *given* shear conditions, the increase in concentration may decreases the critical orientation molecular weight. This is because the resulting relaxation time distribution becomes broader while shifting the distribution toward the longer relaxation time region.

5.4 Conclusion

The formation of the initial crystallization precursor structure in HMW-iPP/LMW-LLDPE blends induced by flow was investigated by using synchrotron *rheo*-WAXD and -SAXS techniques. As the shear was applied at a sufficiently high temperature above cloud point, only the HMW-iPP chains could form the shish-kebab structure in 6/94 and 9/91 blends while LMW-LLDPE merely acts as an amorphous matrix. The results clearly showed that the formation of flow-induced crystallization precursor structure is strongly governed by the concentration of HMW-iPP in the blends. When the HMW-iPP concentration was low, no flow-induced crystallization was observed. As the concentration of HMW-iPP increased above 3wt %, flow-induced nucleation, kebab (folded-chain lamella) growth rate, crystal orientation and crystallinity were all greatly enhanced.

5.5 References

1. de Gennes, P. G. *J. Chem. Phys.* **1974**, 60, 5030.
2. Keller, A., Kolnaar, J.W.H. *Prog. Colloid Polym. Sci*. **1993**, 92, 81.
3. Dukovski, I., Muthukumar, M. *J. Chem. Phys*. **2003**, 118, 6648.
4. Zuo, F., Keum, J. K., Yang, L., Somani, R. H., Hsiao, B. S. *Macromolecules*, **2006**, 39, 2209.
5. Somani, R. H., Yang, L., Hsiao, B. S., Sun, T., Pogodina, N. V., Lustiger, A., *Macromolecules*, **2005**, 38, 1244.
6. Somani, R. H., Yang, L., Zhu, L., Hsiao, B. S., *Polymer*, **2005**, 46, 8587.
7. Somani, R. H., Yang, L., Hsiao, B. S. *Polymer*, **2006**, 47, 5657.
8. Murase, H., Kume, T., Hashimoto, T., Ohta, Y. *Macromolecules ,***2005**, 38, 8719.
9. Olmsted, P. D., Milner, S. T. *Macromolecules,* **1994**, 27, 6648.

10. Brochard-Wyart, F.;de Gennes, P. G. *C. R. Acad. Sci. Paris* 306 (II) **1988**, 699.

11. Olmsted, P. D., Poon, W. C. K.; McLeish, T. C. B., Terril, N. J., Ryan. A. J. *Phys. Rev. Lett.,* **1998**, 81, 373.

12. Sano, H., Yiu, H., Li, H., Inoue, T. *Polymer* **1998**, 39, 5265

13. Rajasekaran, J. J., Curro, J. G., Honeycutt, J. D. *Macromolecule*s **1995**, 28, 6843

14. Teh, J. W. *J. Appl. Polym. Sci.* **1983**, 28, 605.

15. Lo, C. -T., Seifert, S., Thiyagarajan, P., Narasimhan, B. *Macromol. Rapid Comm.* **200 5**, 26, 533.

16. Lo, C. -T., Seifert, S., Thiyagarajan, P., Narasimhan, B. *Polymer* **2004**, 45, 3671

17. Li, J., Shanks, R. A., Long, Y. *Polymer* **2001**, 42, 1941

18. Li, J., Shanks R. A., Olley, R. H., Greenway, G. R. *Polymer* **2001**, 42. 7685.

19. Dong, L, Olley, R. H., Bassett, D. C. *J. Mater. Sci.* **1998**, 33, 4043.

20. Flory, P. J. Principles of Polymer Chemistry, **1953**, Cornell University Press, Ithaca.

21. de Gennes, P. G. *Scaling Concepts in Polymer Physics*; Cornell University Press: Ithaca, NY, **1979**.

22. Seki, M.; Thurman, D. W.; Oberhauser, J. P.; Kornfield, J. A. M*acromolecules*, **2002**, 35, 2583.

23. Yang, L; Somani, R. H.; Sics, I.; Hsiao, B. S.; Kolb, R.; Fruitwala, H.; Ong, C. M*acromolecules*, **2004**, 37, 4845.

24. Somani, R. H., Hsiao, B. S., Nogales, A., Srinivas, S., Tsou, A. H., Sics, I., Balta Calleja, F. J., Ezquerra, T. A. *Macromolecules*, **2000**, 33, 9385.

25. Hoffman, J. D., Davis, G. T., Lauritzen, J. I. *Treatise on Solid State Chemistry*. Hannay NB (Ed), Plenum Press, New cork, Vol 3, Chap 7. **1976**.

26. Hu, S. R. Kyu, T. Stein, R. S. *Polym. Sci. Part B. Polym. Phys*. Ed. **1987**, 25. 71.

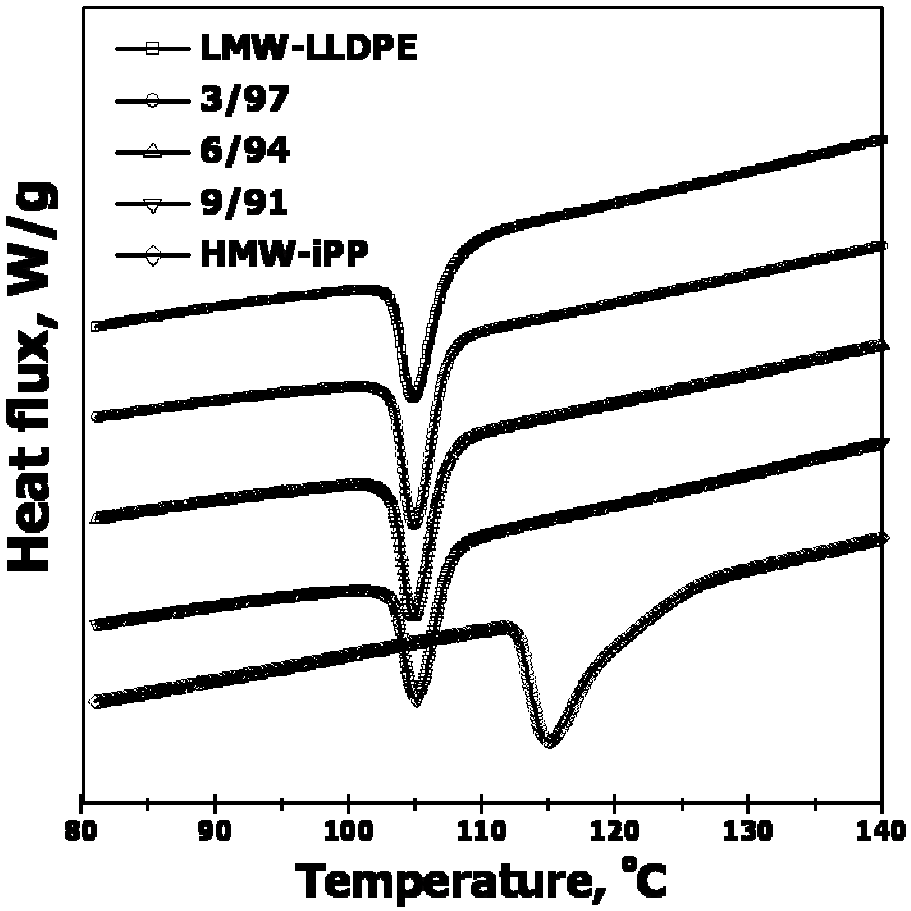
LMW-LLDPE
3/97
6/94
9/91
HMW-iPP
Heat flux, W/g
80
90
100
110
120
130
140
Temperature, °C

Figure 5.1

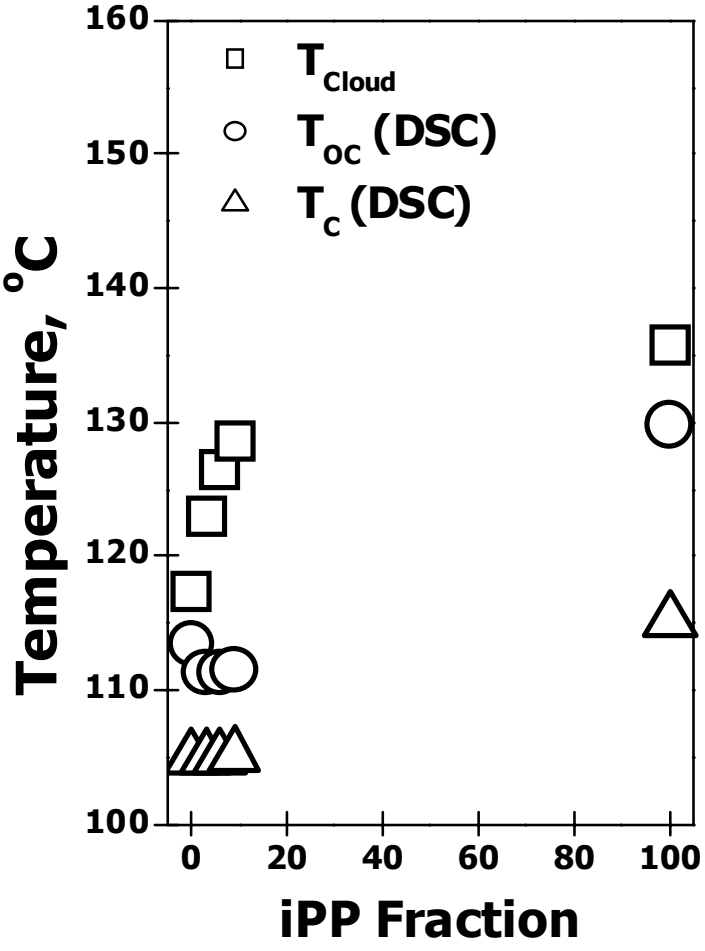
160
150
140
130
120
110
100
0
20
40
60
80
100
Temperature, °C
iPP Fraction
T Cloud
T OC (DSC)
T C (DSC)

Figure 5.2

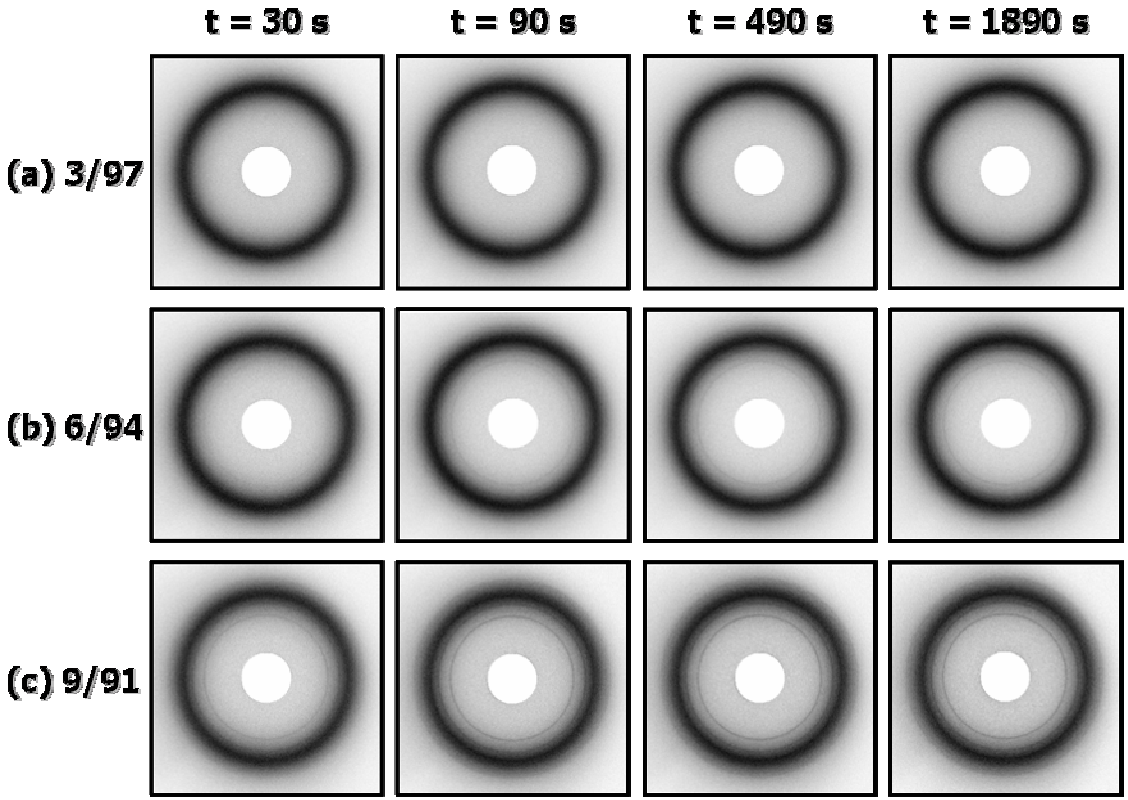

Figure 5.3(a), 5.3(b) and 5.3(c)

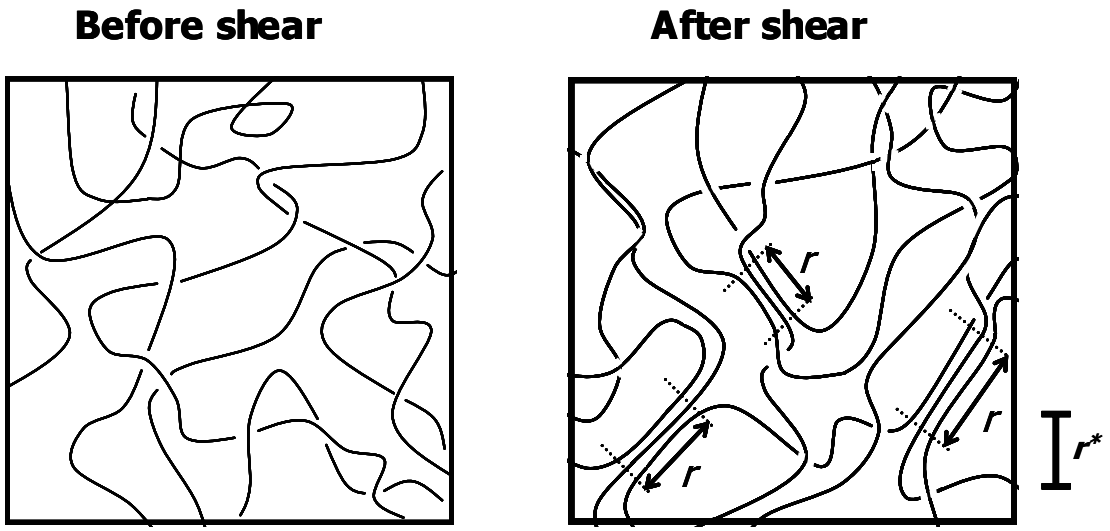

Figure 5.4

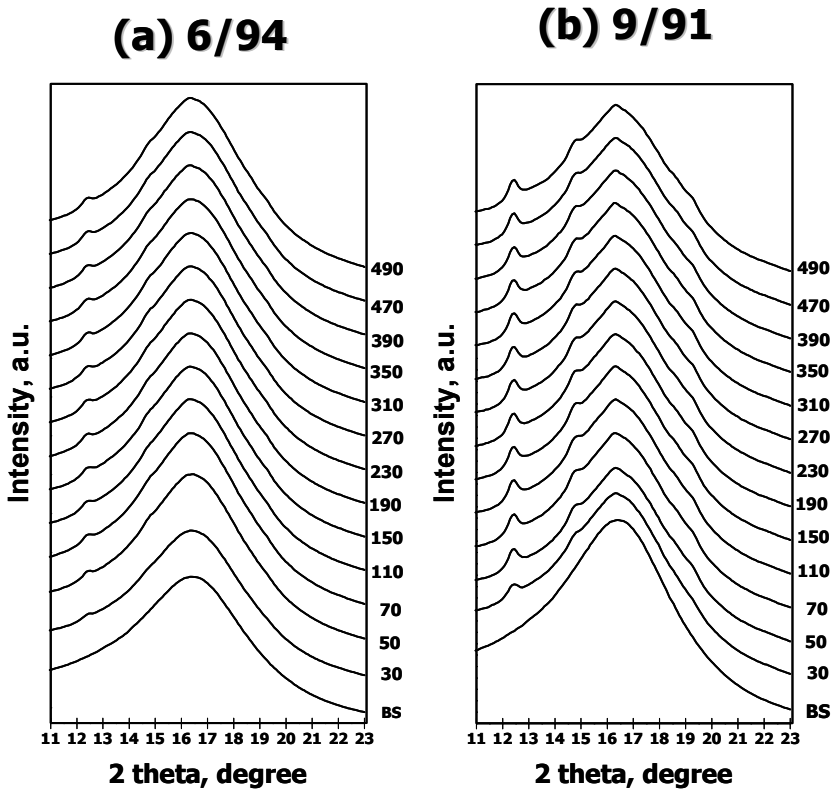

Figure 5.5(a) and 5.5(b)

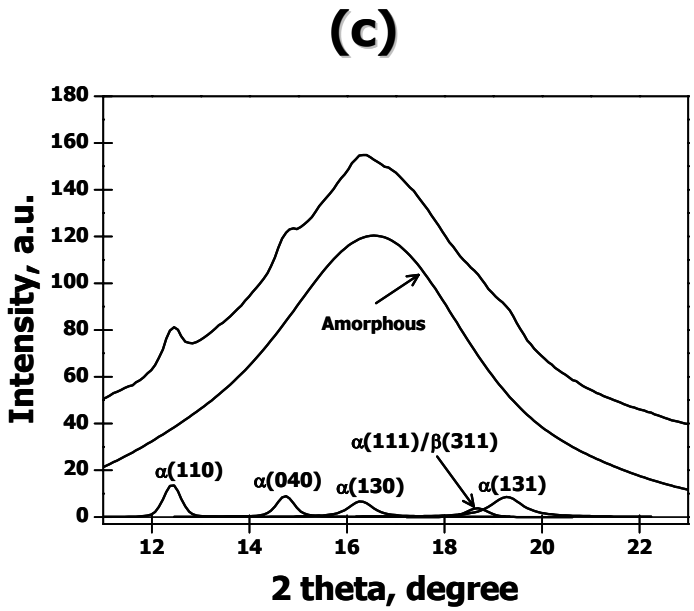
(c)
Intensity, a.u.
2 theta, degree
Amorphous
α(110)
α(040)
α(130)
α(111)/β(311)
α(131)
0
20
40
60
80
100
120
140
160
180
12
14
16
18
20
22

Figure 5.5(c)

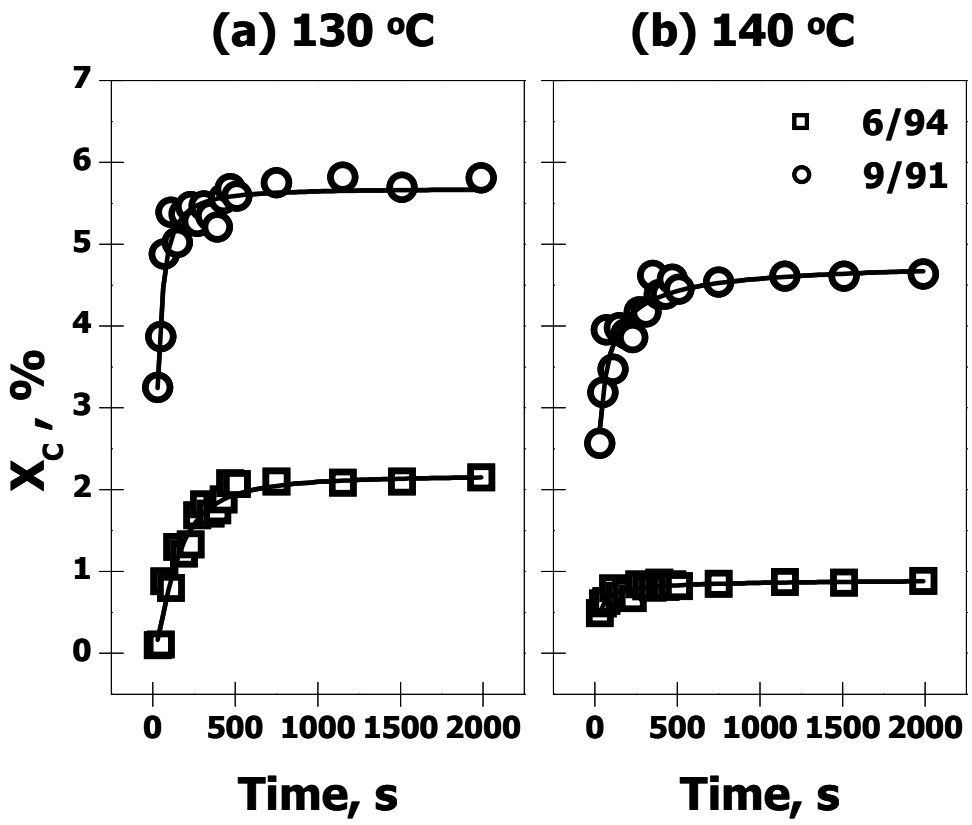

Figure 5.6(a) and 5.6(b)

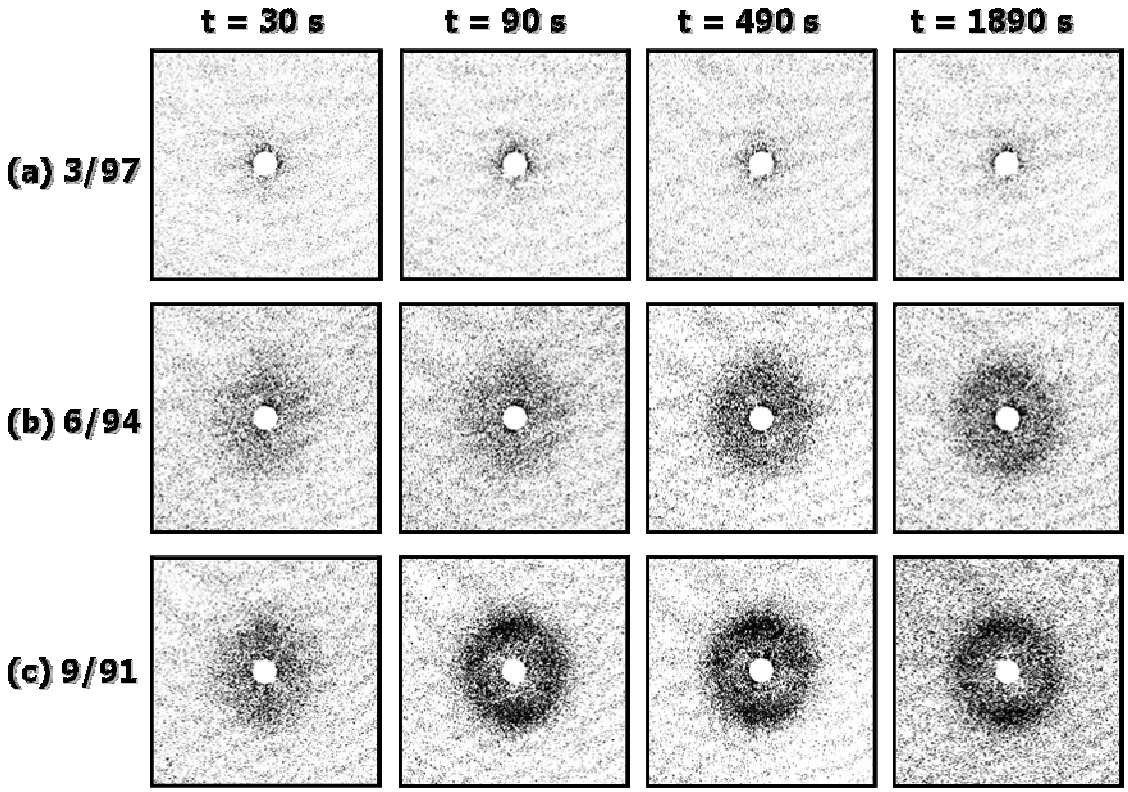

Figure 5.7(a), 5.7(b) and 5.7(c)

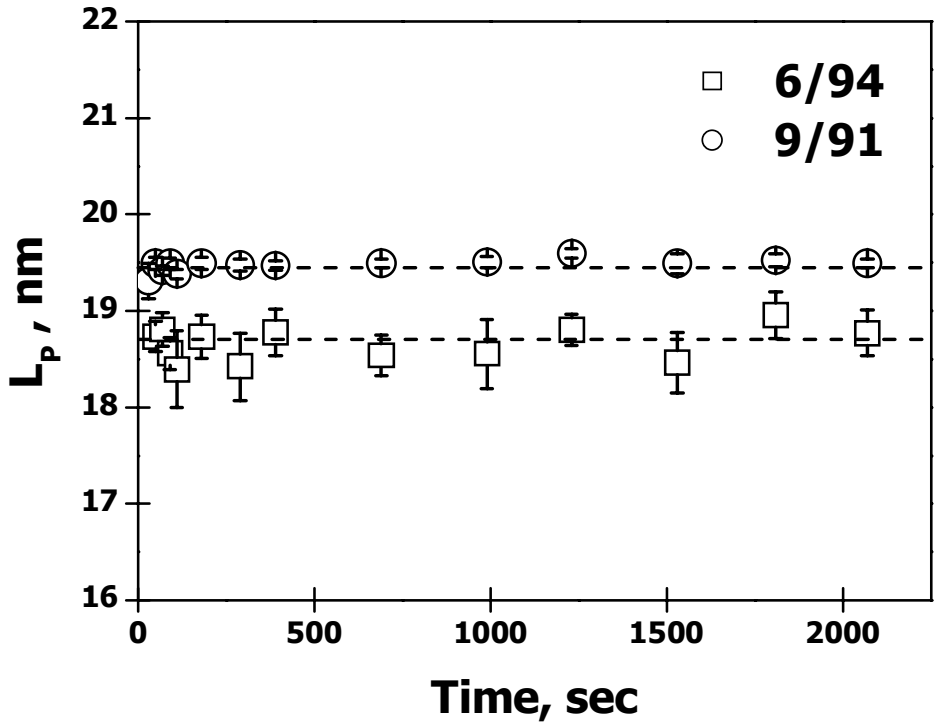

Figure 5.8

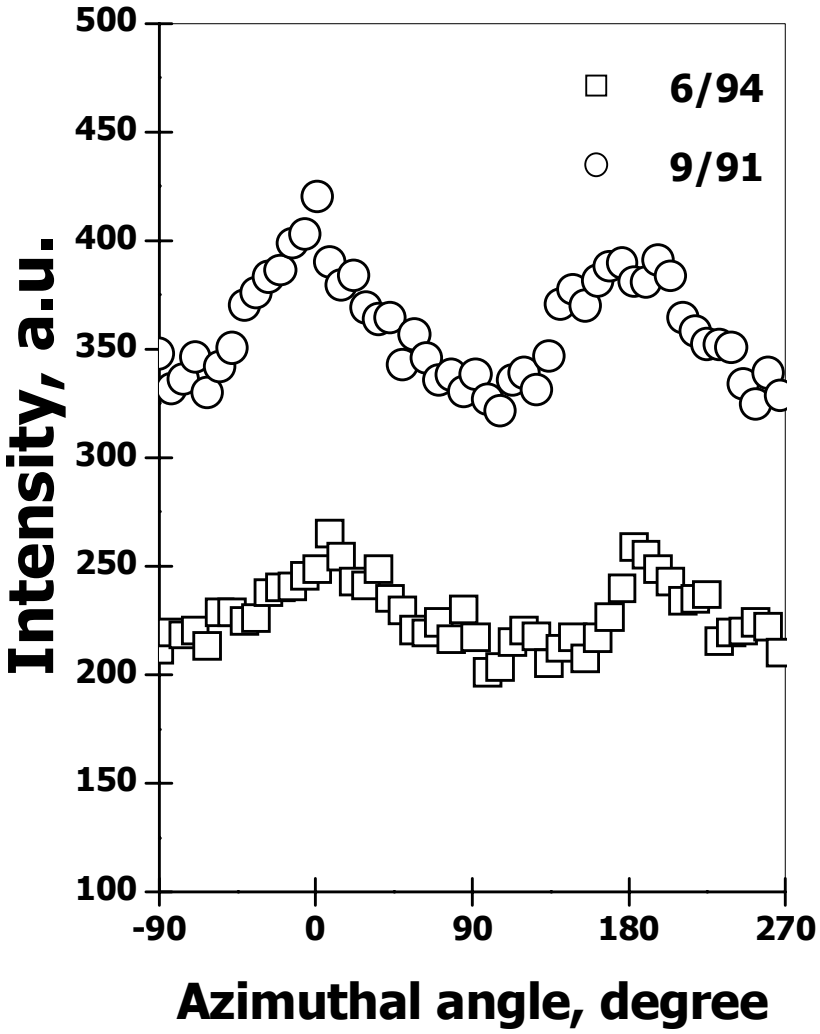
500
450
400
350
300
250
200
150
100
-90
0
90
180
270
6/94
9/91
Intensity, a.u.
Azimuthal angle, degree

Figure 5.9

Concluding Remarks

By using *in-situ rheo*-SAXS and -WAXD techniques, the nature of flow-induced crystallization precursor structure, i.e. shish-kebab entities, formed in deformed polyolefin melts was probed. The study was performed under two different conditions to elucidate the role of high molecular weight chain as well as the effects of strain rate and strain in the formation of flow-induced crystallization precursor structure. The results showed that the formation of flow-induced crystallization precursor structure is greatly enhanced by a small amount of high molecular weight chains above the overlap concentration. This implies that high molecular weight chains play an essential role in forming flow-induced crystallization precursor structure, where the deformation of the entanglement network of high molecular weight chains would produce a stable oriented network consisting of stretched and coiled segments between entanglement points. Also, it was demonstrated that the flow-induced crystallization precursor structure formation is strongly the function of the applied strain as well as the strain rate. As strain and rate are increased, the formation of flow-induced crystallization precursor structure is significantly facilitated. Most of all, a critical strain, ε_c exists in the formation of flow-induced crystallization precursor structure, even when the applied strain rate, $\dot{\varepsilon}$ is higher than the critical strain rate, $\dot{\varepsilon}_c$. Around ε_c, a sharp transition from amorphous to crystalline state was observed, verifying that the shish precursor structure is formed first and it subsequently induces the growth of folded-chain lamellae, i.e. kebabs.

Also, flow-induced shish-kebab structure was subject to heating under planar constraint to investigate the thermal stability. The results indicated that the stability of kebab is dictated by the thermodynamics of coiled chains. In contrast, the stability of

shish was dictated mainly by the dynamics of stretched entanglement network under the planar constrained conditions. Since the relaxation time of the stretched entanglement network is directly the function of the fraction of added high molecular weight chains, adding more high molecular weight chain leads to the formation of thermally more stable shish with slower chain dynamics and thus higher melting point.